

Novel Techniques for Optical Performance Monitoring in Optical Systems

KU, Yuen Ching

A Thesis Submitted in Partial Fulfillment
of the Requirements for the Degree of
Doctor of Philosophy

in

Information Engineering

©The Chinese University of Hong Kong
August 2007

The Chinese University of Hong Kong holds the copyrights of this thesis. Any person(s) intending to use a part or whole of the materials in the thesis in a proposed publication must seek copyright release from the Dean of the Graduate School.

UMI Number: 3302447

INFORMATION TO USERS

The quality of this reproduction is dependent upon the quality of the copy submitted. Broken or indistinct print, colored or poor quality illustrations and photographs, print bleed-through, substandard margins, and improper alignment can adversely affect reproduction.

In the unlikely event that the author did not send a complete manuscript and there are missing pages, these will be noted. Also, if unauthorized copyright material had to be removed, a note will indicate the deletion.

UMI[®]

UMI Microform 3302447

Copyright 2008 by ProQuest LLC.

All rights reserved. This microform edition is protected against unauthorized copying under Title 17, United States Code.

ProQuest LLC
789 E. Eisenhower Parkway
PO Box 1346
Ann Arbor, MI 48106-1346

Acknowledgement

First and foremost, I would like to express my deepest gratitude to my thesis supervisor, Prof. Calvin Chun-Kit Chan, for his continuous guidance and support in my research and studies. Thanks for his valuable advice, fruitful discussion and enormous help throughout my postgraduate studies. His working attitude and scholarship has always been inspirational to me.

I would also like to express my appreciation to Prof. Lian-Kuan Chen. He has in-depth knowledge and a strong sense of direction. Discussions with him have always inspired many research ideas. I would also like to thank Prof. Chinlon Lin, Prof. Frank Tong and Prof. K.W. Cheung for their continuous support and advice.

It is my pleasure to have chance to work with many talented fellow postgraduate students in Lightwave Communications Laboratory in the Department of Information Engineering. Thanks must go to past and present lab members including Dr. Li Huo, Mr. Jian Zhao, Mr. Ning Deng, Mr. Jordan Tse, Mr. Qiguang Zhao, Mr. Zhenchang Xie, Mr. Yin Zhang, Dr. Kit Chan, Dr. Vincent Hung, Dr. Guowei Lu, Dr. Zhaoxin Wang, Ms. Yu Zhang, Mr. Jimmy Chan, Mr. Scott Tam, Ms. Yi Yang, Mr. Clement Cheung, Mr. Chi-Man Lee, Mr. Siu-Ting Ho, Mr. Siu-Sun Pun and Mr. Xiaofeng Sun. I would also like to thank Mr. Alex Siu for his technical assistance in hardware implementation of my projects and his help in solving many technical problems in electronics.

Finally, I am grateful to my parents and Ms. Jelly Cheung for their long-term support, tolerance and encouragement. I must also thank my beloved God. This thesis is dedicated to Him.

Abstract

The tremendous increase of data traffic in the worldwide Internet has driven the rapid development of optical networks to migrate from numerous point-to-point links towards meshed, transparent optical networks with dynamically routed light paths. This increases the need for appropriate network supervision methods. In view of this, optical performance monitoring (OPM) has emerged as an indispensable element for the quality assurance of an optical network. This thesis is devoted to the proposal of several new and accurate techniques to monitor different optical impairments so as to enhance proper network management.

When the optical signal is carried on fiber links with optical amplifiers, the accumulated amplified spontaneous emission (ASE) noise will result in erroneous detection of the received signals. The first part of the thesis presents a novel, simple, and robust in-band optical signal to noise ratio (OSNR) monitoring technique using phase modulator embedded fiber loop mirror (PM-FLM). This technique measures the in-band OSNR accurately by observing the output power of a fiber loop mirror filter, where the transmittance is adjusted by an embedded phase modulator driven by a low-frequency periodic signal. The robustness against polarization mode dispersion, chromatic dispersion, bit-rate, and partially polarized noise is experimentally demonstrated.

Chromatic dispersion (CD) is due to the fact that light with different frequencies travel at different speeds inside fiber. It causes pulse spreading and intersymbol interference (ISI) which would severely degrade the transmission performance. By feeding a signal into a fiber loop which consists of a high-birefringence (Hi-Bi) fiber, we experimentally show that the amount of experienced dispersion can be deduced from the

RF power at a specific selected frequency which is determined by the length of the Hi-Bi fiber. Experimental results show that this technique can provide high monitoring resolution and dynamic range.

Polarization mode dispersion (PMD) splits an optical pulse into two orthogonally polarized pulses traveling along the fiber at different speeds, causing crosstalk and ISI. The third part of the thesis demonstrates two different PMD monitoring schemes. The first one is based on the analysis of frequency-resolved state-of-polarization (SOP) rotation, with signal spectrum broadened by self-phase modulation (SPM) effect. Experimental results show that the use of broadened signal spectrum induced by SPM not only relaxes the filter requirement and reduces the computational complexity, but also improves the estimation accuracy, and extends the monitoring range of the pulsewidth. The second one is based on the delay-tap asynchronous waveform sampling technique. By examining the statistical distribution of the measured scatter plot, unambiguous PMD measurement range up to 50% of signal bit-period is demonstrated.

The final part of the thesis focuses on the monitoring of alignment status between the pulse carver and data modulator in an optical system. We again employ the two-tap asynchronous sampling technique to perform such kind of monitoring in RZ-OOK transmission system. Experimental results show that both the misalignment direction and magnitude can be successfully determined. Besides, we propose and experimentally demonstrate the use of off-center optical filtering technique to capture the amount of spectrum broadening induced by the misalignment between the pulse-carver and the data modulator in RZ-DPSK transmission system. The same technique was also applied to monitor the synchronization between the old and the new data in synchronized phase re-modulation (SPRM) system.

摘要

全球互聯網巨大的數據流量增長帶動了光網絡的迅速發展，由以往的點對點連接朝向使用動態路由光路的網狀透明光網絡演化，而這演化需要適當的網絡監管方案配合。鑑於此，光性能監測已成為保證光網絡質量不可或缺的一環。本論文將針對不同的光訊號缺陷提出新穎且準確的光性能監測技術，使網絡得到適當的管理。

當光訊號於設有光放大器的路徑傳輸時，累積的放大自發射噪聲會引致訊號接收錯誤。本論文的首部份報告一個全新、簡單、穩健、基於嵌入了相位調制器的光纖環路鏡的光訊噪比監測技術。這個技術使用低頻週期訊號調節光纖環路鏡的透射比，再透過觀察光纖環路鏡的輸出功率來量度帶內光訊噪比。實驗演示了這技術於偏振模色散、色散、不同碼率、部份偏振噪聲下的穩健性。

由於不同頻率的光於光纖中行走速度不一，訊號會產生色散現象，使脈衝散開。色散造成符號間干涉，嚴重降低傳輸性能。我們示範了透過把訊號放進由高雙折射光纖構成的光纖環路，訊號所遭受的色散，能由根據高雙折射光纖長度而選定了的射頻頻率的功率而計算出來。實驗結果顯示這技術能提供高解析度和高動態範圍。

偏振模色散把光脈衝一分為二，偏振正交地以不同速度行走，引致串音和符號間干涉。本論文的第三部份演示了兩個不同的偏振模色散監測方案：第一個方案建基於頻率分解偏振態旋轉分析技術，加上利用自相位調制現象來擴寬訊號頻譜，實驗結果顯示利用自相位調制現象而擴寬了的訊號頻譜，不單放寬了濾波器的要求和減低了計算複雜度，更改善了估算的準確度和擴大了可監測的脈寬範圍；第二個方案建基於延遲抽頭異步採樣技術，實驗顯示通過對散佈圖統計分佈的分析，此方案能準確地量度半個位元週期以內的偏振模色散。

本論文的最後一部份主要集中探討光系統中不同協作元件之間校直度的監

察技術。我們再次利用了延遲抽頭異步採樣技術，監測歸零開關鍵控傳送器中脈衝切割器和調制器之間的校直情況。實驗結果顯示這技術能同時監測校直方向和校直度。另外，我們提出並以實驗演示，使用偏移光過濾技術，能測量於歸零差分相移鍵控碼傳送器中因脈衝切割器和調制器之間未對準而產生的頻譜擴寬。同樣的技術，亦被應用於同步相位再調制系統中新舊訊息之間同步程度的監測。

Table of Contents

| | |
|--|----|
| Chapter 1 Introduction | 1 |
| 1.1 Overview | 1 |
| 1.2 Significance of Performance Monitoring | 2 |
| 1.3 Evolution of Performance Monitoring | 3 |
| 1.4 Optical Performance Parameters..... | 4 |
| 1.4.1 Signal Loss Monitoring..... | 5 |
| 1.4.2 Signal Alignment Monitoring..... | 6 |
| 1.4.3 Signal Quality Monitoring..... | 6 |
| 1.5 Requirements of OPM Techniques..... | 7 |
| 1.6 Major contribution of this thesis..... | 8 |
| 1.7 Outline of this thesis | 10 |
| Chapter 2 Optical Signal-to-Noise Ratio (OSNR) Monitoring | 11 |
| 2.1 Definition of OSNR..... | 11 |
| 2.2 Previously Proposed Schemes for OSNR Monitoring | 12 |
| 2.2.1 Out-of-band OSNR Monitoring Techniques..... | 13 |
| 2.2.1.1 Optical Spectral Analysis | 13 |
| 2.2.1.2 Arrayed Waveguide Grating/Tunable Filter Assisted Power Measurements..... | 14 |
| 2.2.1.3 RF Spectral Analysis | 15 |
| 2.2.2 In-band OSNR Monitoring Techniques..... | 16 |
| 2.2.2.1 In-band RF Spectral Analysis | 16 |
| 2.2.2.2 Polarization-Assisted OSNR Monitoring..... | 18 |
| 2.2.2.3 Interferometric Approaches | 23 |
| 2.3 OSNR Monitoring using Phase-Embedded Fiber Loop Mirror (PM-FLM) | 24 |
| 2.3.1 Principle of Proposed Technique | 25 |
| 2.3.2 Experimental Results and Discussion | 29 |
| 2.4 Summary..... | 36 |
| Chapter 3 Chromatic Dispersion (CD) Monitoring..... | 37 |
| 3.1 Management of Fiber Chromatic Dispersion | 37 |
| 3.2 Previously Proposed Schemes for CD Monitoring..... | 40 |

| | | |
|-----------|---|----|
| 3.2.1 | Sub-carrier Ratio Method | 41 |
| 3.2.2 | Clock Tone Analysis | 42 |
| 3.2.3 | Sideband Optical Filtering | 43 |
| 3.3 | Chromatic Dispersion Monitoring Using Birefringent Fiber Loop (BFL) | 44 |
| 3.3.1 | Principle of Proposed Technique | 44 |
| 3.3.2 | Experimental Results and Discussion | 48 |
| 3.4 | Summary | 53 |
| Chapter 4 | Polarization Mode Dispersion (PMD) Monitoring | 54 |
| 4.1 | Overview of PMD | 54 |
| 4.2 | Previously Proposed Schemes for PMD Monitoring | 56 |
| 4.2.1 | PMD-Induced RF Dip Power Measurement | 56 |
| 4.2.2 | Subcarrier-Based RF Power Fading Measurement..... | 57 |
| 4.2.3 | Eye-Opening Penalty Monitoring..... | 58 |
| 4.2.4 | Phase Diversity Detection | 58 |
| 4.2.5 | Arrival Time Measurement of Polarization-Scrambled Light | 59 |
| 4.2.6 | Degree-of-Polarization (DOP) Monitoring | 59 |
| 4.2.7 | Frequency-resolved SOP Rotation Monitoring | 61 |
| 4.3 | Enhanced PMD Monitoring with Frequency-resolved SOP Rotation by SPM..... | 63 |
| 4.3.1 | Experimental Results and Discussion | 65 |
| 4.3.2 | Input SOP Dependency Analysis | 71 |
| 4.4 | PMD Monitoring Using Delay Tap Asynchronous Waveform Sampling..... | 74 |
| 4.4.1 | Concept of Delay Tap Asynchronous Waveform Sampling | 76 |
| 4.4.2 | Experimental Results and Discussion | 76 |
| 4.5 | Summary..... | 79 |
| Chapter 5 | Modulation Alignment Monitoring | 81 |
| 5.1 | Generation of Return-to-Zero (RZ) Signal | 81 |
| 5.2 | Previously Proposed Schemes for Alignment Monitoring..... | 83 |
| 5.2.1 | Modulation-Misalignment-Induced RF DIP Power | |

| | |
|--|-----|
| Measurement..... | 83 |
| 5.2.2 Optical Spectral Asymmetry Measurement..... | 83 |
| 5.2.3 DOP Reduction Measurement..... | 84 |
| 5.3 RZ-OOK Alignment Monitoring Using Delay Tap Asynchronous Waveform Sampling | 85 |
| 5.3.1 Experimental Results and Discussion | 85 |
| 5.4 RZ-DPSK Alignment Monitoring Using Off-center Optical Filtering | 90 |
| 5.4.1 Principle of Proposed Technique | 91 |
| 5.4.2 Experimental Results and Discussion | 94 |
| 5.5 SPRM Alignment Monitoring Using Off-center Optical Filtering | 99 |
| 5.5.1 Introduction to SPRM..... | 99 |
| 5.5.2 Experimental Results and Discussion | 101 |
| 5.6 Summary..... | 105 |
| Chapter 6 Conclusions and Future Works | 106 |
| 6.1 Summary of the Thesis..... | 106 |
| 6.2 Future Works | 107 |
| Bibliography | 109 |
| Appendix – List of Publications | 121 |

List of Figures

| | |
|--|----|
| Fig. 1.1. A long-haul network with OPM. DGE: Dynamic Gain Equalizer, OPM: Optical Performance Monitor, AWG: Array Waveguide Grating..... | 4 |
| Fig. 1.2. The broad spectrum of OPM (Adapted from Ref. [13])..... | 5 |
| Fig. 2.1. OSNR measurement in DWDM system..... | 11 |
| Fig. 2.2. Out-of-band noise level may not be equal to in-band noise level in spectrum-interpolated noise measurement..... | 14 |
| Fig. 2.3. (a) Graphical representation of the generation of an RF spectral dip due to destructive interference when there is PMD (b) OSNR monitoring module by orthogonal delayed-homodyne method..... | 17 |
| Fig. 2.4. Principle of OSNR monitoring using polarization extinction | 19 |
| Fig. 2.5. (a) OSNR monitoring module using polarization nulling (b) Monitoring results in a back-to-back configuration for six NRZ channels with errors < 0.4dB (Adapted from Ref. [33])..... | 19 |
| Fig. 2.6. (a) DOP-based OSNR monitoring module (b) Monitoring errors in a back-to-back configuration with errors <1 dB up to 25dB/0.1nm (Adapted from Ref. [34])..... | 20 |
| Fig. 2.7. (a) Impact of PMD on Polarization-Nulling; OSNR for (b) polarization-nulling and (c) DOP-based OSNR monitoring under different DGD values (Adapted from Ref. [37])..... | 21 |
| Fig. 2.8. OSNR measurement error by induced by ASE polarization, with ASE polarization state (a) aligned, and (b) orthogonal to signal polarization (Adapted from Ref. [43])..... | 22 |
| Fig. 2.9. OSNR monitor based on a 1-bit delay interferometer (Adapted from Ref. [44])..... | 24 |
| Fig. 2.10. Schematic diagram of the proposed OSNR monitoring module. PC: polarization controller, BPF: optical bandpass filter..... | 25 |
| Fig. 2.11. Illustrated PM-FLM transfer function when (a) destructive and (b) constructive interference for data signal occurs..... | 26 |
| Fig. 2.12. Experimental setup. PC: polarization controller, ATT: optical attenuator, OSA: optical spectrum analyzer, EDFA: erbium doped fiber amplifier..... | 30 |
| Fig. 2.13. Output optical spectra (a) without, and (b) with optical bandpass filter at the monitoring module input..... | 31 |
| Fig. 2.14. Measured OSNR and monitoring errors..... | 31 |

| | |
|--|----|
| Fig. 2.15. OSNR monitoring results in a 150-km SMF link (PMD <1.5ps, P _{out} =1 and 10dBm respectively)..... | 32 |
| Fig. 2.16. Monitoring errors under different DGDs for 25-dB OSNR..... | 33 |
| Fig. 2.17. Monitoring errors for partially polarized ASE with different DOPs and alignment (dark for parallel, white for orthogonal) to signal for 25-dB OSNR) | 34 |
| Fig. 2.18. Measured OSNR (circles) and monitoring errors (squares) for polarized ASE (DOP=99.69%) which is parallel (dark) or orthogonal (white) to signal..... | 34 |
| Fig. 2.19. Monitoring errors under different bit-rates for 25-dB OSNR.. | 35 |
| Fig. 2.20. Measured OSNR and monitoring errors for 2.5-Gbps data rate | 35 |
| Fig. 3.1. (a) Dispersion tolerance range using fixed and tunable compensator (b) change in the accumulated dispersion as a function of the temperature fluctuations and fiber length (Adapted from Ref. [51]) | 40 |
| Fig. 3.2. Sub-carrier based CD monitoring (Adapted from Ref. [2])..... | 41 |
| Fig. 3.3. (a) Fading for subcarriers with two different frequencies and (b) the fading ratio of the two subcarriers (Adapted from Ref. [2]) | 42 |
| Fig. 3.4. Clock regenerating effect in NRZ systems and clock fading effect in RZ systems under dispersion (Adapted from [52]) | 42 |
| Fig. 3.5. CD monitoring using sideband optical filtering (Adapted from Ref. [53])..... | 43 |
| Fig. 3.6. Schematic diagram of the proposed chromatic dispersion monitoring module, with experimental setup for demonstration. IM: intensity modulator, EDFA: erbium-doped fiber amplifier, BPF: optical bandpass filter, SMF: single-mode fiber, DCF: dispersion compensating fiber, PC: polarization controller..... | 45 |
| Fig. 3.7. Optical amplitude and phase responses of a BFL at its output. | 46 |
| Fig. 3.8. Transmittance of the birefringent fiber loop..... | 49 |
| Fig. 3.9. RF spectrum at BFL output for signals with (a) 0 ps/nm, (b) 110 ps/nm and (c) 450 ps/nm accumulated dispersion..... | 50 |
| Fig. 3.10. Received RF power at 5GHz as a function of dispersion obtained by experiment (10 Gbit/s NRZ OOK data) and equation 3.5..... | 50 |
| Fig. 3.11. Measured RF power at 5GHz vs DGD with data rate of 10 Gbit/s and accumulated dispersion of 340 ps/nm..... | 51 |
| Fig. 3.12. Received RF power at 5GHz as a function of dispersion (40 Gbit/s NRZ OOK data) | 51 |

| | |
|---|----|
| Fig. 3.13. Measured RF power at 5GHz vs DGD with data rate of 40 Gbit/s and accumulated dispersion of 0 ps/nm and 340 ps/nm | 52 |
| Fig. 3.14. Modified design enabling the measurement of both the magnitude and sign of the link's dispersion..... | 53 |
| Fig. 4.1. Graphical representation of the DGD between the two PSPs caused by intrinsic geometric asymmetry and extrinsic mechanical stress-induced asymmetry of the fiber core..... | 55 |
| Fig. 4.2. Eye diagrams at PMD equals (a) 0, (b) 2T/5, (c) 3T/5, (d) 4T/5, where T is the bit period and pulse width is $\sim 0.28T$ | 56 |
| Fig. 4.3. (a) Proposed different frequency components for PMD monitoring (b) Received RF power variation versus DGD for 1/8, quarter, half, and bit rate frequency components (Adapted from Ref. [69]) | 57 |
| Fig. 4.4. Time-domain explanation of the depolarization effect for different pulse widths under the same DGD..... | 60 |
| Fig. 4.5. Theoretical results of minimum DOP versus DGD (relative to the bit time, T_b) as the pulse width (W) of an RZ signal varies, assuming ideal rectangular pulse..... | 60 |
| Fig. 4.6. Frequency-domain explanation of the depolarization effect for different pulse widths under the same DGD | 62 |
| Fig. 4.7. The operation principle of PMD monitoring based on the frequency-resolved SOP rotation. $\Delta f=f_1-f_2$, $S(f_1)$, $S(f_2)$ are the output polarization states at frequencies f_1 and f_2 , respectively | 63 |
| Fig. 4.8. Experimental setup of PMD monitoring with the assistance of SPM effect, PC: polarization controller, MOD: modulator, DSF: dispersion shifted fiber..... | 65 |
| Fig. 4.9. (a) The spectrum of the signal with 28-ps FWHM pulsewidth (i) without SPM, (ii) with SPM, $P_{in}=20\text{dBm}$; (b) The measured DGD values by analyzing frequency-resolved SOP rotation with/without SPM effect versus the reference DGD values for the 28-ps FWHM pulsewidth signal | 67 |
| Fig. 4.10. The spectra of the signal with 2.5-ps FWHM pulsewidth (i) without SPM (ii) with SPM, $P_{in}=10\text{dBm}$ (iii) with SPM, $P_{in}=20\text{dBm}$ | 69 |
| Fig. 4.11. The measured DGD values by analyzing frequency-resolved SOP rotation with/without SPM effect versus the reference DGD values for the 2.5-ps FWHM pulsewidth signal. | 69 |
| Fig. 4.12. The SOP trajectories on Poincare sphere (X: Start Point; O: End Point), (a) when DGD is 15.2ps and the wavelength scanning range is 0.4nm, and (b) when DGD is 5ps and the wavelength scanning range is 1 nm, (i) without SPM, (ii) with SPM, $P_{in}=10\text{dBm}$, and (iii) with SPM, | |

| | |
|---|----|
| $P_{in}=20dBm$ | 71 |
| Fig. 4.13. Illustration of the relationship between input DOP and PSP . | 72 |
| Fig. 4.14. The minimum measurable DGD for different angles between input SOP and PSP..... | 74 |
| Fig. 4.15. (a) Delay-tap asynchronous sampling. T_s =sampling period, t =timing offset within each sampling. (b) A sample delay-tap scatter plot for RZ-OOK signal at Δt =bit-period..... | 76 |
| Fig. 4.16. Experimental setup. EAM: electro-absorption modulator; ODL: optical delay line; IM: intensity modulator | 77 |
| Fig. 4.17. Two-tap scatter plots under different DGD values..... | 78 |
| Fig. 4.18. Measured plots for parameter m at different DGD values | 79 |
| Fig. 5.1. Modulation output when pulse carver and data modulator are (a) properly aligned, and (b) misaligned. | 81 |
| Fig. 5.2. RF power spectrum when pulse carver and data modulator are (a) aligned and (b) misaligned (Adapted from Ref. [90]) | 83 |
| Fig. 5.3. Solid (dashed) curve is the measured optical when the pulse carver leads (lags) the data modulator by 20 ps. (Adapted from Ref. [91]) | 84 |
| Fig. 5.4. Modulation alignment monitoring in RZ-DPSK systems by measuring DOP reduction (Adapted from Ref. [92])..... | 85 |
| Fig. 5.5. Experimental setup. EAM: electro-absorption modulator; ODL: optical delay line; IM: intensity modulator | 86 |
| Fig. 5.6. Power penalty vs timing misalignment for RZ-OOK system with 28-ps pulsewidth..... | 87 |
| Fig. 5.7. Eye diagrams for the signal with different modulation misalignments. | 87 |
| Fig. 5.8. Two-tap scatter plots for different modulation timing misalignments | 88 |
| Fig. 5.9. d and t for different misalignment obtained by (a) experiment, and (b) simulation using <i>OptSimTM</i> | 89 |
| Fig. 5.10. (a) Illustration of timing alignment between pulse carver and data modulator. (b) Calculated signal spectra with timing alignment between pulse carver and data modulator of (i) 0, (ii) $0.3T$, and (iii) $0.5T$ in a 10-Gb/s RZ-DPSK system with $\sim 0.28 \cdot T$ pulsewidth | 92 |
| Fig. 5.11. Proposed alignment module. EAM: electroabsorption modulator; PM: phase modulator; DI: delay interferometer; BPF: bandpass filter ... | 94 |

| | |
|---|-----|
| Fig. 5.12. Power and BER for different timing misalignments. Insets: Degraded eye diagrams due to misalignment of (a) -32 ps and (b) 32 ps | 95 |
| Fig. 5.13. Optical spectra for perfect alignment (solid line) and worst-case misalignment (dashed line). Inset: Eye diagrams | 96 |
| Fig. 5.14. MPDR for different filter offsets | 97 |
| Fig. 5.15. Output monitoring power for different timing misalignments | 98 |
| Fig. 5.16. Principle of SPRM to simultaneously erase old DPSK data and write new DPSK data. Inset: constellation diagram for DPSK | 100 |
| Fig. 5.17. Experimental setup. Insets: the eye diagrams of the new DPSK signal after balanced detection for (a) the best case of phase re-modulation in NRZ-DPSK format; (b) the worst case of phase re-modulation in NRZ-DPSK format; (c) the best case of phase re-modulation in RZ-DPSK format; and (d) the worst case of phase re-modulation in RZ-DPSK format. | 101 |
| Fig. 5.18. The spectra of the new DPSK signal versus the wavelength offset with respect to the central wavelength of the DPSK signal under the best case (solid) and the worst case (dashed) of phase re-modulation for (a) NRZ-DPSK and (b) RZ-DPSK formats. | 102 |
| Fig. 5.19. The MPDR versus the wavelength offset of the OBPF with respect to the central wavelength of the DPSK signal for NRZ-DPSK (solid) and RZ-DPSK (dashed) formats | 103 |
| Fig. 5.20. The relative monitoring power versus re-modulation misaligned time for (a) NRZ-DPSK and (b) RZ-DPSK formats. The central wavelength of the OBPF is optimized and the relative monitoring power is with respect to the monitoring power for the best case of phase re-modulation. | 104 |

List of Tables

| | |
|---|----|
| Table 3.1. Overview of commercially available dispersion compensation devices (Adapted from Ref. [51]) | 38 |
| Table 4.1. Comparison between the two proposed PMD monitoring schemes: (1) Enhanced Frequency-Resolved SOP Rotation Analysis and (2) Delay-tap Asynchronous Waveform Sampling | 79 |

Chapter 1 Introduction

1.1 Overview

During the past decade, we have been witnessing tremendous changes in the demand and usage pattern of telecommunication networks. On one hand, the total demand for network bandwidth has been growing rapidly. On the other hand, most of the growth originates not from circuit voice traffic, but from Internet-based data traffic. As the Internet user base continues to grow and new content-rich network applications such as video on demand (VOD), multimedia gaming, video teleconference and electronic business continue to emerge, network capacity demands will undoubtedly increase further. It is well known that the characteristic of data traffic is contrastingly different from voice, exhibiting highly bursty traffic demand and dynamic end-to-end connection pattern [1]. These fundamental trends are already having a profound impact on telecommunication networks and have triggered an evolution throughout the optical network.

In addition to high capacity, optical networks are becoming more and more dynamically re-configurable. The signals may traverse over different complex paths consisting of different fibers, amplifiers, optical add/drop multiplexers (OADM), optical cross-connects (OXC), and plenty of other network elements. The transmission path and the add/drop of channels may change from time to time. Besides, future optical networks will be transparent, meaning that they can accommodate signals with different protocols including SONET/SDH, Gigabit Ethernet, ATM, IP over WDM, and etc. The increasing complexity of optical networks makes the data

transmission vulnerable to network malfunctions, misconfigurations, and signal impairments. In order to manage such high capacity and highly dynamic transparent optical networks, performance monitoring systems [9] are necessary, as they can help to identify network degradation and prevent system and network failure that would otherwise translate to colossal financial loss for both service providers and customers.

1.2 Significance of Performance Monitoring

Performance monitoring systems serve a number of important network functions that spans at least the following:

- *Active time-varying distortion monitoring and compensation* – The performance monitors can be used to provide direct feedback for adaptive compensators. Some examples include PMD compensation, distortion compensation, and dynamic gain equalization (DGE) for amplifiers [7], [8]
- *Fault forecasting, detection, localization, isolation, and resilience mechanism activation* – The performance monitors can be used to anticipate major degradations of components like erbium-doped fiber amplifiers (EDFA), OADM, and OXC, as well as changes in working conditions after the initial service rollout. Protection and restoration mechanisms will be triggered within timing limits when necessary [6]-[7].
- *Intelligent path provisioning and traffic routing* – For example, high capacity and priority traffic can be dynamically tuned to high-performance optical channels. In addition, channel commissioning and topology discovery can also be achieved based on performance monitoring [4]-[5], [8].
- *Signal quality characterization for quality of service (QoS) assurance and service level agreement (SLA) fulfillment* – Under the terms of

SLA, the service providers guarantee a measurable QoS to customers. These QoS measures may be in terms of committed network availability, provisioning time, target repair time and procedures and a host of others. If the conditions in the agreement are violated, the carriers will typically provide a rebate to the customers. Performance monitoring enabled QoS measurements will present new opportunities for revenue and competitive differentiation for the service providers [3], [6].

1.3 Evolution of Performance Monitoring

In traditional SONET/SDH (synchronous optical network/synchronous digital hierarchy) networks, optical/electrical/optical (O/E/O) conversion in the data path is typically required for performance monitoring. Bit/block error rates (BERs) at SONET line terminating elements (LTEs) are determined by bit interleaved parity-8 (BIP-8) technique [9]-[12]. Q-factor is also determined from bits interleaved within SONET frames with or without simple loss of signal (LOS) monitoring by power monitors. The signal-to-noise (SNR) degradations and distortions in active and passive components are usually measured in advance [2]. As a result the efficacy of the performance monitoring metrics rests on the assumptions that the networks are opaque and static.

Future optical networks, however, have a number of characteristics described in Section 1.1 that drive the need for a new paradigm of more advanced monitoring techniques called optical performance monitoring (OPM). Since future optical networks will be all-optical, transparent, and dynamically reconfigurable, the monitoring schemes should therefore be non-intrusive, with no need to decode the overhead information, insensitive to signal origins and its transport path history, be on a

per-channel basis, and tie closely with adaptive compensation techniques to provide optimum system conditions in a dynamic manner. In addition, the optical performance parameters to be monitored should be widely extended to facilitate fast and accurate failure root cause analysis.

1.4 Optical Performance Parameters

Today the deployment of OPM is still in its embryonic stage. Current mass deployed performance monitors typically provide information on parameters including (i) aggregate signal power, (ii) individual component's health status such as amplifier pump laser power or temperature controller limits, and (iii) individual channel power, presence, wavelength, and/or spectrum-interpolated optical signal-to-noise ratio (OSNR) [6]-[7]. An illustration of a long-haul network with OPM is shown in Fig. 1.1. These parameters, however, represent only a small part of the overall monitoring picture. As networks continue to evolve to higher-speed with more channel counts to longer distance, more advanced OPM is necessary. Fig. 1.2 shows the broad spectrum of OPM with the plethora of parameters to be monitored classified into three categories: signal loss, signal alignment, and signal quality [13].

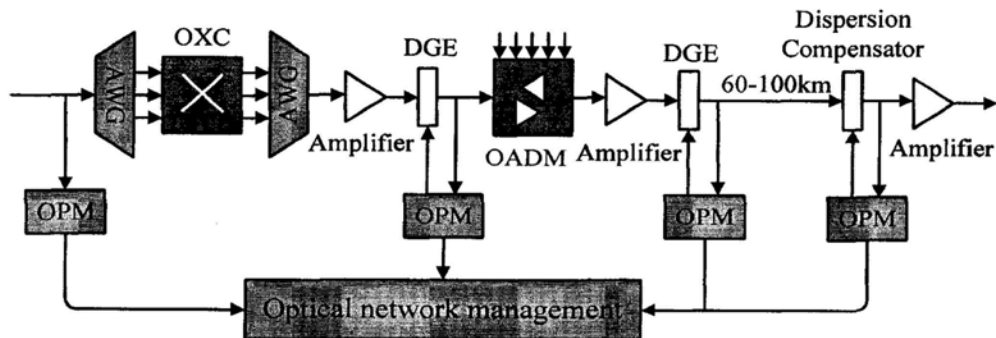


Fig. 1.1. A long-haul network with OPM. DGE: Dynamic Gain Equalizer, OPM: Optical Performance Monitor, AWG: Array Waveguide Grating

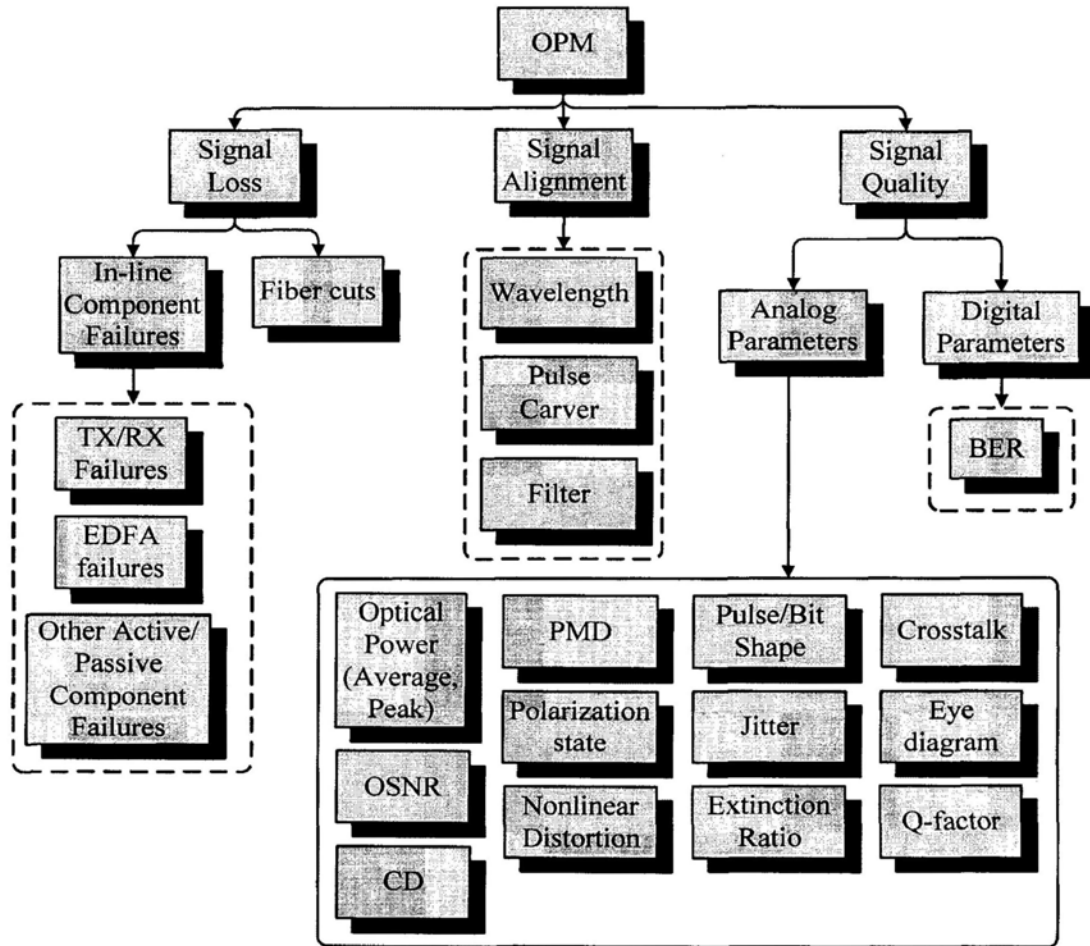


Fig. 1.2. The broad spectrum of OPM (Adapted from Ref. [13])

1.4.1 Signal Loss Monitoring

Signal loss monitoring refers to the monitoring of in-line component failures and fiber cuts that can cause the power loss of the whole channel [6]. Component failures may be defined as a change in opacity (e.g. >2 dB) and they include individual or multiple component malfunctions and improperly installed or configured equipment. The faulty components may be active ones, such as transmitters, receivers, and optical amplifiers, i.e. pump laser failure, or passive ones, such as arrayed-waveguide grating

(AWG). On the other hand, fiber cuts are the damage to the network fibers due to accidents, periodic repair and maintenance, and deliberate malicious attack. Signal loss monitoring schemes are typically referred to as optical surveillance schemes.

1.4.2 Signal Alignment Monitoring

Signal alignment monitoring refers to the monitoring of alignment of signal wavelength, filter position, and pulse carver. These frequency and time domain alignments are used to ensure that the transmission and the reception of signal are maintained in a proper condition.

1.4.3 Signal Quality Monitoring

Signal quality monitoring refers to the monitoring of a host of disparaging effects of optical transmission that must be minimized or controlled [6]. The transmission impairments can be classified into three broad categories:

- (i) Noise, which is the random signal fluctuations that are often treated as a Gaussian process,
- (ii) Distortion, which is the modification of signal waveform due to fiber nonlinearities or fiber dispersion effects, and
- (iii) Jitter, which is the fluctuation in the time registration of the bits.

These notable transmission impairments include amplifier noise, amplifier distortion and transients, chromatic dispersion (CD), polarization mode dispersion (PMD), polarization dependent gain (PDG), polarization dependent loss (PDL), fiber nonlinearity induced distortion and crosstalk including self-phase modulation (SPM), cross-phase modulation (XPM), four-wave mixing (FWM), stimulated Rayleigh

scattering (SRS), and stimulated Brillouin scattering (SBS), timing jitter, multi-path interference (MPI) effects, pump laser RIN transfer, optical filter distortion, and linear crosstalk. In response to these impairments, OPM has been vigorously pursued in laboratories to provide the following physical layer measurements [2], [6]:

- 1) average power (per wavelength or aggregate);
- 2) peak power;
- 3) optical signal-to-noise ratio;
- 4) chromatic dispersion;
- 5) polarization-mode dispersion (first and higher order);
- 6) polarization state;
- 7) nonlinear distortion;
- 8) pulse/bit shape;
- 9) jitter;
- 10) extinction ratio;
- 11) crosstalk;
- 12) eye diagram;
- 13) Q-factor;
- 14) BER;

The above list is, however, by no means exhaustive as new performance metrics always emerge as optical networking technologies advance.

1.5 Requirements of OPM Techniques

To be effective, any monitoring technique should satisfy some general requirements [14], [15]-[16]. These can be classified into technical requirements, commercial requirements, and value-added options.

- *Technical requirements* – From the technical perspective, desirable OPM options should have signal degradation discovery capability, transparency in terms of bit rate, modulation format, and protocol, non-intrusiveness (in-service measurement), high update speed, accuracy, reliability, and stability.
- *Commercial requirements* – From the commercial perspective, desirable OPM options should have low production cost, low power consumption, compactness, simplicity, and interoperability between different vendors. Cost is the major concern here as the capital expense due to OPM must be recovered through savings over time in operational expenses. In 2004, the total market for embedded OPMs is on the order of US\$10-20 million. Unfortunately, price has continued unabated to the point where a 100-GHz-capable OPM in moderate volume is selling for about US\$3,000 [8]. A positive sign may be that many recent optical technologies such as tunable filters and spectrometers have become available and made many OPM options more economical [6].
- *Value-added options* – An increasing focus of OPM development is placed on comprehensiveness (whether the OPM option can monitor multiple parameters simultaneously), fault localization capability (whether the OPM option can locate the source of degradation), and scalability (whether the OPM option can adapt to high data-rate systems).

1.6 Major contribution of this thesis

In this thesis, we address some of the most challenging problems in OPM, including optical signal-to-noise ratio (OSNR), chromatic dispersion (CD), polarization mode dispersion (PMD) and component alignment monitoring.

We propose and investigate several novel OPM schemes for these parameters with the aim of facilitating proper network management.

For optical signal-to-noise ratio (OSNR) monitoring, we propose and investigate a novel, simple, and robust in-band optical signal to noise ratio (OSNR) monitoring technique using phase modulator embedded fiber loop mirror (PM-FLM). This technique measures the in-band OSNR accurately by observing the output power of a fiber loop mirror filter, where the transmittance is adjusted by an embedded phase modulator driven by low-frequency periodic signal. The robustness against polarization mode dispersion, chromatic dispersion, bit-rate, and partially polarized noise is experimentally demonstrated.

For chromatic dispersion (CD) monitoring, our focus is on the use of birefringence fiber loop (BFL) to facilitate chromatic dispersion monitoring based on RF spectrum analysis. By feeding a signal into a fiber loop which consists of a high-birefringence (Hi-Bi) fiber, we experimentally show that the amount of experienced dispersion can be deduced from the RF power at a specific selected frequency which is determined and adjustable by the length of the Hi-Bi fiber. Experimental results show that this technique can provide high monitoring resolution and dynamic range.

For polarization mode dispersion (PMD) monitoring, we demonstrate two different PMD monitoring schemes. The first one is based on the analysis of frequency-resolved state-of-polarization (SOP) rotation, with signal spectrum broadened by self-phase modulation (SPM) effect. Experimental results show that the use of broadened signal spectrum induced by SPM not only relaxes the filter requirement and reduces the computational complexity, but also improves the estimation accuracy, and extends the monitoring range of the pulsewidth. The second one is based

on the delay-tap asynchronous waveform sampling technique. By examining the statistical distribution of the measured scatter plot, unambiguous PMD measurement range up to 50% of signal bit-period is demonstrated.

For alignment monitoring, we employ the delay-tap asynchronous sampling technique to monitor the pulse carver and data modulator misalignment in RZ-OOK transmission system. Experimental results show that both the misalignment direction and magnitude can be successfully determined. Besides, we propose and experimentally demonstrate the use of off-center optical filtering technique to capture the amount of spectrum broadening induced by the misalignment between the pulse-carver and data modulator in RZ-DPSK transmission system. The same technique was also applied to monitor the synchronization between old and new data in synchronized phase re-modulation (SPRM) system.

1.7 Outline of this thesis

The organization of the remaining chapters will be as following:

Chapter 2: Introduction to our proposed OSNR monitoring scheme based on phase modulator embedded fiber loop mirror (PM-FLM).

Chapter 3: Introduction to our proposed CD monitoring scheme based on birefringent fiber loop (BFL).

Chapter 4: Demonstrates our two proposed PMD monitoring schemes based on SPM-enhanced frequency-resolved SOP analysis and delay-tap asynchronous sampling.

Chapter 5: Describes the issue of component misalignment and our proposed alignment monitoring schemes using delay-tap asynchronous sampling technique and off-center optical filtering.

Chapter 6: Conclusions and future works.

Chapter 2 Optical Signal-to-Noise Ratio (OSNR) Monitoring

2.1 Definition of OSNR

According to TIA-EIA-526-19 standard [17], the definition of OSNR is $10\log(P_{\text{sig}}/P_{\text{ase}})$, where P_{sig} is the signal power measured with an optical filter with 3-dB bandwidth large enough to cover the whole signal spectrum, i.e. 0.2 nm for 10-Gb/s NRZ signal, and P_{ase} is the noise measured with an optical filter of known noise equivalent bandwidth (NEB). P_{ase} is typically referenced to 0.1-nm NEB, although a 1-nm NEB is sometimes used (Fig. 2.1).

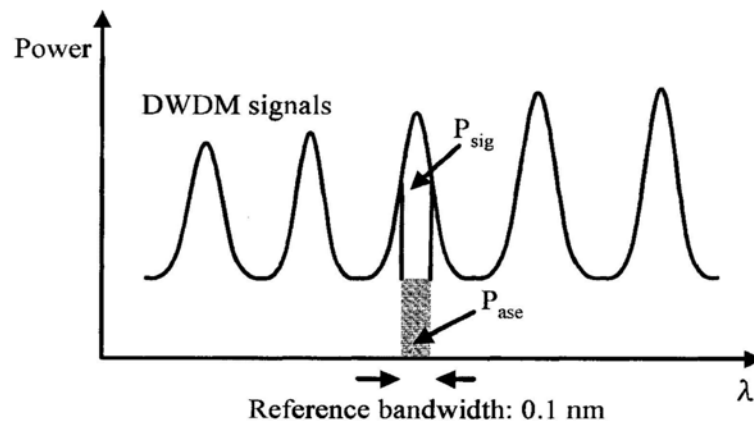


Fig. 2.1. OSNR measurement in DWDM system

OSNR is important because it suggests a degree of impairment when the optical signal is carried in links with optical amplifiers. Optical

amplifiers introduce additional impairments because the accumulated amplified spontaneous emission (ASE) noise will contribute electrical noise after O/E conversion in the receivers. In practice, the use of amplifiers will improve the signal as the increase in the signal amplitude will help overcome the noise generated in the receiver's front end. However, the optical background noise that accompanies the desired optical signal will be amplified along with signal as well. Consequently, the OSNR will tend to degrade as it passes through the transmission system [18]. One of the consequences of having low OSNR is that no matter how strong the signal presented to a good receiver, there will be errors associated with the presence of the ASE. Thus, there exists a minimum acceptable OSNR for a given BER [19].

As a result of the above property, OSNR has been vigorously pursued as an important analog performance metric for (i) link setup, control, and optimization, such as tuning a dynamic gain equalizer [7], (ii) in-service signal quality characterization for QoS assurance [20], (iii) correlation with end-terminal BER for fault management purposes [21], and (iv) path performance prediction for intelligent routing [5][6].

2.2 Previously Proposed Schemes for OSNR Monitoring

Desirable OSNR monitoring techniques should be simple, accurate, low-cost, with large dynamic range and sensitivity, and requiring low monitoring power. To date, numerous OSNR monitoring techniques have been proposed and they can be classified as out-of-band, in which the ASE noise is measured outside the channel bandwidth, or in-band, in which the ASE noise is measured within the channel bandwidth [14].

2.2.1 Out-of-band OSNR Monitoring Techniques

2.2.1.1 Optical Spectral Analysis

One of the most commonly used techniques for out-of-band OSNR monitoring is optical spectral analysis (OSA). A small portion ($\sim 1\text{-}5\%$) of the transmitted optical signal is tapped and sent to an optical spectrum analyzer. The ASE noise spectrum lying between the channels can be used to derive an estimate of the in-band ASE noise by linear interpolation. However, there are two general cases in which spectral monitoring becomes problematic: dense WDM channel packing and dynamic reconfigurable networks [22]. For networks with dense WDM channel spacing, such as 10-Gb/s RZ modulated channels on a 50-GHz ITU grid, there is insufficient spectrum available for monitoring between the channels and the OSNR measurement is hindered by crosstalk from adjacent channels. For dynamic reconfigurable networks, each channel may traverse a different route with a different number of erbium-doped fiber amplifiers (EDFAs), optical cross-connect (OXC), and optical add-drop multiplexer (OADM). Thus, each channel may experience unequal EDFA gain and different background shaping by the filters of OXC and OADM. The upshot is that the out-of-band ASE noise may not be equal to the in-band ASE noise (Fig. 2.2). Besides, OSNR monitoring using a high-resolution OSA is costly, bulky, and inconvenient. To solve the last problem, several more compact out-of-band approaches based on arrayed-waveguide-grating (AWG) or tunable filters have been proposed.

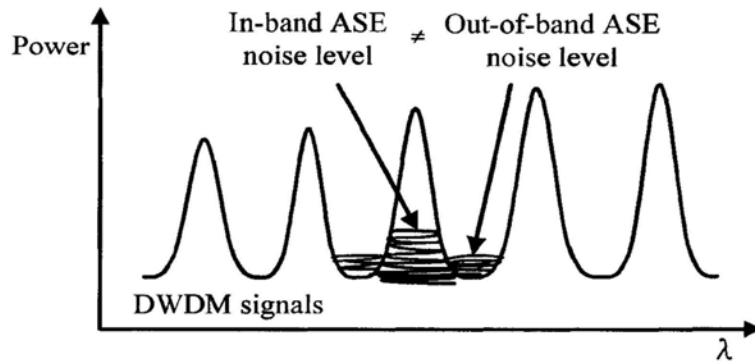


Fig. 2.2. Out-of-band noise level may not be equal to in-band noise level in spectrum-interpolated noise measurement

2.2.1.2 Arrayed Waveguide Grating/Tunable Filter Assisted Power Measurements

An AWG module monolithically integrated with eight photodiodes was proposed in [23] to realize a compact OSNR monitor. The WDM signals are tapped and demultiplexed into individual signal wavelengths by the AWG. The power of each channel is then detected and converted into a corresponding voltage by the photodiode. This voltage is proportional to the sum of the signal and the ASE noise power of that channel. On the other hand, one of the ports of AWG is left unused and the voltage detected is proportional to the ASE noise power. With these two parameters, the OSNR can be calculated. However, the major problem of using AWG is the crosstalk issue when the number of channel is large. To reduce the crosstalk, a double-resolution-AWG-based OSNR monitoring circuit was further proposed [24]. The OSNR could be monitored up to 37.5dB/0.1nm with <1-dB errors.

Another commonly used component in place of AWG is tunable filter [25]-[26]. The optical filtering approach usually uses two optical filters alternately: one with wide enough bandwidth to accommodate the signal

spectrum for measuring the signal power and the other with narrow enough bandwidth to reject the adjacent channels for measuring the noise power. However, this requires filter with very deep transfer function for noise measurement. Recently, OSNR monitoring based on double-pass filtering and dithered tunable reflector has been proposed to solve this problem [27]. The OSNR can be monitored up to 44-dB/0.1nm with errors <0.4 dB.

2.2.1.3 RF Spectral Analysis

Another approach to out-of-band OSNR monitoring is to make use of the RF spectrum of the signal. This involves monitoring of the signal power using an optical power meter and the electrical noise using an RF spectrum analyzer at spectral null locations at which the signal is not present. Both low-frequency (40-50 kHz) and high frequency (e.g. 9.8 GHz for 2.5 Gb/s signal) spectral null regions have been proposed in this regard [28]-[29]. OSNR monitoring using RF spectrum is simple and potentially low-cost. However, low-frequency monitoring is susceptible to low-frequency noise tails that would exaggerate the strength of the noise. Moreover, it is suitable for signal with short pattern length only. On the other hand, high-frequency monitoring tends to suffer crosstalk from adjacent channels and may require high-speed RF spectrum analyzer as the data rates go up.

Alternatively, a subcarrier can be added out-of-band of the signal spectrum. The OSNR of the signal can be correlated to the electrical carrier-to-noise ratio (CNR) of the subcarrier [2]. This scheme is simple and allows simultaneous monitoring of multiple channels. However, the measurements are sensitive to dispersion effects such as CD and PMD due to high-frequency fading and the subcarrier consumes extra bandwidth.

2.2.2 In-band OSNR Monitoring Techniques

As we have discussed in Section 2.2.1.1, out-of-band OSNR monitoring is unreliable in dynamic reconfigurable networks and systems with tight wavelength spacing. Many approaches have thus been proposed to measure the in-band noise. All these methods rely on at least one of the following properties to differentiate the signal and the noise: (i) signal is polarized while noise is unpolarized, (ii) signal is coherent while noise is incoherent, (iii) signal and noise have different duty cycles, and (iv) signal and noise are differently distributed in the phase space.

2.2.2.1 In-band RF Spectral Analysis

One of the approaches for in-band OSNR monitoring is to use in-band RF spectral analysis. There are two methods proposed: orthogonal delayed-homodyne method and half clock frequency constellation monitoring.

(A) Orthogonal Delayed Homodyne Method

In orthogonal delayed homodyne method [30], a PMD emulator is added at the monitoring module and the PMD introduced will cause any given optical frequency component to split between the two orthogonal modes called principal states of polarization (PSP) and propagate down the fiber at different speeds. This speed differential, called the differential group delay (DGD), will dephase the given frequency component on each PSP with respect to the carrier and will generate a dip in the electrical spectrum after detection due to destructive interference (Fig. 2.3). When the signal is launched at 45° (in Jones Space) relative to the PSPs, the minimum dip frequency is related to the DGD introduced by the PMD

emulator by $f_{\min} = 1/(2 \cdot DGD)$. By measuring this narrowband RF dip power (i.e. the electrical noise) using an RF spectrum analyzer, together with the total optical power measured by an optical power meter, the OSNR can be calculated [28]. This method is simple and can deal with considerable values of PMD. However, it requires a high rate of spectral analysis, obtains spectral nulling of the signal in a very localized region that contains a small amount of energy, and is sensitive to chromatic dispersion.

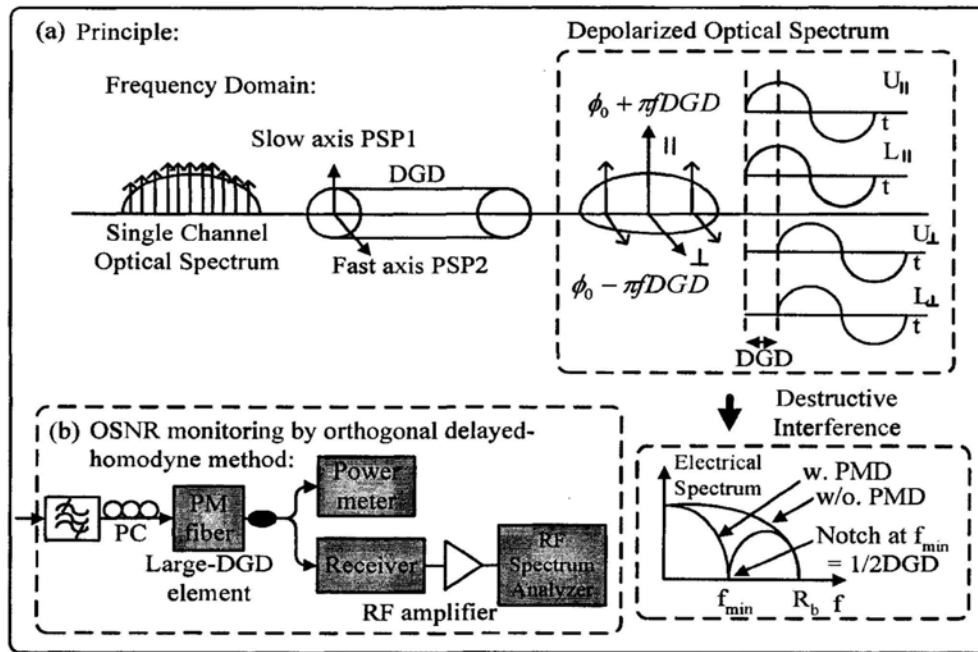


Fig. 2.3. (a) Graphical representation of the generation of an RF spectral dip due to destructive interference when there is PMD (b) OSNR monitoring module by orthogonal delayed-homodyne method

(B) Half Clock Frequency Constellation Monitoring

Half clock frequency constellation monitoring uses an analysis of a narrow bandwidth of the electrical data spectrum at precisely half the data clock frequency [31]. The half clock frequency component is found to have the

nice property that it is conjugate symmetric, thus if an RF demodulation is done, the resulting demodulated signal will appear along a single axis in the demodulated phase-space. The SNR can then be derived by taking the ratio of the length of the line to its width, and the OSNR can be finally correlated with the SNR. As this technique is inherently narrowband, it offers the advantage of very high sensitivity (avoiding the requirement of optical pre-amplification). However, it is fairly complicated and is sensitive to chromatic dispersion. It also has small dynamic range, and cannot detect narrowband signal degradations that occur at frequencies other than the half-clock.

2.2.2.2 Polarization-Assisted OSNR Monitoring

Polarization-assisted OSNR monitoring is based on the principle that an optical signal has a well-defined polarization, whereas ASE noise is unpolarized as it is essentially white noise. Thus, polarization techniques can be employed to separate the signal and the noise.

(A) Polarization Extinction Method

In polarization extinction method [32], a polarization controller (PC) is used together with a polarizer in front of a tunable optical filter and an optical power meter (Fig. 2.4). The PC is adjusted until the power meter indicates the minimum power, which corresponds to half of the ASE power. Then the polarization controller is set to the orthogonal state and the power meter indicates the maximum power, which corresponds to the signal power plus half of the ASE power. With the maximum and the minimum power, OSNR can be calculated by

$$OSNR(\text{dB}/0.1\text{nm}) = \frac{P_{\max} - P_{\min}}{2P_{\min}} \quad (2.1)$$

where the NEB of the filter is assumed to be 0.1 nm. This method is

simple and has no high-speed electronics processing, but it is susceptible to PMD degradation.

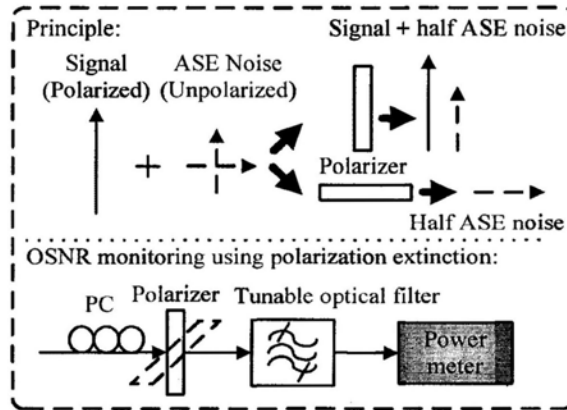


Fig. 2.4. Principle of OSNR monitoring using polarization extinction

(B) Polarization Nulling Method

Polarization-nulling is based upon the same principle as the polarization extinction method except that a rotating quarter-wave plate and a rotating linear polarizer are used to continuously search for the maximum power and the minimum power [33]. This method is simple, has large dynamic range, requires relatively low monitoring power, and has on-the-fly processing. However, it is also susceptible to PMD degradation.

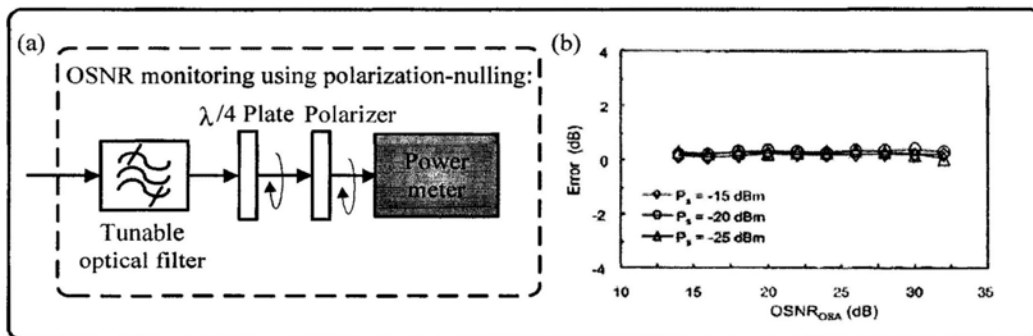


Fig. 2.5. (a) OSNR monitoring module using polarization nulling (b) Monitoring results in a back-to-back configuration for six NRZ channels with errors < 0.4dB (Adapted from Ref. [33])

(C) Degree-of-Polarization (DOP) Based OSNR Monitoring

Another slight variation to polarization-nulling is to use the degree-of-polarization (DOP) [34]. DOP is an important property of light sources used to describe how much of the total light power is polarized. Mathematically, it is defined as the polarized light power divided by the total light power, i.e. the signal power divided by the sum of signal and ASE noise power.

$$DOP = \frac{P_{\text{polarized}}}{P_{\text{total}}} = \frac{P_{\text{polarized}}}{P_{\text{polarized}} + P_{\text{unpolarized}}} = \frac{P_{\text{sig}}}{P_{\text{sig}} + P_{\text{ase}}} \quad (2.2)$$

Thus the in-band OSNR can be estimated from the DOP of a channel as follows:

$$OSNR = 10 \log\left(\frac{DOP}{1 - DOP}\right) \quad (2.3)$$

The advantage of using DOP for in-band OSNR monitoring is that the information obtained can be used to monitor PMD as well. However, the monitoring dynamic range is small and DOP is significantly affected by PMD as well.

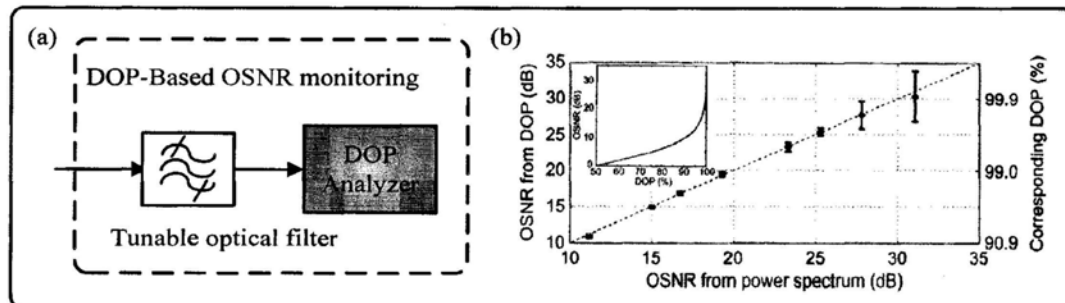


Fig. 2.6. (a) DOP-based OSNR monitoring module (b) Monitoring errors in a back-to-back configuration with errors <1 dB up to 25dB/0.1nm

(Adapted from Ref. [34])

(D) Impact of PMD and partially polarized noise on polarization assisted OSNR monitoring schemes

The above polarization assisted OSNR monitoring schemes are based on the assumption that (1) an optical signal has a well-defined polarization, whereas (2) ASE noise is unpolarized as it is essentially white noise. However, these assumptions may not be valid under the influence of PMD and partially polarized noise.

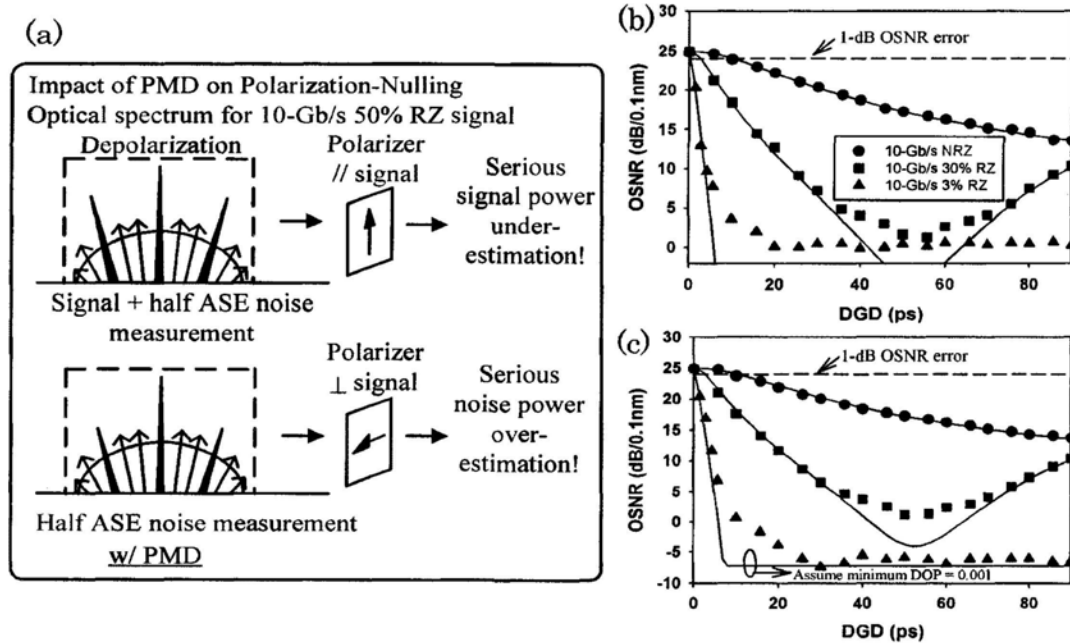


Fig. 2.7. (a) Impact of PMD on Polarization-Nulling; OSNR for (b) polarization-nulling and (c) DOP-based OSNR monitoring under different DGD values (Adapted from Ref. [37])

To a first-order approximation, PMD can be described as a DGD between the two orthogonal polarization modes of the fiber. The DGD of the fiber link will rotate the frequency components of the signal with respect to the carrier by an amount of $\pi \Delta f \times DGD$ (in Jones space), where Δf is the frequency offset from the center carrier, when the signals are launched at 45° with respect to the PSPs [35]. This is referred as the SOP

walk-off effect. Consequently, in polarization-nulling when we align a polarizer parallel to the signal, the maximum power (signal + $\frac{1}{2}$ ASE noise power) will be underestimated because the polarizer is aligned with a single SOP only. Similarly, when we align a polarizer perpendicular to the signal, the minimum power ($\frac{1}{2}$ ASE noise power) will be overestimated. This is illustrated in Fig. 2.7(a). The performance of DOP-based OSNR monitoring is similar to that of polarization-nulling technique. Fig. 2.7(b,c) shows the experimentally measured OSNR monitoring results under different DGD values. For a 1-dB OSNR monitoring error, the maximum tolerable DGD values for NRZ, 30% RZ, and 3% RZ are found to be <10 ps, <3 ps, and 0.5 ps, respectively [36].

There have been some schemes ([37]-[40]) proposed to improve the performance of polarization-nulling technique under PMD. However, they have either complex configuration or tight filter bandwidth requirement. Also, they cannot deal with polarized noise.

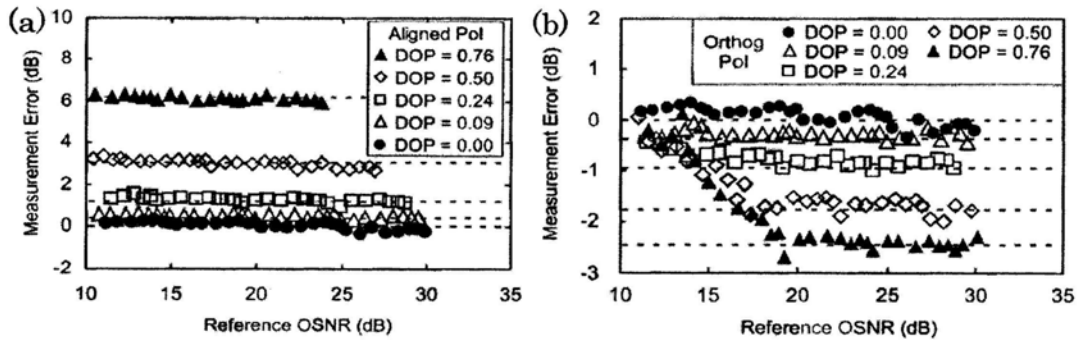


Fig. 2.8. OSNR measurement error by induced by ASE polarization, with ASE polarization state (a) aligned, and (b) orthogonal to signal polarization (Adapted from Ref. [43])

A different challenge to OSNR measurement by polarization assisted approaches is the partial polarization of the ASE noise by polarization

hole-burning (PHB) in the optical amplifiers and by polarization-dependent loss (PDL) in network elements [41]-[42]. Since the total ASE power is estimated as twice its component orthogonal to the signal polarization, when the ASE has a non-zero DOP, the total ASE power is underestimated if the ASE is aligned with the signal, while it is over-estimated if the ASE is orthogonal to the signal. Fig. 2.8 shows the measurement error under different ASE DOP [43]. The monitoring error can be as large as 6 dB when ASE DOP is set to be 0.76.

2.2.2.3 Interferometric Approaches

The third approach to differentiate the signal and the noise is to use an interferometer [44]-[47]. Based on the property that an optical signal is coherent, whereas ASE noise is incoherent, interferometric techniques can be employed to separate the signal and the noise because the signal can interfere at the output of the interferometer while the ASE noise cannot. The method is simple, potentially low-cost, and relatively insensitive to chromatic dispersion and PMD.

In [44], a 1-bit delay-interferometer (DI) is employed to monitor OSNR as shown in Fig. 2.9. In the case of finite extinction ratio (ER) and equal probabilities of “1s” and “0s”, the maximum and the minimum output powers are

$$\begin{aligned} P_{\max} &= \frac{1}{2}P_N + \frac{3}{4}P_S + \frac{1}{2}P_S\sqrt{\frac{1}{ER} - \frac{1}{ER^2}} \\ P_{\min} &= \frac{1}{2}P_N + \frac{1}{4}P_S - \frac{1}{2}P_S\sqrt{\frac{1}{ER} - \frac{1}{ER^2}} \end{aligned} \quad (2.4)$$

where P_N and P_S are the powers of the in-band noise and the signal, respectively. The OSNR of the signal can then be expressed as

$$OSNR(\text{dB}/0.1\text{nm}) = \frac{NEB}{0.1\text{nm}} \left[\frac{1 + 2\sqrt{\frac{1}{ER} - \frac{1}{ER^2}}}{r-1} - \frac{1 - 2\sqrt{\frac{1}{ER} - \frac{1}{ER^2}}}{2} \right]^{-1} \quad (2.5)$$

where $r = P_{\max}/P_{\min}$ and NEB is the noise equivalent bandwidth that is determined by the optical filtering prior to detection. This scheme was found to be insensitive to both chromatic dispersion and PMD.

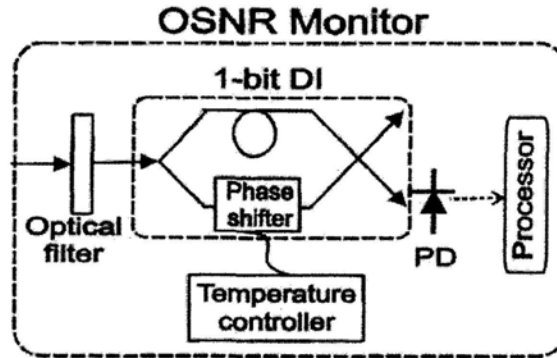


Fig. 2.9. OSNR monitor based on a 1-bit delay interferometer (Adapted from Ref. [44])

There are some variations of the scheme with similar performance which include the use of other kinds of interferometer such as $\frac{1}{4}$ -bit delayed interferometer [45] and birefringent fiber loop [46].

2.3 OSNR Monitoring using Phase-Embedded Fiber Loop Mirror (PM-FLM)

In this section, we propose and experimentally demonstrate a novel in-band optical OSNR monitoring technique using a phase modulator embedded fiber loop mirror (PM-FLM). This technique measures the in-band OSNR accurately by observing the output power of a fiber loop mirror filter, where the transmittance is adjusted by an embedded phase modulator driven by a low-frequency periodic signal. The measurement

errors are less than 0.5 dB for OSNR between 0 and 40 dB in a 10 Gbit/s non-return-to-zero system. This technique was also shown experimentally to have high robustness against various system impairments such as chromatic dispersion, PMD and partially polarized noise, showing high feasibility to be deployed in practical implementation.

2.3.1 Principle of Proposed Technique

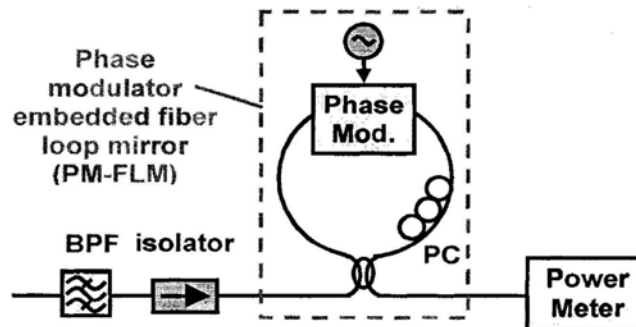


Fig. 2.10. Schematic diagram of the proposed OSNR monitoring module.

PC: polarization controller, BPF: optical bandpass filter

The idea of our proposed scheme is to estimate the incoherent noise from the input signal by periodically shifting the transfer function of a fiber loop mirror filter using an embedded phase modulator. Fig. 2.10 shows the schematic diagram of our proposed OSNR monitoring module. Our proposed OSNR monitoring module consists of a fiber loop mirror embedded with a low-frequency sinusoidal signal driven optical phase modulator (i.e. PM-FLM) and an optical power meter at the output port. The optical phase modulator is pigtailed with polarization-maintaining fibers (PMF) at both input and output ends.

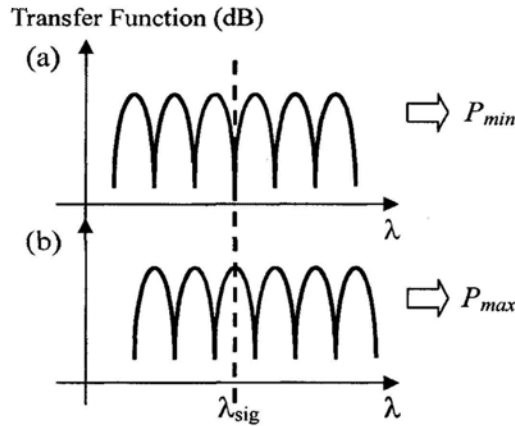


Fig. 2.11. Illustrated PM-FLM transfer function when (a) destructive and (b) constructive interference for data signal occurs

The polarization controller inside the loop is set to produce a polarization rotation of $\pi/2$ for signals passing through both directions. As there is intrinsic birefringence inside the loop induced by the embedded phase modulator and its pigtail, polarization independent periodic transmission and reflection bands in the output spectrum can be realized [48]. By periodically altering the applied voltage to the embedded phase modulator, the phase difference between the counter-propagating signals passing through different principal axes of the phase modulator would change accordingly, and thus leads to periodic shift in the transfer function [49], as illustrated in Fig. 2.11. When the induced phase difference is 0 or π , the signal would experience constructive interference and destructive interference, respectively. Consequently, the input signal can be switched out or reflected back periodically. On the other hand, there are always noises leaking out as long as the noise equivalent bandwidth (NEB) is large enough. As a result, the signal power can be extracted in the case of constructive interference while the noise level can be extracted in the case of destructive interference for the data signal. The choice of the free spectral range (FSR) of the fiber loop mirror is critical to

ensure good measurement performance. If the FSR is too narrow compared with the signal bandwidth, the signal would not be effectively nulled. On the other hand, if FSR is too wide as compared with the BPF bandwidth, there would not be enough noise to leak out in the case of destructive interference.

Under normal operation, the polarization controller (PC) inside the fiber loop was first adjusted to optimize the polarization of the counter propagating signals through the optical phase modulator. Once this step is completed, no further polarization control is needed inside the fiber loop. The input signal is fed into the fiber loop mirror and is split into clockwise (CW) and counter-clockwise (CCW) paths. A low frequency sinusoidal signal is used to drive the optical phase modulator to scan through different amount of phase differences between the counter-propagating signals and an optical power meter is used to track the maximum and the minimum output powers (P_{\max} and P_{\min}). The output of the PM-FLM can be expressed as [47]:

$$P_{arbitrary,out} = (1 - D_{arbitrary} \cos(\Delta\phi_{arbitrary})) \cdot \alpha \cdot P_{arbitrary,in} \quad (2.6)$$

where $\Delta\phi_{arbitrary}$ stands for the phase difference between the CW and the CCW paths, α is the insertion loss and $D_{arbitrary}$ is the distinctness of interference. Since $P_{arbitrary,out,max} = (1 + D_{arbitrary}) \cdot \alpha \cdot P_{arbitrary,in}$ and $P_{arbitrary,out,min} = (1 - D_{arbitrary}) \cdot \alpha \cdot P_{arbitrary,in}$, we obtain:

$$D_{arbitrary} = \frac{P_{arbitrary,out,max} - P_{arbitrary,out,min}}{P_{arbitrary,out,max} + P_{arbitrary,out,min}} \quad (2.7)$$

For the ASE noise, we have

$$P_{ASE,out} = (1 - D_{ASE} \cos(\Delta\phi_{ASE})) \cdot \alpha \cdot P_{ASE,in} \quad (2.8)$$

and the data signal, we have

$$P_{sig,out} = (1 - D_{sig} \cos(\Delta\phi_{sig})) \cdot \alpha \cdot P_{sig,in} \quad (2.9)$$

Since $D_{ASE} \approx 0$, the total output power of the PM-FLM is

$$\begin{aligned}
 P_{out} &= P_{sig,out} + P_{ASE,out} \\
 &= (1 - D_{sig} \cos(\Delta\phi_{sig})) \cdot \alpha \cdot P_{sig,in} + (1 - D_{ASE} \cos(\Delta\phi_{ASE})) \cdot \alpha \cdot P_{ASE,in} \\
 &= (1 - D_{sig} \cos(\Delta\phi_{sig})) \cdot \alpha \cdot P_{sig,in} + \alpha \cdot P_{ASE,in} \\
 &= (1 - D_{sig} \cos(\Delta\phi_{sig})) \cdot \alpha \cdot P_{sig,in} + \frac{P_{ASE,in}}{P_{sig,in}} \cdot \alpha \cdot P_{sig,in} \\
 P_{out} &= \left(1 + \frac{P_{ASE,in}}{P_{sig,in}} - D_{sig} \cos(\Delta\phi_{sig})\right) \cdot \alpha \cdot P_{sig,in} \tag{2.10}
 \end{aligned}$$

Therefore the maximum and minimum output powers are

$$P_{out,max} = \left(1 + \frac{P_{ASE,in}}{P_{sig,in}} + D_{sig}\right) \cdot \alpha \cdot P_{sig,in} \tag{2.11}$$

$$P_{out,min} = \left(1 + \frac{P_{ASE,in}}{P_{sig,in}} - D_{sig}\right) \cdot \alpha \cdot P_{sig,in} \tag{2.12}$$

Dividing (2.11) by (2.12), we obtain

$$\frac{P_{out,max}}{P_{out,min}} = \frac{1 + \frac{P_{ASE,in}}{P_{sig,in}} + D_{sig}}{1 + \frac{P_{ASE,in}}{P_{sig,in}} - D_{sig}} \tag{2.13}$$

and by some manipulation,

$$\begin{aligned}
 \frac{P_{out,max}}{P_{out,min}} (1 - D_{sig}) + \frac{P_{out,max}}{P_{out,min}} \frac{P_{ASE,in}}{P_{sig,in}} &= 1 + D_{sig} + \frac{P_{ASE,in}}{P_{sig,in}} \\
 \frac{P_{out,max}}{P_{out,min}} (1 - D_{sig}) - (1 + D_{sig}) &= \frac{P_{ASE,in}}{P_{sig,in}} \left(1 - \frac{P_{out,max}}{P_{out,min}}\right) \\
 \frac{P_{ASE,in}}{P_{sig,in}} &= \frac{\frac{P_{out,max}}{P_{out,min}} (1 - D_{sig}) - (1 + D_{sig})}{1 - \frac{P_{out,max}}{P_{out,min}}} \tag{2.14}
 \end{aligned}$$

If the phase difference between the CW and the CCW paths changes by more than 2π , the OSNR can be derived as:

$$OSNR(dB/0.1nm) = \frac{P_{sig,in} \cdot NEB_f}{P_{ASE,in} \cdot 0.1nm} = \frac{(1-r) \cdot NEB_f}{[r(1-D_{sig}) - (1+D_{sig})] \cdot 0.1nm} \tag{2.15}$$

where $r = P_{out,max}/P_{out,min}$, NEB_f is the noise equivalent bandwidth of the band-pass filter (BPF) at the module's input, and $D_{sig} = (P_{sig,max} - P_{sig,min}) / (P_{sig,max} + P_{sig,min})$ is the distinctness of signal interference when noise is absent. Note that the component losses can be ignored as both signal and noise experience almost exactly the same amount of component loss.

2.3.2 Experimental Results and Discussion

The proposed OSNR monitoring scheme was experimentally characterized in a 10-Gb/s NRZ on-off keying (OOK) system, as shown in Fig. 2.12. The signal source was a DFB laser at 1545.6 nm, externally modulated by a LiNbO₃ optical intensity modulator with 10-Gb/s 2³¹-1 PRBS NRZ data. An EDFA was used to produce different levels of ASE noise, which was then combined with the modulated signal by a 3-dB fiber coupler. The OSNR level was controlled by the optical attenuators before the fiber coupler and it was adjusted from 0 dB to 40 dB in our experiment. The noise-added signal was then amplified by another EDFA and a PMD emulator was inserted to simulate the effects of different differential group delay (DGD) values varying from 0 ps to 50 ps. Finally, the composite signal was fed to an optical spectrum analyzer (OSA) and also to our proposed OSNR monitoring module, for comparison.

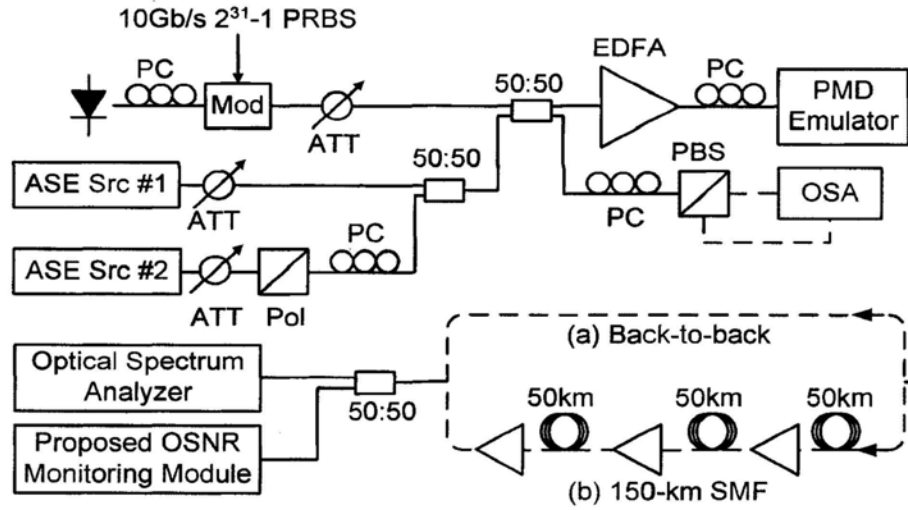


Fig. 2.12. Experimental setup. PC: polarization controller, ATT: optical attenuator, OSA: optical spectrum analyzer, EDFA: erbium doped fiber amplifier

The BPF bandwidth was about 1 nm, which was wide enough to cover the whole signal spectrum. The implementation of the BPF may be static or tunable to implement a static or shared OSNR monitor respectively. The length of the fiber loop was only around 2 meters, therefore immune to environmental fluctuation. The polarization dependence of the periodic filtering characteristics was shown to be negligible by randomly changing the input signal polarization using a polarization controller. The sampling time of the optical power meter was set to be 20 ms, which was fast enough compared with the speed of variation in the output power, and was slow enough to eliminate the interference dependence on the signal pattern. The driving frequency of the phase modulator was set to be 1 Hz and the driving amplitude was set to be little bit larger than V_π of the phase modulator to ensure that the whole range of output power can be covered. The total measurement time for our scheme was within 30 seconds. The free spectral range (FSR) of the PM-FLM transfer function was measured to be around 0.7 nm. D_{sig} and D_{ASE} were measured to be

about 0.975 and 0.01, respectively, in our experiment.

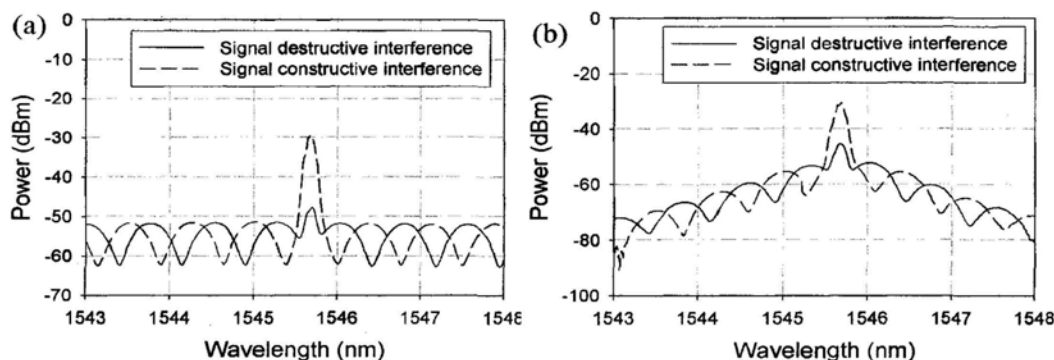


Fig. 2.13. Output optical spectra (a) without, and (b) with optical bandpass filter at the monitoring module input

The output optical spectral of the PM-FLM are shown in Fig. 2.13. It shows that the data signal and the ASE noise can be effectively separated by dithering the driving signal of the phase modulator.

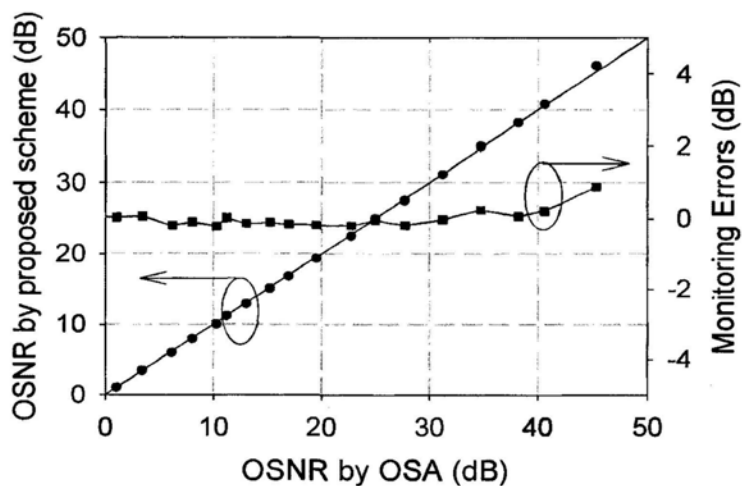


Fig. 2.14. Measured OSNR and monitoring errors

Fig. 2.14 compares various levels of monitored OSNRs by our proposed scheme with the conventional OSNR measurements by linear interpolation. The OSNRs agreed very well with the reference OSNRs.

The measured monitoring error was less than 0.5 dB for OSNR varying from about 0 dB/0.1 nm to 40 dB/0.1 nm. This shows high sensitivity and large input dynamic range of the proposed scheme.

Next, the performance of our scheme after 150-km single mode fiber (SMF) transmission was investigated. An EDFA was added after each 50-km SMF span and the output power from each EDFA was maintained at 1 and 10 dBm, respectively. Fig. 2.15 shows that the monitoring errors were negligible, indicating that our scheme was rather insensitive to chromatic dispersion, typical value of PMD (< 1.5 ps in our case), and power in long-haul transmission in SMF.

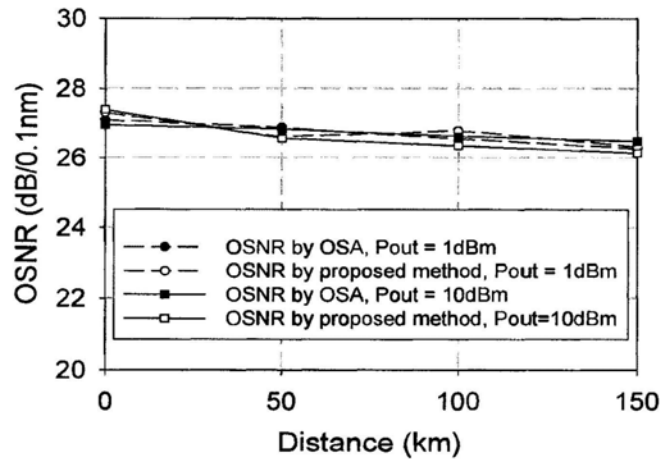


Fig. 2.15. OSNR monitoring results in a 150-km SMF link (PMD < 1.5 ps, $P_{out}=1$ and 10dBm respectively)

Fig. 2.16 shows the monitoring errors when DGD was introduced. For reference, the OSNR was set to be 25 dB/0.1 nm by the OSA. The monitoring error was smaller than 0.25 dB for DGD varying from 0 ps to 50 ps, which shows high PMD insensitivity of our proposed scheme.

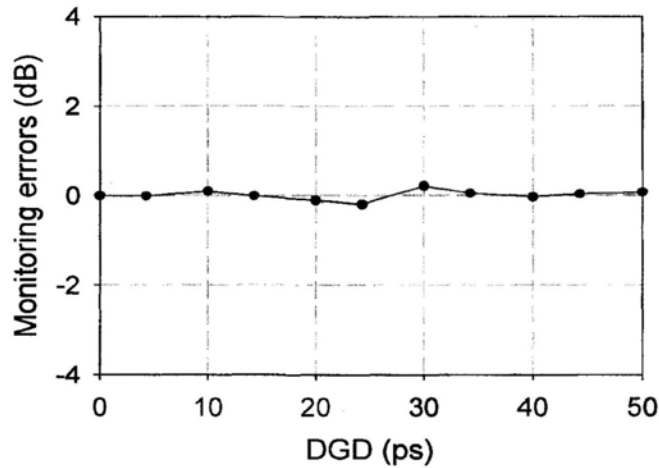


Fig. 2.16. Monitoring errors under different DGDs for 25-dB OSNR

The influence of partially polarized ASE to our scheme was also investigated. Partially polarized ASE was generated by combining the output of a polarized ASE source with the output of an unpolarized ASE source using a 3-dB coupler. Two independent attenuators were used to control the DOP of the resulting ASE. The DOP of the unpolarized ASE source was measured to be 5.16%, while the polarized source had a DOP of 99.69%. A polarization controller was used to set the polarization of the ASE either aligned with or orthogonal to the signal polarization. The polarization alignment of the signal and noise components was determined using a polarization beam splitter (PBS) and an optical spectrum analyzer (OSA) as shown in Fig. 2.12. The signal was nulled in one branch of the PBS, while the polarized part of the ASE was nulled either in the same branch or the orthogonal branch to obtain the desired state of polarization. Fig. 2.17 shows that the monitoring errors were negligible for different values of noise DOP, showing that our proposed scheme is insensitive to partially polarized ASE noise. For instance, Fig. 2.18 shows the OSNR measurement performance under the worst case (polarized ASE). The monitoring errors were kept to be less than 0.5 dB over the whole 40-dB monitoring range. This further confirms the

robustness of our proposed OSNR monitoring scheme against partially polarized ASE. Compared with the polarization nulling method which could induce non-negligible monitoring error under partially polarized ASE [43], our scheme shows a higher robustness to operate in practical environment.

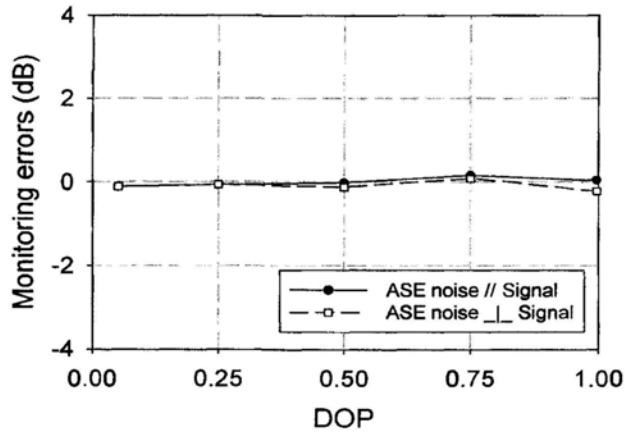


Fig. 2.17. Monitoring errors for partially polarized ASE with different DOPs and alignment (dark for parallel, white for orthogonal) to signal for 25-dB OSNR)

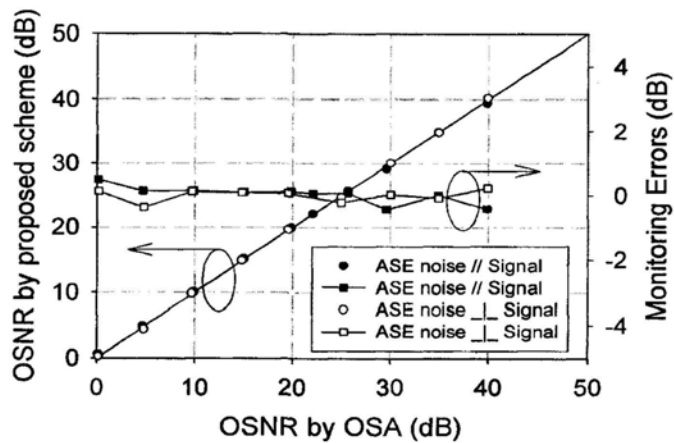


Fig. 2.18. Measured OSNR (circles) and monitoring errors (squares) for polarized ASE (DOP=99.69%) which is parallel (dark) or orthogonal (white) to signal

Finally, the data rate dependency of our proposed scheme was investigated. The OSNR monitoring errors (for 25-dB OSNR) for bit-rates from 2.5 Gbps to 10 Gbps were shown in Fig. 2.19, and the OSNR monitoring performance for 2.5-Gbps data rate was particularly shown in Fig. 2.20. These two figures show that our proposed scheme is bit-rate independent in the range from 2.5 Gbps to 10 Gbps, which is a desirable feature in OSNR monitoring.

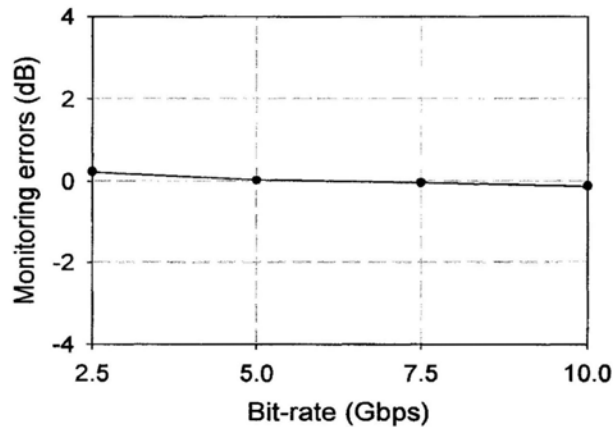


Fig. 2.19. Monitoring errors under different bit-rates for 25-dB OSNR

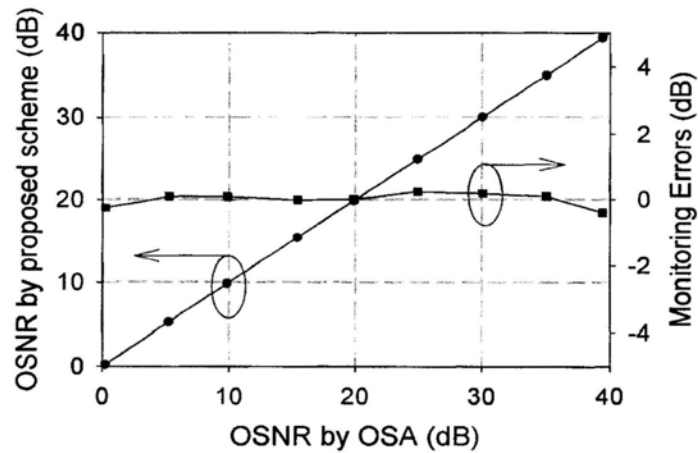


Fig. 2.20. Measured OSNR and monitoring errors for 2.5-Gbps data rate

2.4 Summary

In this chapter, we have proposed a novel and simple in-band OSNR monitoring technique using phase modulator embedded fiber loop mirror (PM-FLM). Various characterization experiments have shown that the proposed technique has high accuracy, high sensitivity and large dynamic range in OSNR measurements. For instance, the monitoring errors were less than 0.5 dB for OSNR between 0 to 40 dB in a 10-Gb/s NRZ system. This technique has also been shown to be PMD insensitive, CD insensitive, bit-rate independent, and robust to partially polarized ASE noise.

Chapter 3 Chromatic Dispersion (CD) Monitoring

3.1 Management of Fiber Chromatic Dispersion

Chromatic dispersion (CD) is a well-understood effect that arises from the frequency-dependent nature of the index of refraction in an optical fiber. It is one of the main impairments that limit the performance of optical fiber systems. Since light of different frequencies travel at different speeds inside optical fiber due to chromatic dispersion, pulse spreading and intersymbol interference (ISI) would occur and lead to BER floors. For instance, while dispersion limits a 2.5-Gbit/s channel to roughly 900 km (1-dB power penalty), a 10- and 40-Gbit/s channel would be limited to approximately 60 km and 4 km, respectively. Thus, some method of dispersion compensation must be employed for a system to operate beyond these distance limits.

Over the course of the 1980s, fiber manufacturers started to fabricate dispersion-shifted fiber (DSF) whose zero dispersion wavelength point coincided with the loss minimum of the fiber with the aim of reducing the two main limitations imposed by the fiber itself. However, such fiber is incompatible with the deployment of wavelength division multiplexing (WDM) systems since harmful nonlinear effects would be generated. Any nonlinear mixing effects such as self-phase modulation (SPM), cross-phase modulation (XPM), and four-wave mixing (FWM) that require phase matching between the different wavelength channels will accumulate at a higher rate than if the channels travel at widely different speeds.

Chromatic dispersion is in fact a necessary evil which should be managed rather than eliminated. A simple yet elegant solution is to create a dispersion map, in which the designer of a transmission link alternates elements that produce positive and then negative dispersion such that the dispersion has some nonzero value at each point along the fiber. This effectively eliminates FWM and XPM, but the total accumulated dispersion at the end of the fiber links is zero, thus minimal pulse broadening is induced. Introducing negative dispersion along a link having positive dispersion can be referred to as either dispersion compensation or dispersion management. Traditionally, the introduction of chromatic dispersion compensation modules has been based on dispersion-compensating fiber (DCF) [50]. Other more recent devices include high-order mode (HOM) DCF, chirped fiber Bragg gratings (FBG), virtually imaged phase arrays (VIPAs) and electronic compensation circuitry. Table 3.1 summarizes the popular commercially available compensation techniques [51].

Table 3.1. Overview of commercially available dispersion compensation devices (Adapted from Ref. [51])

| <i>Technology</i> | <i>Loss</i> | <i>Tunability</i> | <i>Bandwidth</i> | <i>Non-linearity</i> | <i>Slope Matching</i> |
|-------------------|-------------|-------------------|------------------|----------------------|-----------------------|
| DCF | High | None | Broadband | High | Possible |
| Chirped FBG | | | | | |
| Broadband | Low | Very slight | Broadband | Low | Easy |
| Sampled | Very low | Possible | Channels | | |
| VIPA | High | Possible, \pm | Channels | Very low | Easy |
| HOM fiber | Medium | Very slight | Broadband | Medium | Easy |

Chromatic dispersion has been considered predominantly a time-invariant phenomenon. Therefore, in today's networks, fibers and other dispersive components are pre-characterized for chromatic dispersion and the transmission link engineered to accommodate or correct this value in a "set-and-forget" manner using fixed compensation

solutions. However, there are several important aspects of optical systems and networks that make tunable dispersion compensation solutions attractive, including [51]:

(1) *Inventory management.* Even in a static network, distances between dispersion compensation points will vary. Dispersion compensation modules must cover a wide range of compensation values. Therefore tunable compensation module significantly reduces the inventory of different required types of compensation modules.

(2) *Accuracy for ≥ 40 -Gbit/s systems.* The required accuracy in dispersion compensation increases dramatically with the signal bit rate. While the amount of residual dispersion that is tolerable at 10-Gbit/s is approximately 1000 ps/nm, this margin shrinks to only 60 ps/nm for 40-Gbit/s systems as shown in Fig. 3.1(a). The use of tunable modules seems to be the only practically solution for compensating accumulated dispersion.

(3) *Changes in the path length.* In a reconfigurable network, signal paths are set up and torn down in seconds or fractions of seconds. Channels are added and dropped, and wavelengths may follow time-dependent paths, all to achieve higher efficiency of the network's resources. As fiber paths change, chromatic dispersion will change accordingly, and compensation devices will have to adjust on the fly to accommodate the changes.

(4) *Environmental effects.* Temperature changes can lead to variations in dispersion that may be significant enough to impact the system. Fig. 3.1 shows that a not-uncommon 20°C variation along a 1000-km 40-Gbit/s link would produce significant degradation. Therefore tunable dispersion compensation is necessary to adapt to environmental changes.

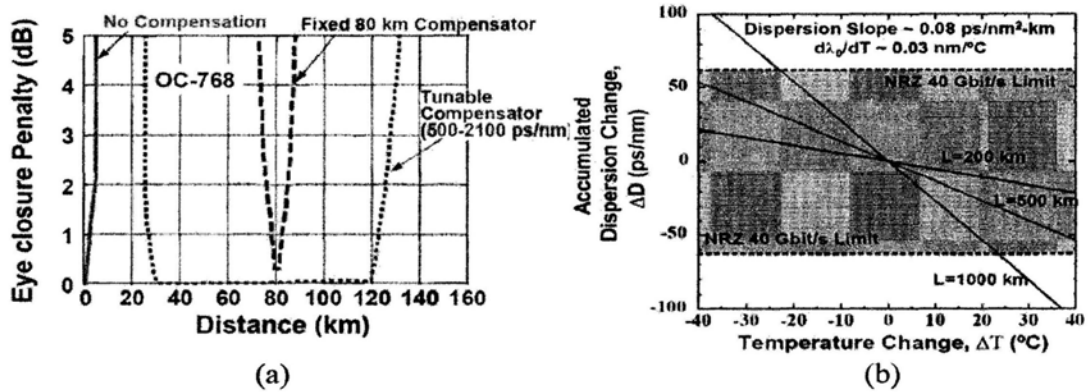


Fig. 3.1. (a) Dispersion tolerance range using fixed and tunable compensator (b) change in the accumulated dispersion as a function of the temperature fluctuations and fiber length (Adapted from Ref. [51])

In order to achieve both tenability and adaptability in dispersion compensation, a feedback loop is required to track the changes in the accumulated dispersion of a signal and drive a tuning element that would compensate the dispersion. A key element of a dynamic dispersion compensator is a chromatic dispersion monitor in the feedback loop that can measure the required compensation, while the data is being transmitted through the optical link. This is quite different from the more traditional chromatic dispersion measurement techniques in which dark fiber is usually measured off-line. In the following section, we will review previously proposed CD monitoring schemes and introduce our proposed CD monitoring scheme based on birefringent fiber loop (BFL).

3.2 Previously Proposed Schemes for CD Monitoring

Several techniques have been demonstrated for real-time chromatic dispersion monitoring to enable dynamic dispersion compensation. Most of them make use of CD induced fading effect of signal sideband. Chromatic dispersion induces a time delay between the sidebands corresponding to a

certain frequency component. As the phase difference corresponding to this time delay increases, the sidebands become out of phase, when the side bands start canceling each other and the amplitude of the RF components becomes very small. Thus, the change of signal sideband power can provide dispersion information.

3.2.1 Sub-carrier Ratio Method

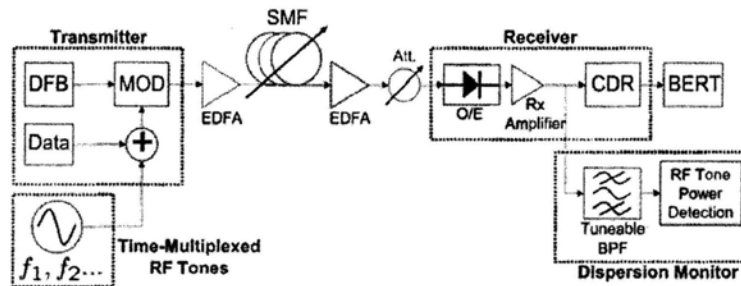


Fig. 3.2. Sub-carrier based CD monitoring (Adapted from Ref. [2])

Fig. 3.2 shows a CD monitoring technique using sub-carrier ratio method [2]. At the transmitter side, RF sub-carriers are added to the data to modulate light. Since sub-carrier would experience fading under dispersion, CD can be monitored by measuring the powers of different sub-carriers at the receiver side. Fig. 3.3 shows the fading effect of two different sub-carrier frequencies and their ratio. By measuring the sub-carrier ratio instead of measuring only the RF power of one sub-carrier, both the dynamic range and sensitivity can be improved. This technique is simple and accurate. However, it requires modification at the transmitter side, which may not be always possible. Besides, sub-carrier would degrade the signal.

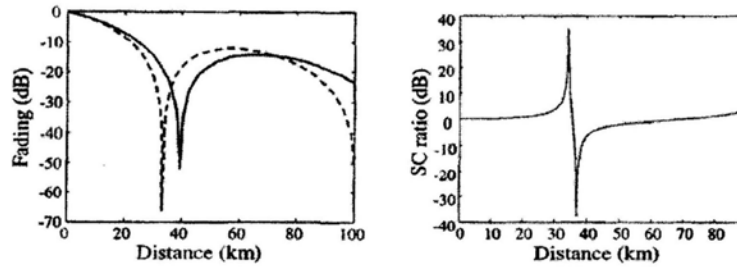


Fig. 3.3. (a) Fading for subcarriers with two different frequencies and (b) the fading ratio of the two subcarriers (Adapted from Ref. [2])

3.2.2 Clock Tone Analysis

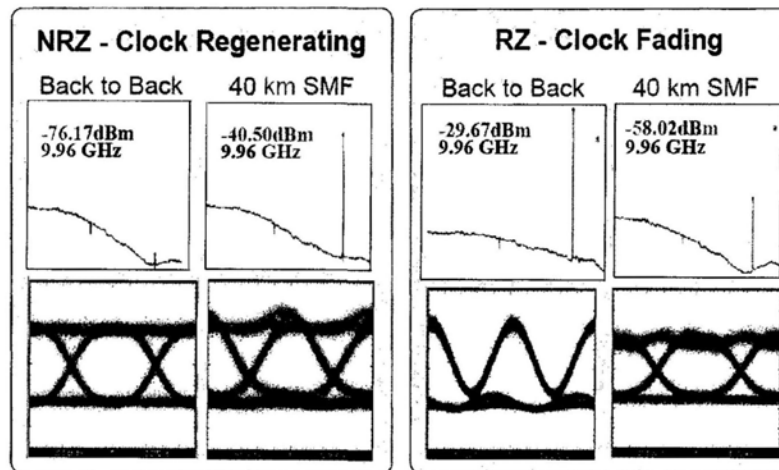


Fig. 3.4. Clock regenerating effect in NRZ systems and clock fading effect in RZ systems under dispersion (Adapted from [52])

Another similar technique to monitor chromatic dispersion is based on a clock regenerating effect in NRZ systems and a clock fading effect in RZ systems under dispersion [52]. There is no clock component at the transmitter output for NRZ systems. However, during the transmission, partial compression would occur due to dispersion. Therefore these reshaped pulses have clock components and the regenerated clock power is proportional to the amount of dispersion. On the other hand, RZ data

contains clock component at the transmitter. However, during the transmission, the pulse is broadened due to dispersion, corresponding to a faded clock component. Dispersion can be monitored by measuring the amount of clock fading. The NRZ clock regenerating effect and RZ clock fading effect are shown in Fig. 3.4. The merit of this technique is that it does not require modification of the transmitter, but is bit rate and modulation format dependent.

3.2.3 Sideband Optical Filtering

Chromatic dispersion can also be monitored by sideband optical filtering [53]. Since the upper sideband and lower sideband of a signal have different frequencies, they travel at different speeds in dispersive medium. Therefore by filtering out the upper and lower sideband of a signal separately and compare their arrival times through clock recovery and phase-sensitive detection, the chromatic dispersion can be measured as shown in Fig. 3.5. This technique is highly sensitive, and it does not require modification at the transmitter.

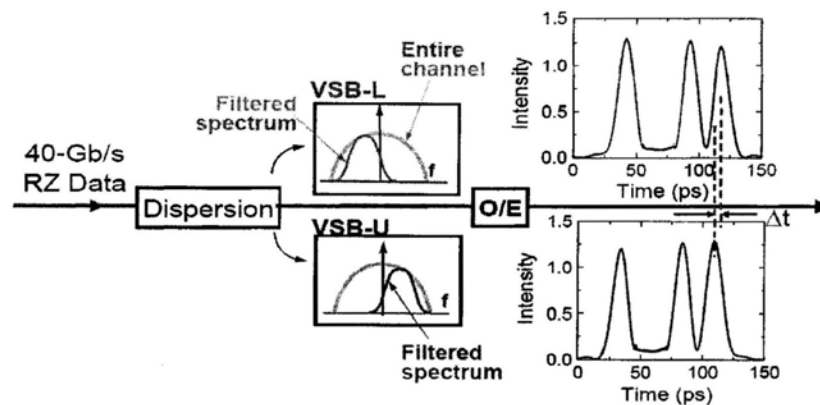


Fig. 3.5. CD monitoring using sideband optical filtering
(Adapted from Ref. [53])

3.3 Chromatic Dispersion Monitoring Using Birefringent Fiber Loop (BFL)

In this section, we propose and demonstrate a new technique for monitoring dispersion using birefringent fiber loop (BFL). By feeding a signal distorted by chromatic dispersion into a fiber loop which consists of a high-birefringence (Hi-Bi) fiber, the amount of dispersion experienced by the signal can be deduced from the measured RF power at a specific selected frequency which is determined by the length of the Hi-Bi Fiber. This technique requires no modification at the transmitter, provides large measurement range and is polarization insensitive and independent of data rate. A measurement range of 1500 ps/nm has been experimentally achieved for 10-Gb/s NRZ signal. Similar performance can be achieved for 40-Gb/s NRZ signal.

3.3.1 Principle of Proposed Technique

When an intensity-modulated double-sideband signal is transmitted along a fiber, fiber dispersion will convert part of the intensity modulation into phase modulation, which induces a phase delay φ_f at frequency f . This can be explained by expanding the power series of the frequency dependent propagation constant $\beta(\omega)$ under the influence of chromatic dispersion [54]. Therefore, the total accumulated dispersion D of the fiber link can be determined by measuring the phase modulation at a specific spectral component. This can be easily accomplished by a birefringent fiber loop (BFL) which only consists of a 3-dB coupler, polarization controller (PC) and a piece of high-birefringence (Hi-Bi) fiber [55], as shown in Fig. 3.6. The advantages of using BFL include simplicity, polarization insensitivity and low insertion loss.

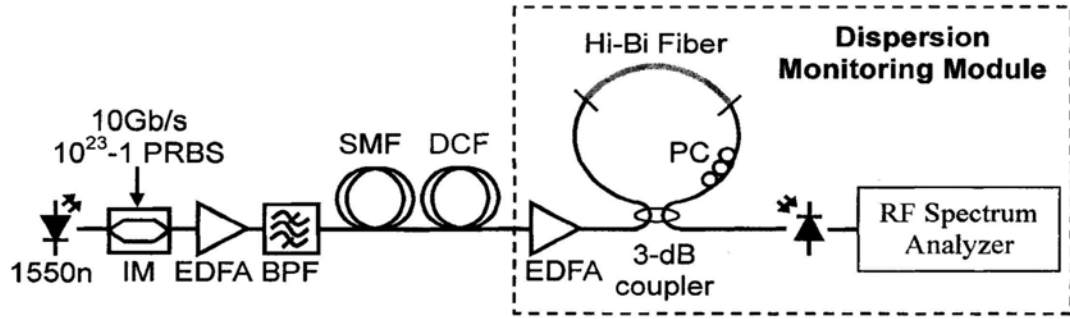


Fig. 3.6. Schematic diagram of the proposed chromatic dispersion monitoring module, with experimental setup for demonstration. IM: intensity modulator, EDFA: erbium-doped fiber amplifier, BPF: optical bandpass filter, SMF: single-mode fiber, DCF: dispersion compensating fiber, PC: polarization controller

The incoming signal is split by the 3-dB coupler into two counter-propagating beams that would recombine and interfere at the coupler after traveling around the fiber loop. The clockwise (CW) and the counter-clockwise (CCW) beams would experience a time delay τ induced by the Hi-Bi fiber under the condition that the PC inside the loop provides a 90° rotation for beams from both directions. The frequency response of the BFL can be written as

$$H(f) = |H(f)|e^{j\Phi(f)} = \frac{j}{2}(e^{-j2\pi f\tau} + 1) \quad (3.1)$$

Fig. 3.7 illustrates the magnitude and the phase responses of the BFL. The free spectral range (FSR) of the BFL is $1/\tau$. Suppose the monitoring position is at f_p , the basic idea is to let the phase shifts between the optical carrier at f_o and the two frequency components at $f_o \pm f_p$ be $+\pi/2$ and $-\pi/2$, respectively, so that these two frequency components have a π phase difference, and therefore, they could cancel each other when there is zero fiber dispersion. In addition, the RF power at f_p should change significantly even when only a small residual dispersion is incurred, so

that a high dispersion resolution can be obtained. From Fig. 3.7, it can be deduced that two conditions should be satisfied: (1) $f_0 = \frac{2n-1}{4\tau}$ where n is an integer (so that the $f_0 - f_p$, f_0 and $f_0 + f_p$ are aligned with three successive quadrature points), and (2) $f_p = \frac{FSR}{2} = \frac{1}{2\tau}$.

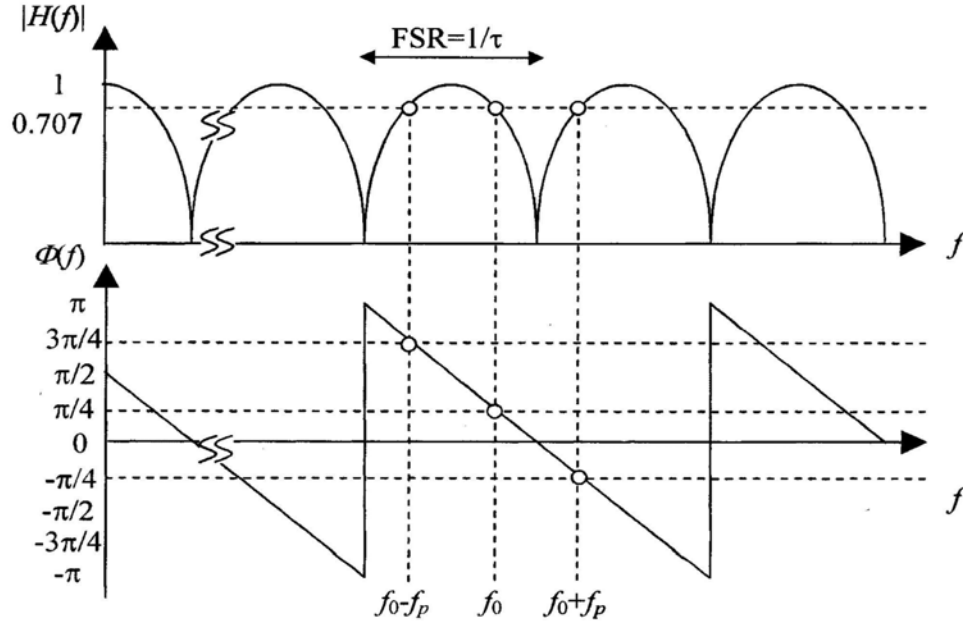


Fig. 3.7. Optical amplitude and phase responses of a BFL at its output.

Considering the carrier $\omega_0 = 2\pi f_0$ and the sidebands $\omega_0 \pm \Omega$ where $\Omega = 2\pi f_p$, as the carrier and sidebands propagate along the fiber, they acquire phase shifts of φ_0 and φ_{\pm} , respectively. This produces an electric field with both intensity and phase modulation components at Ω . If the signal is then sent through an BFL with DGD of τ , the electric field at the output of the BFL will be

$$\begin{aligned}
 E_{out} = & \frac{1}{2}[A_0 \cos(\omega_0 t + \varphi_0) \pm A_0 \cos(\omega_0 t + \varphi_0 + \omega_0 \tau)] \\
 & + \frac{1}{2}[A_\Omega \cos(\omega_0 t + \Omega t + \varphi_+) \pm A_\Omega \cos(\omega_0 t + \Omega t + \varphi_+ + \omega_0 \tau + \Omega \tau)] \\
 & + \frac{1}{2}[A_\Omega \cos(\omega_0 t - \Omega t + \varphi_-) \pm A_\Omega \cos(\omega_0 t - \Omega t + \varphi_- + \omega_0 \tau - \Omega \tau)]
 \end{aligned} \quad (3.2)$$

The detected photocurrent is then proportional to

$$\begin{aligned}
 i_\pm \propto & (1 \pm \cos(\omega_0 \tau)) \cos\left(\frac{\Omega \tau}{2}\right) \cos\left(\frac{\varphi_+ + \varphi_-}{2}\right) \cos(\Omega t + \eta) \\
 & + \sin(\omega_0 \tau) \sin\left(\frac{\Omega \tau}{2}\right) \sin\left(\frac{\varphi_+ + \varphi_-}{2}\right) \sin(\Omega t + \eta)
 \end{aligned} \quad (3.3)$$

where $\eta = (\varphi_+ + \varphi_-)/2$. Since $f_0 = \frac{2n-1}{4\tau}$, we get $\omega_0 \tau = (2n-1)\frac{\pi}{2}$ and the photocurrent is proportional to

$$\begin{aligned}
 i_\pm \propto & \cos\left(\frac{\Omega \tau}{2}\right) \cos\left(\frac{\varphi_+ + \varphi_-}{2}\right) \cos(\Omega t + \eta) \\
 & \pm \sin(\omega_0 \tau) \sin\left(\frac{\Omega \tau}{2}\right) \sin\left(\frac{\varphi_+ + \varphi_-}{2}\right) \sin(\Omega t + \eta)
 \end{aligned} \quad (3.4)$$

Resulting in an RF power at $\Omega = 2\pi f_p = \pi/\tau$ of

$$P \propto \sin^2\left(\frac{\varphi_+ + \varphi_-}{2}\right) = \sin^2\left(\frac{\beta_2}{2}(\Delta\omega)^2\right) = \sin^2\left(\frac{\lambda^2 D}{4\pi c}(2\pi f_p)^2\right) = \sin^2\left(\frac{\pi \lambda^2 f_p^2}{c} D\right) \quad (3.5)$$

where λ is the optical wavelength and c is the speed of light in vacuum. Therefore, by measuring the RF power of the detected signal from the BFL at f_p using an RF spectrum analyzer, the total accumulated dispersion can be determined. With the use of the BFL, the RF power at f_p is now related to a sine function rather than a cosine function [2] of the accumulated dispersion. Therefore the dispersion resolution can be improved significantly, especially around zero dispersion regime.

The monitoring position f_p can be easily adjusted by varying τ which

is controlled by the length of the Hi-Bi fiber. This gives a freedom of control to system administrator for optimizing the measurement range and stability. In general, the measurable D increases with the decrease of f_p which can be easily observed from equation (3.5). However, a long Hi-Bi fiber is needed which may degrade the stability. Note that a bandpass filter together with an RF power meter can be used, in practice, to replace the RF spectrum analyzer. Besides, multiple channels monitoring can be realized if the channel spacing are tuned to be $\Delta\omega = \frac{(2q-1)\pi}{2\tau}$ where q is an integer.

3.3.2 Experimental Results and Discussion

The proposed CD monitoring technique was experimentally demonstrated in a 10-Gb/s NRZ on-off keying (OOK) system, as shown in Fig. 3.6. The signal source was a tunable laser at 1550 nm, which was then externally modulated by a LiNbO₃ optical intensity modulator with 10-Gb/s 2²³-1 PRBS NRZ data. The modulated signal was amplified by an EDFA, before being transmitted through a dispersive fiber link, consisting of different combinations of single-mode fiber (SMF) or dispersion-compensating fiber (DCF) to produce different amount of accumulated dispersion. The signal was then sent to the proposed dispersion monitoring module for CD measurement.

The dispersion monitoring module consisted of an EDFA, a BFL, a 20GHz detector and an RF spectrum analyzer. The EDFA was used to maintain the same optical power before the detector to ensure that the measured power variations were mainly caused by fiber dispersion, rather than a change in the received optical power. The BFL consisted of a 3-dB coupler, a PC, and a segment of Hi-Bi fiber with a birefringence of

5.275×10^{-4} . The Hi-Bi fiber was put in metal box and was temperature stabilized. The relative optical delay between the two axes of the Hi-Bi fiber is about 100 ps (fiber length=56.8m), which was verified by observing the peak spacing in the BFL transmittance, as shown in Fig. 3.8. The received power at 5 GHz ($f_{RF} = 1/2\tau$) was measured using an RF spectrum analyzer with 1-MHz measurement bandwidth. The measured power has <0.1 dB variation for different input signal polarization, which shows that the scheme is polarization insensitive.

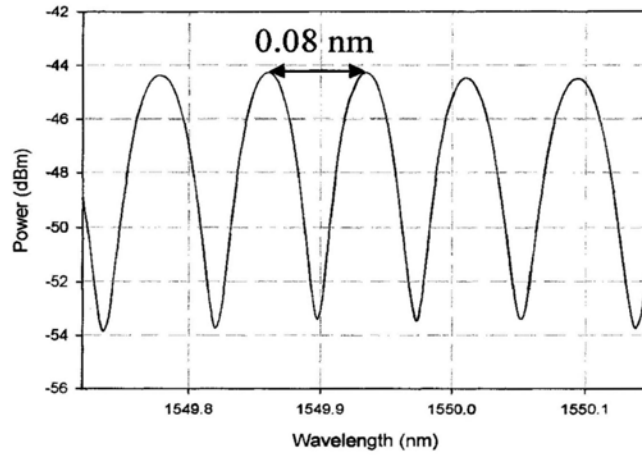


Fig. 3.8. Transmittance of the birefringent fiber loop.

Fig. 3.9 shows the RF spectra for accumulated dispersion of 0 ps/nm, 110 ps/nm, and 450 ps/nm respectively. It can be seen that the received RF power at 5 GHz varies in different cases. Thus, such measured RF power variation can be used to indicate the amount of accumulated dispersion experienced by the signal. Fig. 3.10 shows the measured RF power at 5 GHz for different values of accumulated dispersion. An unambiguous measurement range of 1500 ps/nm was observed using the proposed CD monitoring technique. Note that the measurement range can, in principle, reach $c/(2\lambda^2 f_{RF}^2) = 2497$ ps/nm for $\lambda = 1550$ nm, and it is independent of both

data rate and modulation format [56]. Nevertheless, accumulated dispersion only up to 1500 ps/nm was measured in our experiment due to the lack of equipment such as single mode fiber. Fig. 3.11 shows the chromatic dispersion measurement under different values of DGD with reference dispersion of 340 ps/nm. Stable measurement within 30 ps of DGD was observed which shows that the proposed scheme is rather insensitive to PMD.

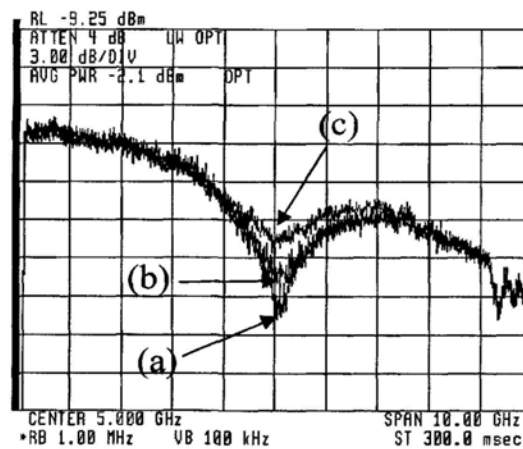


Fig. 3.9. RF spectrum at BFL output for signals with (a) 0 ps/nm, (b) 110 ps/nm and (c) 450 ps/nm accumulated dispersion

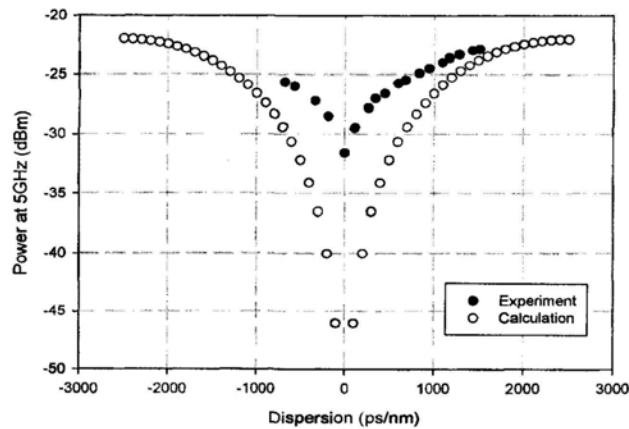


Fig. 3.10. Received RF power at 5GHz as a function of dispersion obtained by experiment (10 Gbit/s NRZ OOK data) and equation 3.5

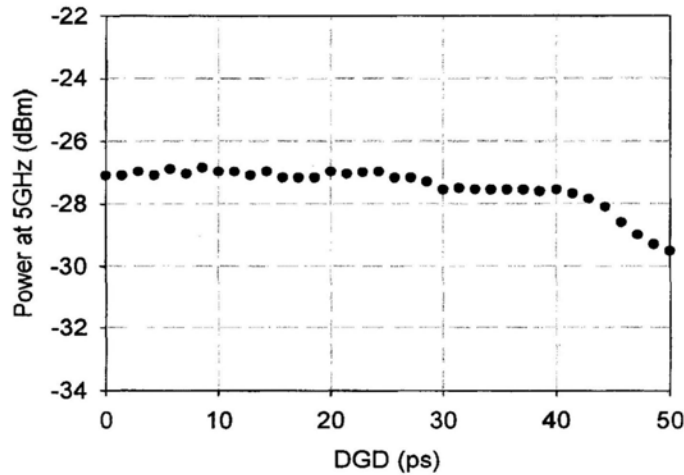


Fig. 3.11. Measured RF power at 5GHz vs DGD with data rate of 10 Gbit/s and accumulated dispersion of 340 ps/nm

Next, we have tried to repeat the experiment for 40 Gbit/s NRZ OOK data. The experimental setup is similar to the one shown in Fig. 3.6 except that a 10-to-40-Gbit/s electrical multiplexer was used to generate 40-Gbit/s NRZ electrical signal to drive a 40-Gbit/s intensity modulator.

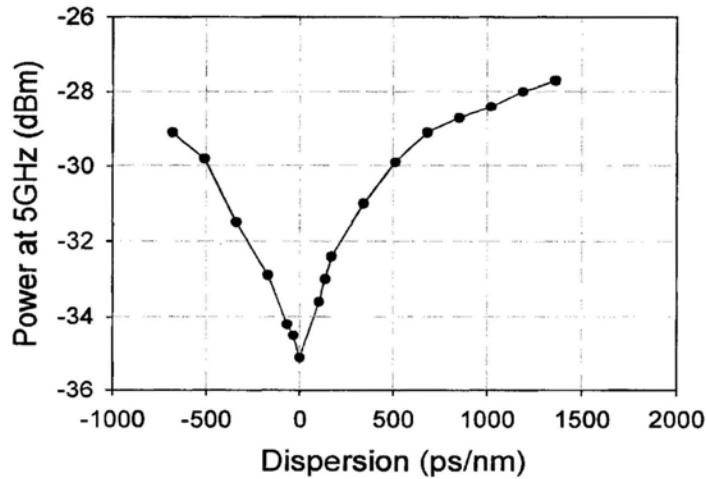


Fig. 3.12. Received RF power at 5GHz as a function of dispersion (40 Gbit/s NRZ OOK data)

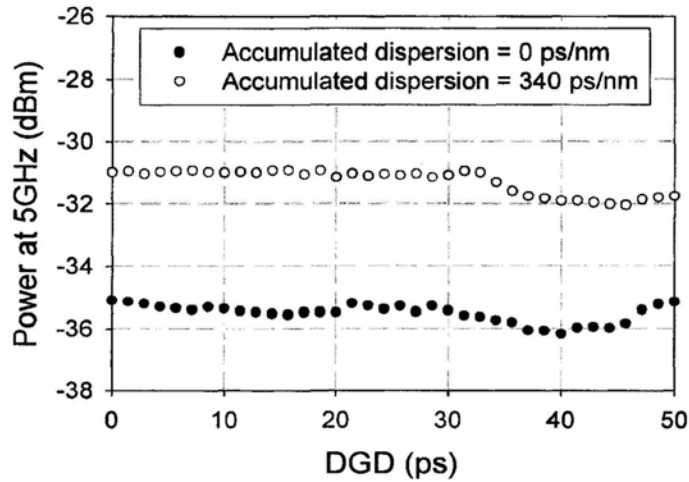


Fig. 3.13. Measured RF power at 5GHz vs DGD with data rate of 40 Gbit/s and accumulated dispersion of 0 ps/nm and 340 ps/nm

The measurement results are depicted in Fig. 3.12 and Fig. 3.13. The results are similar to that of 10-Gbit/s data, showing that the proposed scheme works well under different bit rate.

Although this scheme has a large measurement range, it would be useful to differentiate between positive and negative dispersion. This can be accomplished using the system shown in Fig. 3.14 which is similar to the one described in [57]. The signal is split and transmitted through two sections with dispersive elements having total dispersions of $+D_0$ and $-D_0$. Each arm is then transmitted through a BFL and detected with photodetector. The RF signal from each segment is filtered with RF bandpass filter, amplified, and converted into a voltage signal using an RF power detector. The difference of two voltage signals is then used to determine the sign and magnitude of the total dispersion. If the dispersion in the link is positive, the section with the $+D_0$ dispersive element will produce a larger RF power than the section with the $-D_0$ element, while a

negative dispersion in the link will result in a smaller RF power. The tradeoff here is that the ability to determine the sign of the dispersion reduces the measurable magnitude by a factor of two.

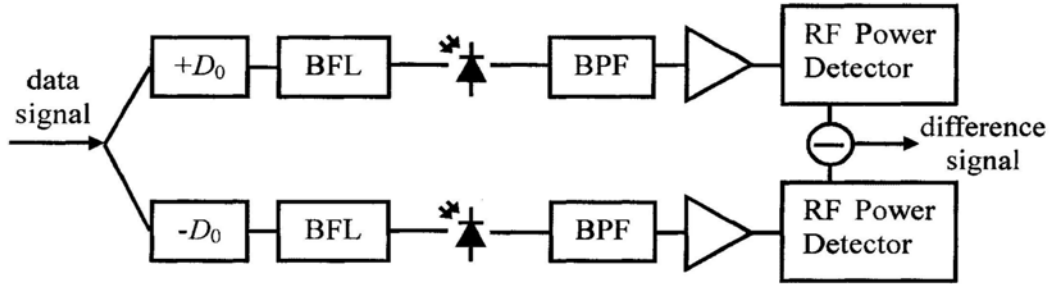


Fig. 3.14. Modified design enabling the measurement of both the magnitude and sign of the link's dispersion

3.4 Summary

In this chapter, a new chromatic dispersion monitoring technique using birefringent fiber loop was proposed and demonstrated. Experimental results showed an unambiguous measurement range of 1500 ps/nm for 10-Gb/s NRZ data. Similar results were obtained for 40-Gb/s NRZ quasi-PRBS data. This technique requires no modification at the transmitter, provides large measurement range and is polarization insensitive and independent of data rate.

Chapter 4 Polarization Mode Dispersion (PMD) Monitoring

4.1 Overview of PMD

Polarization mode dispersion (PMD) is another important optical parameter to be monitored in future optical networks. PMD has its origins in optical birefringence and the random variation of the birefringent axes orientation along the fiber length. To a first-order approximation, PMD splits the optical pulses into two pulses polarized along the orthogonal principal state of polarizations (PSPs) and the two pulses will travel down the fiber at slightly different speeds. The resulting time difference is called the differential group delay (DGD) [58].

The three major causes of PMD are (i) intrinsic geometric asymmetries in the fiber core, (ii) external mechanical stress-induced variations in the fiber core, and (iii) birefringence of in-line components. Although telecommunication fibers are often called “single mode,” even in an ideal circularly symmetric fiber, there are two orthogonally polarized HE_{11} modes. In a perfect fiber, these modes have the same group delay. However, in reality, fibers have a certain amount of intrinsic geometric asymmetry which breaks the degeneracy of the orthogonally polarized HE_{11} modes, resulting in birefringence. The intrinsic geometric asymmetries arise when slightly elliptical instead of perfectly circular optical fibers are manufactured. These asymmetries will remain fairly constant over time. On the other hand, the external mechanical stress-induced asymmetries stem from a variety of sources including daily and seasonal heating and cooling, nearby vibration sources, and periodic

repair and maintenance. These asymmetries are typically dynamic in nature and cause the fiber PMD to vary stochastically in time (Fig. 4.1). In addition, although amplifiers or other components such as add-drop multiplexers in an optical system may have constant birefringence, variable polarization rotations between them due to the environment cause these components to randomly add to the PMD of the total system.

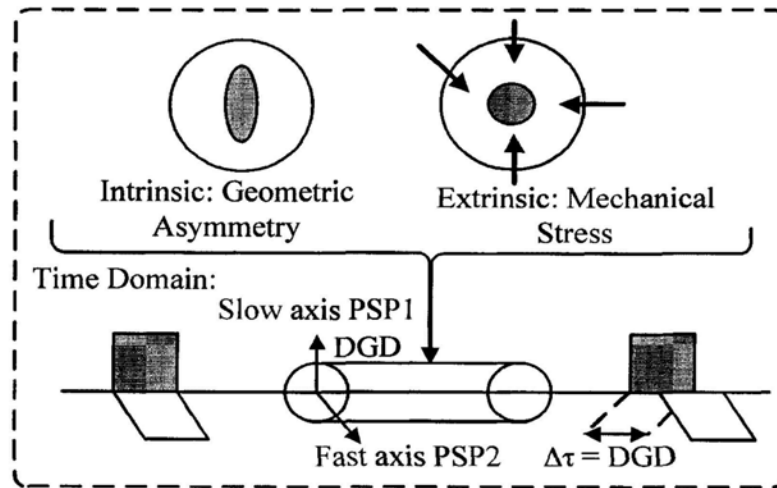


Fig. 4.1. Graphical representation of the DGD between the two PSPs caused by intrinsic geometric asymmetry and extrinsic mechanical stress-induced asymmetry of the fiber core

PMD is a deleterious effect in high-speed ($>10\text{-Gb/s}$) optical systems because the splitting pulse will cause crosstalk and inter-symbol interference (ISI) as shown in Fig. 4.2. It has been shown in several reports that the acceptable average DGD varies between 10% and 20% of a bit time depending mostly on the modulation format, outage probability, and receiver architecture [59]-[61]. It is particularly difficult to tackle PMD because the PMD effects are stochastic, time-varying, and temperature dependent, and worsen as the bit rate goes up. Moreover, instantaneous first-order PMD will follow a Maxwellian probability

distribution which always has some finite possibility of severe system penalties. Although much of the fiber sold today is rated as “low PMD” fiber ($<0.1\text{ps}/\sqrt{\text{km}}$), the presence of high-PMD legacy fiber and the PMD of in-line optical components make it necessary to monitor and compensate the effects of PMD. In the following section, we will review several reported PMD monitoring techniques. We will then propose and experimentally demonstrate two PMD monitoring schemes based on SPM-enhanced frequency-resolved SOP rotation and delay-tap asynchronous sampling technique, respectively.

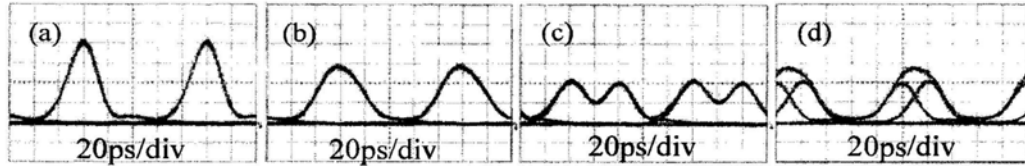


Fig. 4.2. Eye diagrams at PMD equals (a) 0, (b) $2T/5$, (c) $3T/5$, (d) $4T/5$, where T is the bit period and pulse width is $\sim 0.28T$

4.2 Previously Proposed Schemes for PMD Monitoring

4.2.1 PMD-Induced RF Dip Power Measurement

As explained before, PMD causes any given optical frequency component to split between the two orthogonal PSPs and travel at different speeds along the fiber. This speed differentially dephases the given frequency component on each PSP with respect to the carrier and generates a dip in the electrical spectrum after detection due to destructive interference. The worst case of detected RF power fluctuates with DGD according to [69]

$$P = P_0 \cos^2(\pi \cdot f \cdot \Delta\tau) \quad (4.1)$$

where P_0 is the RF power without PMD effects, and $\Delta\tau$ is the delay between the two PSPs. It can be easily deduced that the RF power fades periodically with PMD and the power fading notch is located at the frequency of $f = (2k+1)/(2 \times DGD)$. A band-pass filter (BPF) observing the intensity of a number of different notch components including the quarter bit rate frequency component, the half bit rate frequency component, and the bit rate frequency component can be used as first-order PMD monitors (Fig. 4.3) [65]-[71]. However, this method requires high-speed electrical circuits at the order of the bit rate and the sinusoidal PMD detection curve limits the maximum detection range.

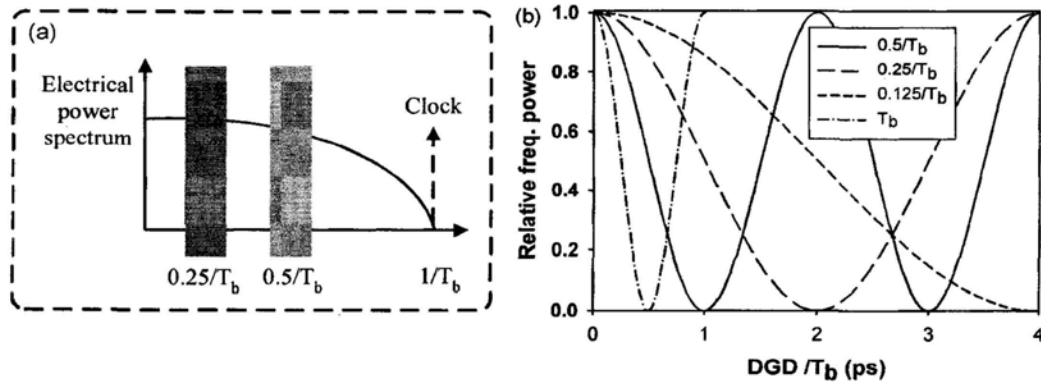


Fig. 4.3. (a) Proposed different frequency components for PMD monitoring (b) Received RF power variation versus DGD for 1/8, quarter, half, and bit rate frequency components (Adapted from Ref. [69])

4.2.2 Subcarrier-Based RF Power Fading Measurement

Based on the same idea, subcarrier-based PMD monitoring that allows simultaneous and independent PMD monitoring for WDM systems was proposed [72]. A subcarrier with the same power but slightly different frequency is added to each of the WDM channels. The subcarrier power fading due to PMD is strongly correlated to the PMD-induced degradation of that channel but is independent of that of the other channels. The

advantages of this scheme include the ability to monitor several WDM channels simultaneously and independently by a single module. Besides, the monitoring sensitivity and dynamic range can be easily adjusted by properly choosing the subcarrier frequency. However, this technique suffers from several disadvantages includes (i) sensitivity to chromatic dispersion, nonlinearities and four-wave mixing, (ii) power penalty induced by subcarrier, and (iii) requirement of transmitter modification.

4.2.3 Eye-Opening Penalty Monitoring

Measurement of the opening in the eye pattern can be another useful PMD monitor [73]-[74]. The eye monitor consists of two decision circuits in parallel. The first acts as the simple decision gate in a conventional receiver, and the second functions as a monitor gate with variable threshold to characterize the edges of the eye at variable phases. Since this technique evaluates the eye opening at the sample time, it needs a valid clock signal, called the synchronous control signal. While the eye opening is tightly correlated to the BER, it is affected by other distortion sources such as chromatic dispersion and nonlinearities.

4.2.4 Phase Diversity Detection

Phase diversity detection is an asynchronous method which measures the phase difference of a given frequency component after PSP filtering and electrical detection by using a Gilbert cell mixer [75]. The PMD is then inferred from the measured phase. This detection scheme is not affected by other distortion sources such as chromatic dispersion. However, it requires PSP tracking at the receiver, which is fairly complicated, and is also affected by higher-order PMD.

4.2.5 Arrival Time Measurement of Polarization-Scrambled Light

This method measures the arrival time variations of polarization-scrambled light by integrating the voltage-controlled oscillator (VCO) input signal of the clock recovery phase-locked loop (PLL) in the receiver [76]. It allows detection of PMD at or below the eye pattern visibility limit, has high monitoring sensitivity, and is usable in the presence of higher-order PMD. However, it requires polarization scrambling at the transmitter and has small dynamic range.

4.2.6 Degree-of-Polarization (DOP) Monitoring

The DOP of a signal represents how much of all the time components or frequency components of an optical signal are polarized along the same state of polarization (SOP). The DOP varies from 1, when the components are polarized along the same SOP, to 0, when the polarizations of the components are randomly scrambled. The principle of using DOP for PMD monitoring is as follows: When a pulse having a DOP of 1 (polarized along the same SOP) enters at a 45° angle with respect to PSPs of a fiber with first-order PMD, the leading edge of the pulse is polarized along the fastest PSP, while the middle of the pulse has the same SOP as the input pulse, and the trailing edge is polarized along the slowest PSP. Hence the output optical signal is no longer polarized along the same SOP and thus DOP is degraded [62]. This is illustrated in Fig. 4.4 and Fig. 4.5. Since the signal DOP degradation is proportional to the amount of signal pulse distortion caused by PMD, it can be used for in-service PMD monitoring [64].

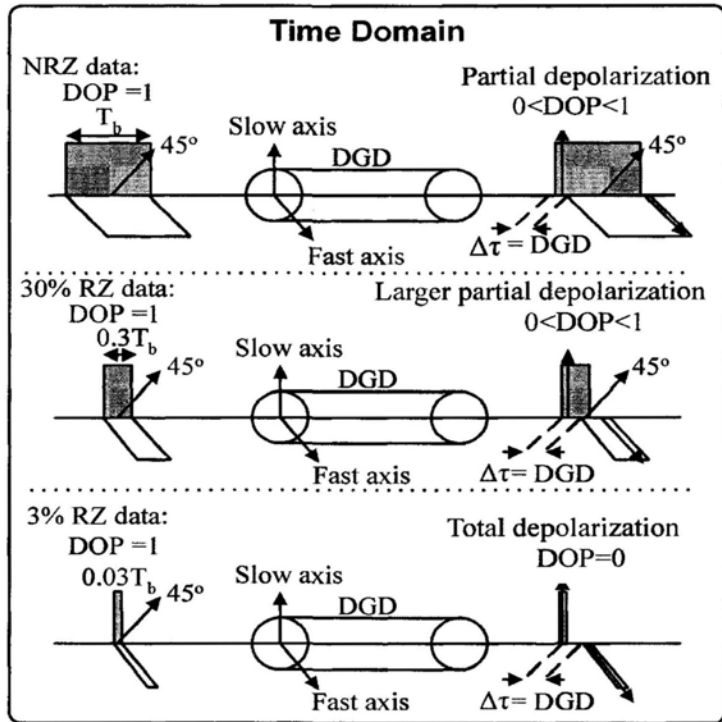


Fig. 4.4. Time-domain explanation of the depolarization effect for different pulse widths under the same DGD

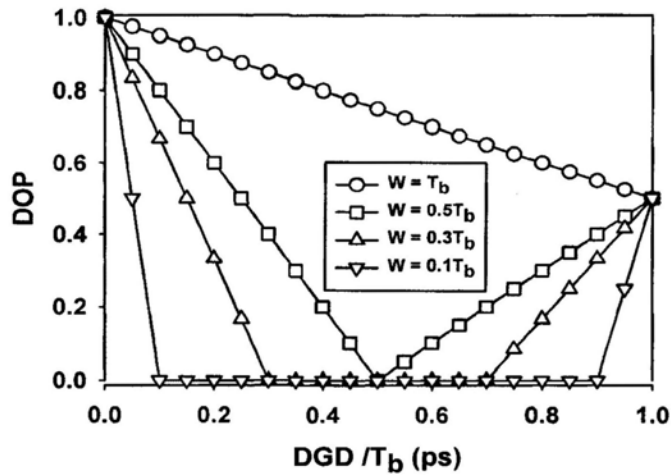


Fig. 4.5. Theoretical results of minimum DOP versus DGD (relative to the bit time, T_b) as the pulse width (W) of an RZ signal varies, assuming ideal rectangular pulse

PMD monitoring based on DOP is simple, bit-rate independent, without the need of high-speed electronics device, and insensitive to chromatic dispersion and the sign of the modulator chirp. However, it is sensitive to the input SOP, modulation format, the magnitude of the modulator chirp, fiber nonlinearity, and ASE noise. Also, this technique has low sensitivity for monitoring NRZ signal, and has small dynamic range for monitoring RZ signal [58][63][64].

4.2.7 Frequency-resolved SOP Rotation Monitoring

PMD-induced depolarization effect on optical signals occurs not only in the time domain, as explained in Fig. 4.4, but also in the frequency domain. As shown in Fig. 4.6, the link DGD causes the SOP of frequency components within the optical spectrum to rotate with respect to the central optical frequency by an amount $\pm 2\pi \times \Delta f \times \text{DGD}$ in Stokes space, where Δf is the frequency offset of a given component from the center of the optical spectrum. This is known as the ‘SOP walkoff’ effect which is the basic idea behind some offline PMD measurement methods performed in the frequency domain, such as Poincaré sphere or Jones matrix methods. In these methods, a tunable laser is used to sweep through a range of wavelengths and the PMD is derived from the output polarization states at different wavelengths.

The same idea was recently applied to in-service PMD monitoring to measure the PMD experienced by a real-time signal [77]-[79]. The measurement of DGD is performed by filtering the signal spectrum with a scanning filter at the receiver side and launching the filtered signal to a polarization analyzer. The tunable filter and polarization analyzer inside the frequency-resolved SOP rotation monitoring module are normally synchronized together to sample the polarization states at different filter

central wavelengths. The link DGD and pulsewidth (estimated DGD) are then derived from the measured wavelength-dependent SOP data.

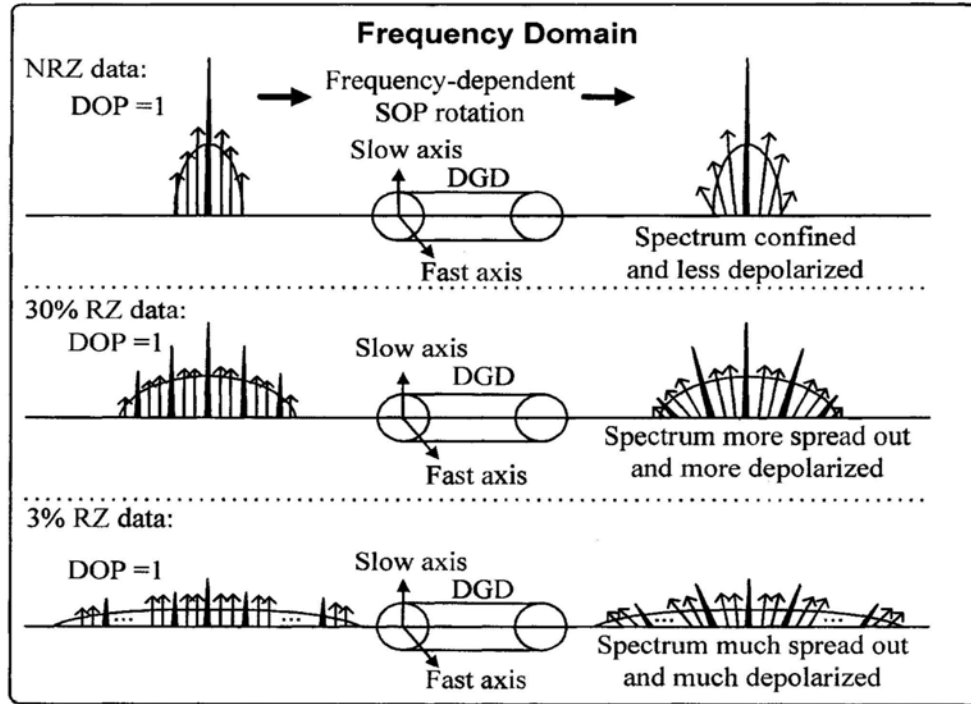


Fig. 4.6. Frequency-domain explanation of the depolarization effect for different pulse widths under the same DGD

When displayed on the Poincaré sphere, the polarization state at the output moves in a circle on the surface of the sphere as the optical frequency is varied, as shown in Fig. 4.7. The link DGD $\Delta\tau$ and effective DGD $\Delta\tau_{eff}$ are estimated from the polarization state rotation speed with respect to the optical frequency around the PSP and the sphere center, respectively, using the equation shown in the inset of Fig. 4.7. This scheme is real-time and non-disruptive. However, it has strict signal bandwidth, filter bandwidth requirement, as well as high computation complexity. To combat these restrictions, we propose to enhance the

scheme using self-phase modulation (SPM) effect which will be described in more details in next section.

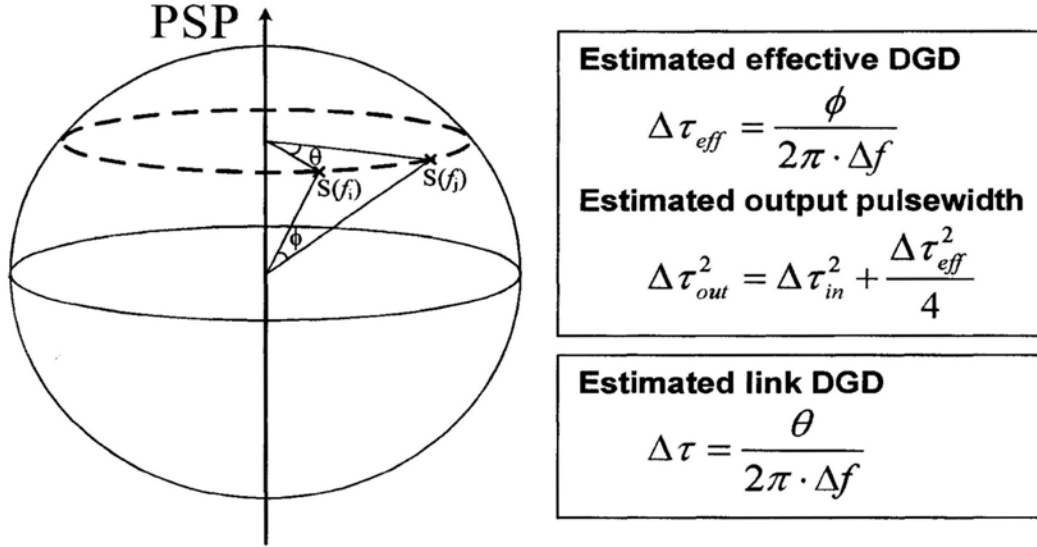


Fig. 4.7. The operation principle of PMD monitoring based on the frequency-resolved SOP rotation. $\Delta f=f_i-f_j$, $S(f_i)$, $S(f_j)$ are the output polarization states at frequencies f_i and f_j , respectively

4.3 Enhanced PMD Monitoring with Frequency-resolved SOP Rotation by SPM

As discussed in last section, experiments that utilized a tunable bandpass filter at the receiver side to analyze SOP for in-service PMD and pulsewidth distortion monitoring have been reported recently [77]-[79]. Though this monitoring scheme is real-time and non-disruptive [77], it has some limitations. First, the monitoring accuracy is critically affected by the stability of the optical tunable filter [78]-[79], since any drift and dithering of the central wavelength will eventually lead into uncertainties

in the Stokes vector measurements. Second, complicated de-convolution computation must be performed to reconstruct an accurate results, whenever a optical tunable filter passband profile is not sufficiently narrow, causing low pass filtering effect of the signal's Stokes vector function [78]. Also, the estimation accuracy of the PSP, and hence the DGD values, is limited by the number of sampling points of the SOP values and hence this scheme is only suitable for narrow picosecond pulse ($< 10\text{ps}$) transmission systems which have wide optical spectrum, providing enough SOP samples [79].

To generalize, the measurement accuracy of the frequency-resolved SOP rotation based PMD monitoring scheme is determined by the normalized filter bandwidth, which is defined as the ratio of the FWHM bandwidth of the filter over that of the signal spectrum [79]. This implies that there are two alternative ways to improve the measurement with the same degree of accuracy: (1) to employ a narrow bandwidth filter or (2) to broaden the signal spectrum.

In this section, we propose and experimentally investigate the use of SPM-induced spectrum broadening to enhance in-service PMD monitoring by frequency-resolved SOP analysis. The idea is to broaden the signal spectrum using SPM effect and alleviate the above-mentioned limitations so as to provide several desirable features including:

- (i) providing more sampling points;
- (ii) allowing a larger filtering step such that simple averaging could be performed instead of complicated de-convolution;
- (iii) improving the filter drifting tolerance, and
- (iv) being suitable even for use with a large pulsewidth.

In our experiment, it was found that, for 10-Gbit/s optical systems with pulsewidths of 28 ps and 2.5 ps, SPM-assisted PMD measurement results agreed very well with reference PMD measurements, with DGD values ranging from 2 ps to 25 ps.

4.3.1 Experimental Results and Discussion

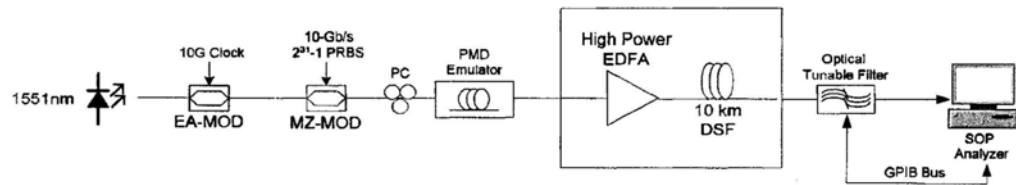


Fig. 4.8. Experimental setup of PMD monitoring with the assistance of SPM effect, PC: polarization controller, MOD: modulator, DSF: dispersion shifted fiber

Fig. 4.8 shows the experimental setup of our proposed scheme. A 1551-nm CW light source was fed into an EAM driven by a 10-GHz sinusoidal wave to generate a 10-Gbit/s 28-ps full-width at half-maximum (FWHM) RZ pulse train. The RZ pulse train was then sent to an optical Mach-Zehnder intensity modulator and modulated with $2^{31}-1$ PRBS. The modulated RZ pulse stream was then fed into a polarization controller (PC) and a PMD emulator implemented by different lengths of polarization-maintaining fiber (PMF). The DGD values of these PMFs were measured in advance by a PMD analyzer (EXFO FPMD5600) for reference. In order to investigate the SPM effect on the wavelength domain SOP rotation, a high power EDFA and a 10-km dispersion-shifted-fiber (DSF) (zero-dispersion wavelength at ~ 1570 nm, and nonlinear coefficient γ 1.8) were placed after the PMD emulator, to introduce the SPM effect and broaden the signal spectrum. The PMD

parameter of the DSF used in our experiment was as small as $0.05 \text{ ps}/\sqrt{\text{km}}$; thus the additional measurement error induced by the 10-km DSF was negligible. To control the SPM effect level, a variable optical attenuator (VOA) was added after the EDFA to adjust the injection power into the DSF. The spectrum-broadened signal was then fed into a tunable fiber-grating filter with 0.22-nm 3-dB bandwidth (JDSU TB90226) and a polarization analyzer (Agilent 8509C). The depolarization effect of ASE was negligible in our experiment with proper ASE filtering by the tunable filter. A computer program provided synchronization between the tunable filter and the polarization through a GPIB bus. The tuning step of the filter was about 0.01 nm. After sweeping the filter over the broadened spectrum, the corresponding SOP value was sampled and recorded. A circle-fitting algorithm was then employed to find out the PSP from the SOP trajectory, and the corresponding DGD can be obtained by calculating the SOP rotation rate around the PSP with respect to wavelength. The SOP scanning time was less than 1 minute, which needs further reduction to match the response time requirement of the millisecond range in PMD compensation systems.

Fig. 4.9(a) shows the signal spectra with and without SPM in the absence of PMD, with the injection power to EDFA maintained at 20 dBm. Without SPM, the 3-dB bandwidth of the signal spectrum was about 0.2 nm. For such a narrow spectrum, not enough sample points could be obtained and the measurement error could be as large as 30% even with de-convolution calculations [79]. With SPM, the signal spectrum exhibited a seven-fold broadening to 1.4 nm. To facilitate the investigation, we employed a parameter, SPM level ($\Delta\phi_{\max}$), which is defined as the maximum nonlinear phase shift induced by the SPM effect, $\Delta\phi_{\max} = \gamma P_{\text{peak}} L_{\text{eff}}$, where P_{peak} is the peak power and L_{eff} is the effective

length [80]. In the case with SPM-broadened spectrum, the corresponding SPM level is 2.5.

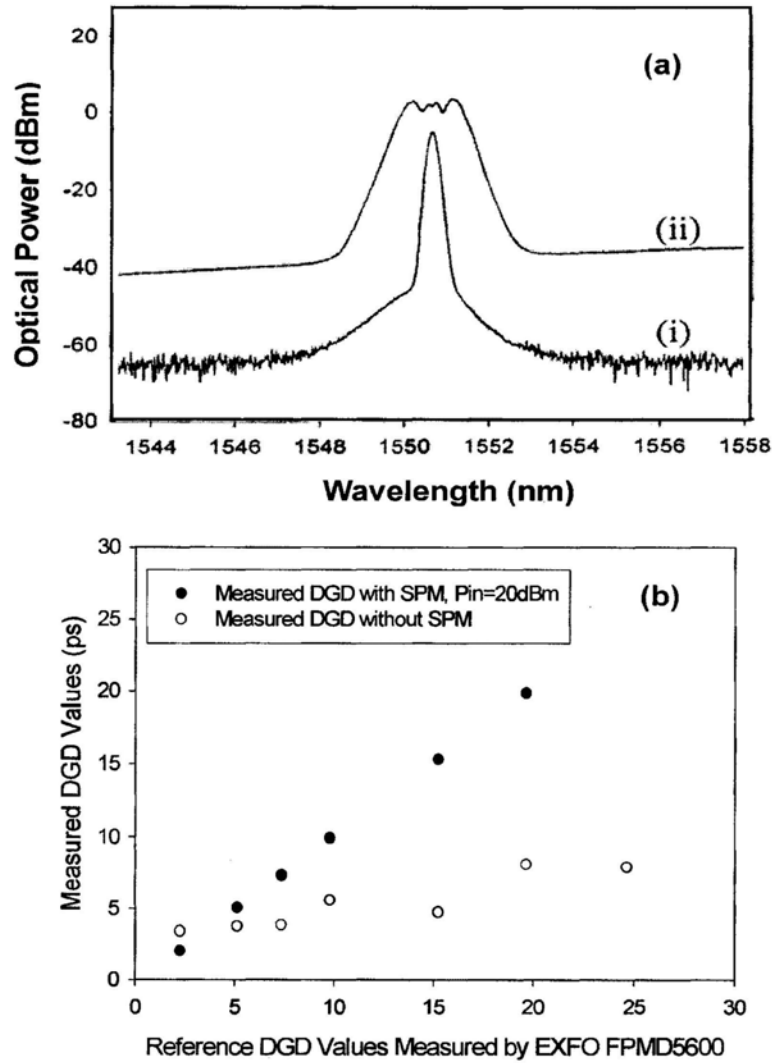


Fig. 4.9. (a) The spectrum of the signal with 28-ps FWHM pulsewidth (i) without SPM, (ii) with SPM, $P_{in}=20\text{dBm}$; (b) The measured DGD values by analyzing frequency-resolved SOP rotation with/without SPM effect versus the reference DGD values for the 28-ps FWHM pulsewidth signal

Fig. 4.9(b) shows the PMD monitoring results with and without SPM. With the introduction of SPM, the average measurement error was only about 2%, compared with an average error of 52.16% and 30% in conventional schemes without and with de-convolution calculation [79], respectively. This improvement could be explained by the improved PSP estimation in the circle-fitting algorithm due to the additional sample points obtained from the SPM broadened spectrum. Also, the normalization of the SOP vector [78] was employed to reduce the potential error induced if the input SOP was nearly parallel or orthogonal to the PSP of the transmission link. Apart from the improved accuracy, SPM-assisted PMD monitoring also had a lower computational complexity. Unlike previous works [78]-[79], this scheme required no prior knowledge of the filter profile for the complicated de-convolution calculation, and simple averaging could be employed. Furthermore, our experimental results showed that, without the assistance of SPM, the previous schemes based on frequency-resolved SOP rotation could not work well for cases with wider pulsewidths even after de-convolution, whereas this enhanced scheme could help extend the application pulsewidth range.

We also characterized the effects of SPM level on the PMD monitoring accuracy as an excessive SPM level might induce extra degradation in measurement performance. Pulses with four different power levels, 10 dBm, 17 dBm, 18.5 dBm and 20 dBm, were launched to the DSF fiber, and the DGD value was varied from 2 ps to 25 ps. In order to enhance the SPM effect, RZ pulses with 2.5-ps FWHM pulsewidth from a fiber ring laser (PriTel Ultrafast Optical Clock Source) were used.

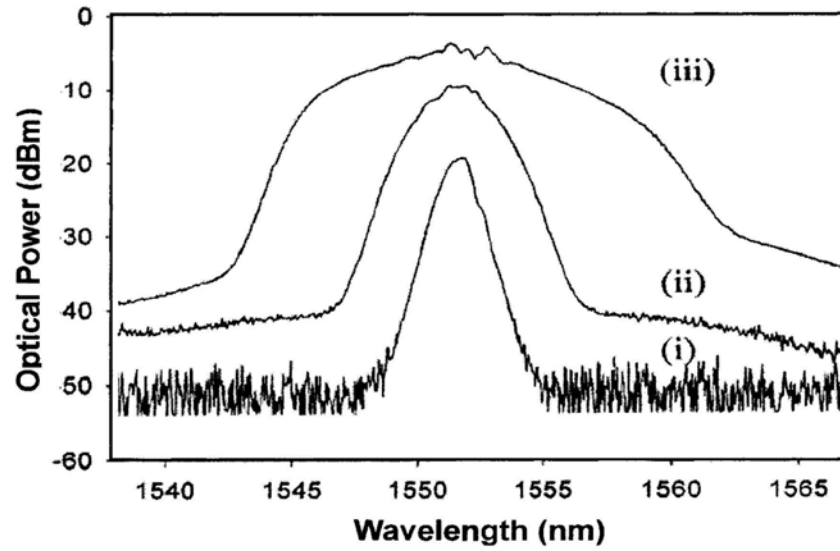


Fig. 4.10. The spectra of the signal with 2.5-ps FWHM pulsewidth (i) without SPM (ii) with SPM, $P_{in}=10\text{dBm}$ (iii) with SPM, $P_{in}=20\text{dBm}$

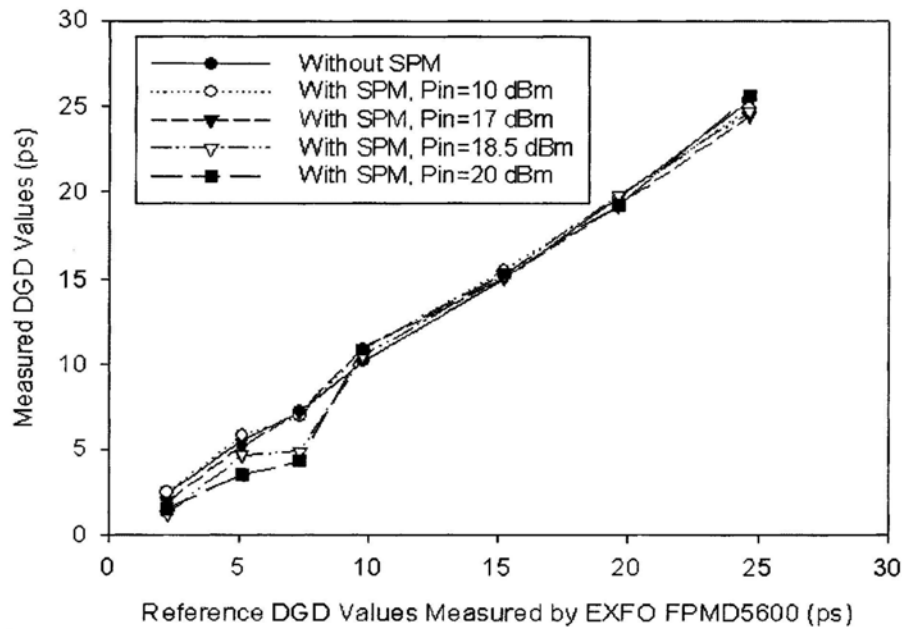


Fig. 4.11. The measured DGD values by analyzing frequency-resolved SOP rotation with/without SPM effect versus the reference DGD values for the 2.5-ps FWHM pulsewidth signal.

The spectra are shown in Fig. 4.10 and the relationship between the measured DGD values and the reference DGD values is shown in Fig. 4.11. It was found that with input power of 17 dBm and below, the measured DGD values agreed very well with the reference values taken by a commercial PMD analyzer, with an average estimation error less than 10%. However, for input power higher than 18.5 dBm, although measured DGD values also agreed well with the reference DGD values when the value was larger than 10 ps, large errors occurred for DGD values less than 7 ps. To further investigate this deviation, we studied the SOP trajectory on the Poincaré spheres for three cases: (i) without SPM, (ii) with SPM and launched power = 10 dBm, (iii) with SPM and launched power = 20 dBm. Fig. 4.12(a) shows the SOP trajectory on the Poincaré spheres with 15.2-ps reference DGD value. In this case, the SOP rotated around the PSP for nearly the same amount in all three cases, with a wavelength scanning range of 0.4 nm. However, in Fig. 4.12(b)(iii), the SOP trajectory on the Poincaré sphere with 5.1-ps reference DGD value showed large fluctuation at 20-dBm input power. This could be attributed to the intra-channel XPM-induced nonlinear polarization rotation when the two orthogonal polarization components were partially overlapping for small DGD values. This showed therefore that the excessive input power introduced additional measurement error.

In short, while SPM effect can improve PMD monitoring, very high input power should be avoided to maintain monitoring accuracy. In our experiment, the marginal case with good monitoring accuracy was at a launched power of about 17 dBm with 2.5-ps FWHM pulsewidth data pulses being fed into 10-km DSF fiber with nonlinear coefficient γ of 1.8. This corresponds to an SPM level of about 28, which is sufficiently high to cope with most practical cases.

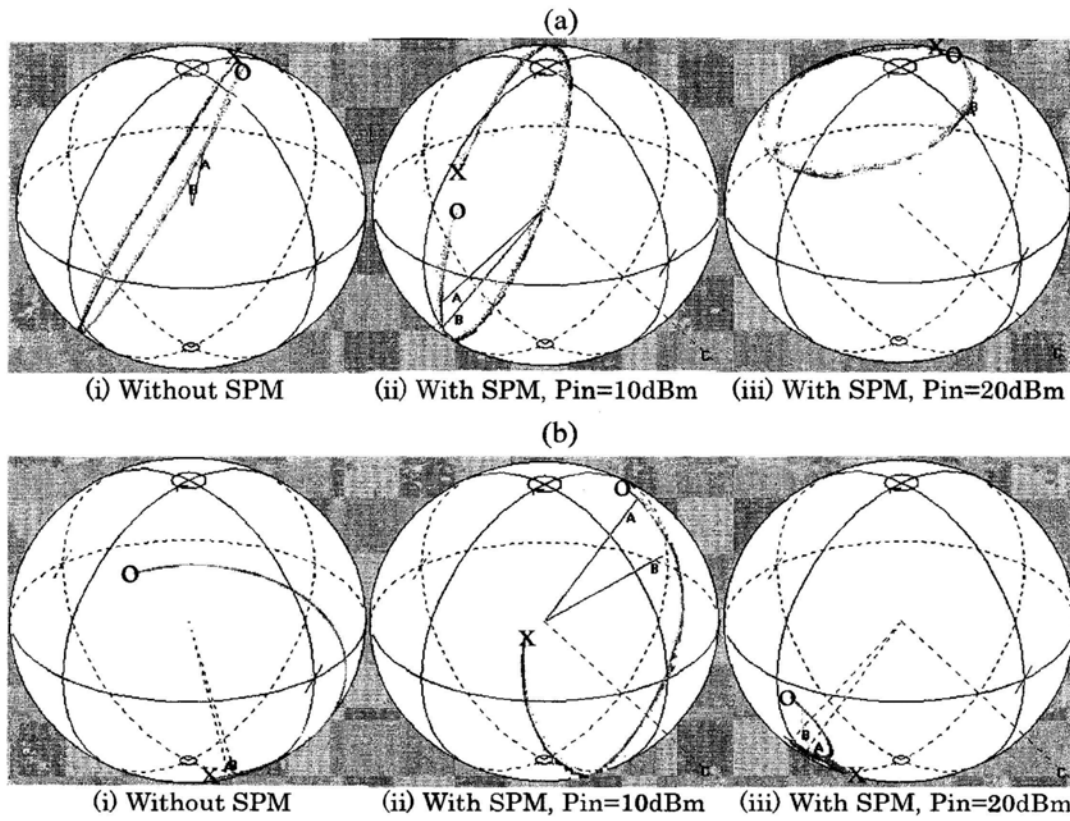


Fig. 4.12. The SOP trajectories on Poincare sphere (X: Start Point; O: End Point), (a) when DGD is 15.2ps and the wavelength scanning range is 0.4nm, and (b) when DGD is 5ps and the wavelength scanning range is 1 nm, (i) without SPM, (ii) with SPM, $P_{in}=10\text{dBm}$, and (iii) with SPM, $P_{in}=20\text{dBm}$.

4.3.2 Input SOP Dependency Analysis

One limitation of the scheme based on the frequency-resolved SOP rotation measurement is that, if the input SOP is nearly parallel or orthogonal to the PSP of the transmission link, potential measurement error will be introduced. Actually the error comes from the resolution limitation of the polarimeter. When input SOP gets closer to the PSP, the diameter of the circular trace is limited and therefore the distance

between two consecutive measurement points is reduced. If the distance between two measurement points is shorter than the resolution of the polarimeter, they may be indistinguishable from each other. Thus error is introduced in the subsequent curve-fitting algorithm. With a smaller DGD, the angular difference $\Delta\theta$ and the geometric distance between two consecutive measurement points are smaller. For different input SOP there is a minimum measurable DGD at which the distance between two consecutive measurement points is equal to the resolution of the polarimeter. Let the resolution of polarimeter be d_{\min} , i.e. the minimum distance that can be resolved on a Poincaré sphere; then the DGD must satisfy the following equation (see Fig. 4.13)

$$DOP \cdot \sin \phi \cdot \Delta\theta \geq d_{\min} \quad (4.2)$$

where $\Delta\theta = DGD \cdot \Delta\omega$.

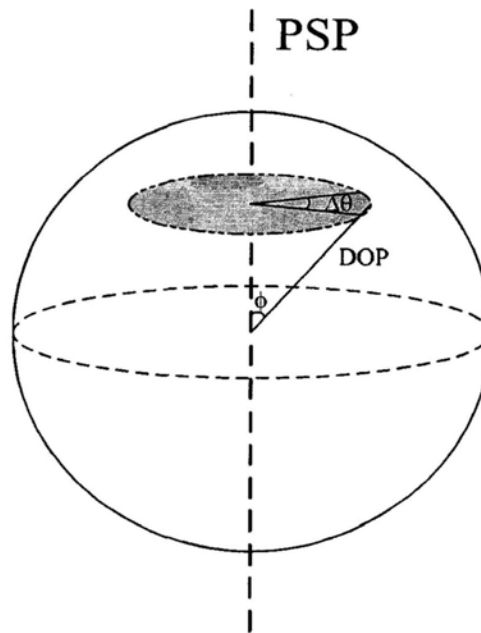


Fig. 4.13. Illustration of the relationship between input DOP and PSP

Thus this error will limit the minimum measurable DGD, which is determined by the following equation derived from [81]:

$$DGD \cdot DOP \cdot \sin \phi \cdot (2\pi \frac{\Delta\lambda \cdot c}{\lambda^2}) \geq d_{\min} \quad (4.3)$$

where ϕ is the angle between the input SOP and PSP, $\Delta\lambda$ is the wavelength spacing between two SOP sampling values, and d_{\min} is the resolution of the polarimeter, i.e. the minimum distance that can be resolved on a Poincaré sphere. With the minimum DOP,

$$DOP = \exp\left[\frac{-(\pi \cdot BW \cdot DGD)^2}{4 \cdot \ln(2)}\right] \quad [82],$$

where BW is the FWHM bandwidth of the filter, we can obtain the upper bound of the minimum measurable DGD. In our experiment, $\Delta\lambda$, d_{\min} and BW are 0.01 nm, 0.0005 and 27.5 GHz, respectively. Thus the upper bound of the minimum measurable DGD value can be obtained numerically from equation (4.3) and is plotted in Fig. 4.14. It is clear that once the input SOP is fully aligned with PSP ($\phi=0,\pi$), the measurement error induced will approach infinity. However, beyond a small misalignment angle between the input SOP and PSP, the minimum measurable DGD is small enough for practical application. For instance, when ϕ is 0.08 radian (or 4.6°), the minimum measurable DGD can still be kept below 0.8 ps, showing the reliability of the proposed scheme. In actual deployment, if a small measurable DGD is desirable, one may improve the measurement by increasing the filter scanning step size appropriately. All the PMD measurement schemes based on Poincaré sphere or Jones matrix method will suffer from the same problem, including the previous frequency-resolved SOP rotation scheme. In our experiment, measurement data are discarded when the obtained circular traces are too small. In [83], to overcome this limitation, the received signal is launched to an additional fixed DGD element at the receiver side to reduce the input SOP dependency.

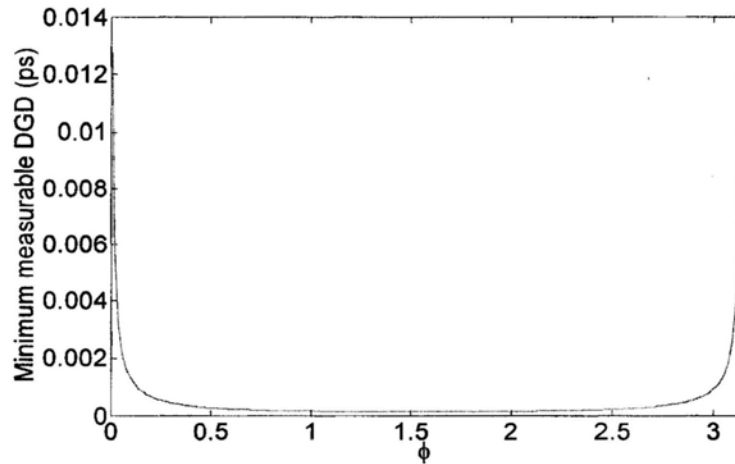


Fig. 4.14. The minimum measurable DGD for different angles between input SOP and PSP.

To sum up, in this section, an enhanced scheme for frequency-resolved SOP rotation based in-service PMD monitoring was proposed and experimentally demonstrated. By using the SPM effect to broaden the signal spectrum, it has been shown that the computation complexity and the estimation error of the PMD monitoring were significantly reduced. In next section, we will propose and demonstrate another simple PMD monitoring scheme which is based on delay-tap asynchronous waveform sampling technique.

4.4 PMD Monitoring Using Delay Tap Asynchronous Waveform Sampling

The eye-diagram technique is a simple but powerful measurement method for assessing the data-handling ability of a digital transmission system [85]-[86]. It has been used extensively for evaluating the performance of wire systems and can also be applied to optical fiber data links. By

superimposing the power variation within each period to form a variety of data patterns, the effects of waveform distortion are allowed to be shown immediately on an oscilloscope. Nevertheless, in order to generate eye diagrams properly, a complicated clock extraction process from the signal is required so that the sampling can be synchronized to the signal bit rate. On the other hand, asynchronous sampling techniques dispense with clock extraction, so they are transparent to clock rate and signal format [87]. However, the sacrificed information makes identifying some causes of signal degradation challenging, as different impairments can cause similar changes in histogram shape. There have been a number of techniques proposed to reconstruct eye diagrams from the asynchronous samples [88]. However, they rely on highly stable sampling rates and significant signal processing.

Recently, a new asynchronous sampling technique, called delay-tap asynchronous waveform sampling, was proposed which resolves the power evolution within each bit, providing a direct measure of waveform distortion without clock extraction [84]. In this section, we describe and demonstrate the use of delay-tap asynchronous waveform sampling technique to realize effective PMD monitoring in RZ-OOK systems. By simultaneously sampling the incoming waveform with a fixed temporal delay, the waveform characteristics can be obtained without the need of clock synchronization. The scheme is simple and has no particular sampling rate nor stability requirements. PMD monitoring by the technique was experimentally demonstrated. A measurement range up to 50ps can be achieved for 10-Gb/s signal.

4.4.1 Concept of Delay Tap Asynchronous Waveform Sampling

The proposed alignment monitoring scheme is based on the delay-tap asynchronous waveform sampling technique [84] as illustrated in Fig. 4.15. Signal samples are taken at a rate of $1/T_s$, which can be much slower than the system clock. Each sample point consists of two measurements (x and y) separated by a fixed time delay Δt . The x and y values are then plotted in pairs to form a two-tap scatter plot as shown in Fig. 4.15(b). If adjacent bits 01 are sampled, the sample would fall on the left vertical edge of the two-tap plot. Similarly, the diagonal, bottom horizontal edge and the origin correspond to adjacent bits 11, 10 and 00, respectively. Since this plot provides signal waveform characteristics similar to eye diagram, impairments such as PMD and modulation misalignment (which will be investigated in Section 5.3) can be observed from its evolution.

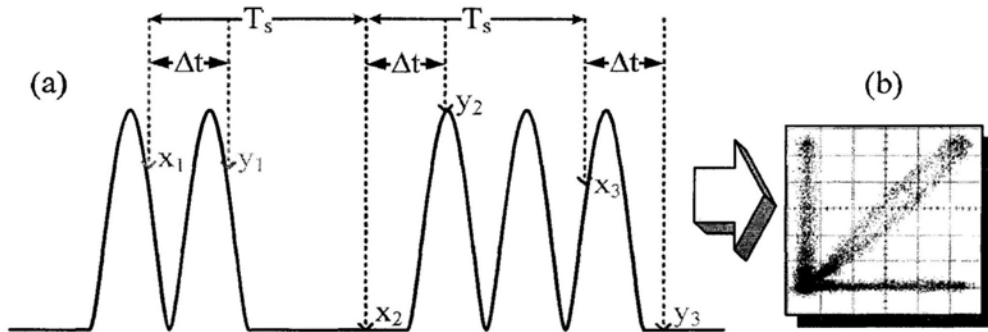


Fig. 4.15. (a) Delay-tap asynchronous sampling. T_s =sampling period, t =timing offset within each sampling. (b) A sample delay-tap scatter plot for RZ-OOK signal at Δt =bit-period.

4.4.2 Experimental Results and Discussion

Fig. 4.16 shows the experimental setup used to investigate the proposed scheme, a CW light at 1547 nm was carved into a 10-Gb/s pulse train with

a pulse width of 28 ps via an electro-absorption modulator (EAM), driven by a 10-GHz sinusoidal clock signal. The pulse train was then modulated with a 10-Gb/s NRZ PRBS of pattern length $2^{31}-1$ using a LiNbO₃ Mach-Zehnder intensity modulator (IM). The optical delay line (ODL) was used to align the pulse train and data modulation. At the output of the RZ-OOK transmitter, the signals was fed into a PMD emulator which produces DGD from 0 ps to 90 ps before being fed into a delay-tap asynchronous sampling system in which a signal was first detected using a photo-detector. Then the detected signal was split into two branches with relative delay of Δt , before being sampled by a 50-MHz triggered low-speed analog to digital converter. Finally, a computer was used to collect and analyze the samples. In our experiment, Δt was set to be $T/2$, where T equals to one bit period (100 ps) for 10-Gb/s signals.

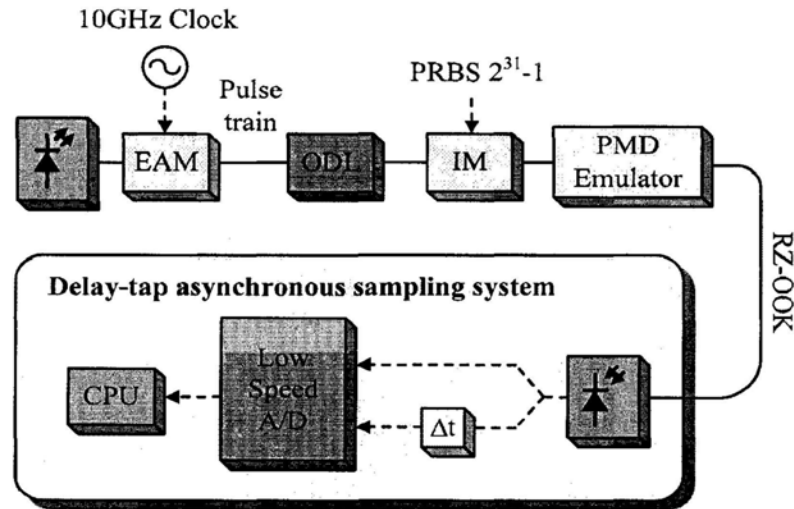


Fig. 4.16. Experimental setup. EAM: electro-absorption modulator; ODL: optical delay line; IM: intensity modulator

Fig. 4.17 shows the two-tap scatter plots obtained at different DGD values in a 10-Gb/s RZ-OOK system. For the cases without PMD (i.e. DGD=0 ps), it is observed that the left vertical and the bottom horizontal edges of the scatter plots are the longest. Increasing the DGD value would

shorten the edges for $DGD < T/2$, but lengthen the edges for $DGD > T/2$, where T is the bit period. For instance, when $DGD=50$ ps, the lengths of the left vertical and the bottom horizontal edges are shortened to only half of their original values when $DGD=0$ ps, as shown in Fig. 4.17; while their respective lengths are nearly restored to their original values at $DGD=90$ ps.

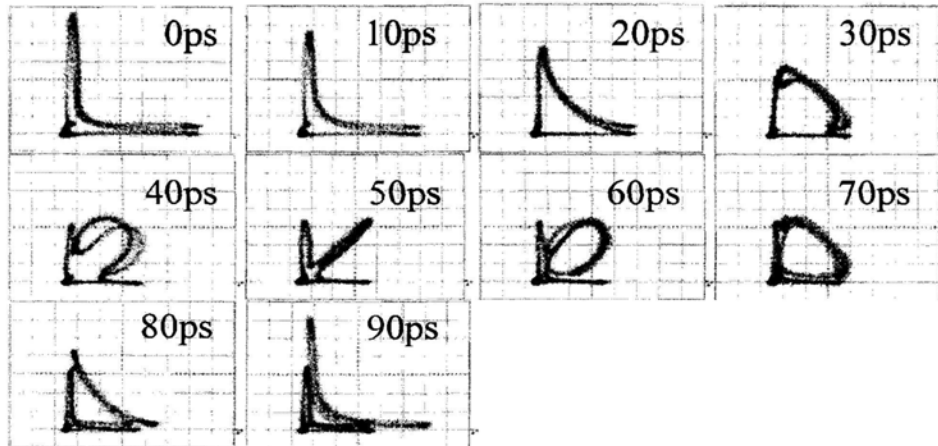


Fig. 4.17. Two-tap scatter plots under different DGD values

The evolution of the left vertical and the bottom horizontal edges offer a potential means for monitoring PMD. We take the following parameter to investigate this effect:

$$m = \frac{\text{number of sample points falling on the left and the bottom edges}}{\text{total number of sample points on the scatter plot}}$$

Since the left vertical and the bottom horizontal edges of the scatter plot correspond to the signal amplitude transitions, the parameter m represents the proportion of the rising and the falling edges of the signal in terms of time, which is independent of signal amplitude.

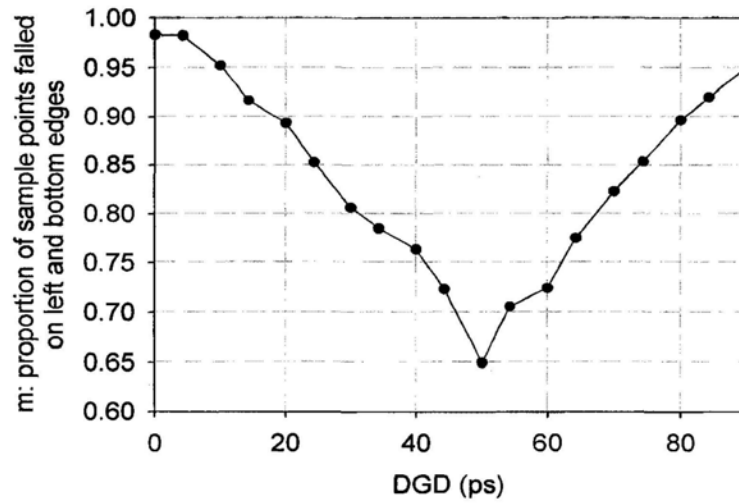


Fig. 4.18. Measured plots for parameter m at different DGD values

Fig. 4.18 shows the values of the parameter m based on the experimentally measured sample values. It is shown that m decreases monotonically with the increase of DGD up to half of the bit rate. Therefore, an unambiguous monitoring of PMD up to 50% of signal bit period is successfully achieved.

4.5 Summary

Table 4.1. Comparison between the two proposed PMD monitoring schemes: (1) Enhanced Frequency-Resolved SOP Rotation Analysis and (2) Delay-tap Asynchronous Waveform Sampling

| | Enhanced Frequency-Resolved SOP Rotation Analysis by SPM | Delay-tap Asynchronous Waveform Sampling |
|------|--|--|
| Pros | <ul style="list-style-type: none"> ● High sensitivity | <ul style="list-style-type: none"> ● Simple setup ● High measurement range |
| Cons | <ul style="list-style-type: none"> ● High cost ● Low measurement range | <ul style="list-style-type: none"> ● Lower sensitivity |

In this chapter, two PMD monitoring schemes have been proposed and experimentally demonstrated. The first one is an enhanced scheme for frequency-resolved SOP rotation based in-service PMD monitoring. By using the SPM effect to broaden the signal spectrum, it has been shown that the computation complexity and the estimation error of the PMD monitoring were significantly reduced. The second one is based on the delay-tap asynchronous sampling technique. By observing the evolution of the left and the bottom edge, PMD up to 50 ps can be successfully monitored. Comparison between the two proposed schemes is summarized in Table 4.1.

Chapter 5 Modulation Alignment Monitoring

5.1 Generation of Return-to-Zero (RZ) Signal

Return-to-zero is the preferred data modulation format for high bit-rate ultra long-haul (ULH) dense wavelength-division multiplexed (DWDM) optical transmission systems [89]. It is because, RZ modulation results in receiver performance superior to that for NRZ modulation by 1 to 2 dB. Also, systems can be designed to be more robust against impairments such as self-phase modulation (SPM) and polarization mode dispersion (PMD) with RZ modulation.

Although RZ modulation offers improved performance, transmitters for RZ modulation are more complex and expensive than those for NRZ modulation. Generally, two cascaded modulation stages are required, one to form the pulses and a second to modulate the pulses to imprint the data on the signals. The order of the two modulation stages may be changed in some cases.

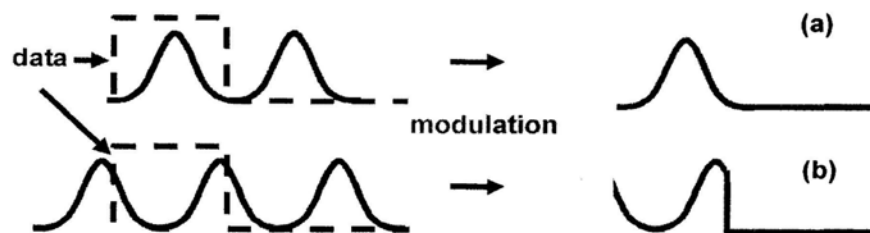


Fig. 5.1. Modulation output when pulse carver and data modulator are (a) properly aligned, and (b) misaligned.

In order to generate the RZ signal properly, the peak of the RZ pulses should be aligned to the middle of the data bit period, as shown in Fig. 5.1(a). However, due to temperature variation and device aging, the relative time delay of the optical and electrical devices can drift over time [90]-[92]. If there is any misalignment between the pulse carver and data modulator, improper amplitude / phase transition would appear within each pulse, and the pulses would have broken shape (see Fig. 5.1(b)) and result in erroneous detection. Therefore proper synchronization between pulse carver and data modulator must be implemented to avoid severe impact on the transmission performance.

In laboratory, pulse carver and data modulator are synchronized by manually adjusting a delay line that provides certain time delay Δt . Usually adjustment of the delay line is based on bit-error rate (BER) readings from BERT or synchronous eye diagram on a digital oscilloscope. This is acceptable for laboratory operation. However, for real operation, a low cost, automatic approach is preferred.

To realize automatic synchronization, we may tap out part of the modulated signal and feed into an alignment monitoring module which can provide timing misalignment information. The misalignment information is then fed back to the delay line for automatic adjustment. For the alignment monitoring module, there have been several schemes proposed for return-to-zero on-off-keying (RZ-OOK) and return-to-zero differential-phase-shift-keying (RZ-DPSK) systems. They will be reviewed in next section. After that, we will propose and experimentally demonstrate two modulation misalignment monitoring schemes, one for RZ-OOK and one for RZ-DPSK systems.

5.2 Previously Proposed Schemes for Alignment Monitoring

5.2.1 Modulation-Misalignment-Induced RF DIP Power Measurement

In [90], it was found that the timing misalignment between the pulse carver and data modulator in RZ-OOK system would generate spectral null at $\sim 0.64 \times$ bit rate as shown in Fig. 5.2. The power of the spectral null is inversely proportional to the amount of timing misalignment. Therefore, by detecting the amount of the power in the frequency band immediately around the expected nulling frequency, the timing misalignment can be deduced. This scheme is low-cost and has large dynamic range. However, it is unable to distinguish different misalignment directions.

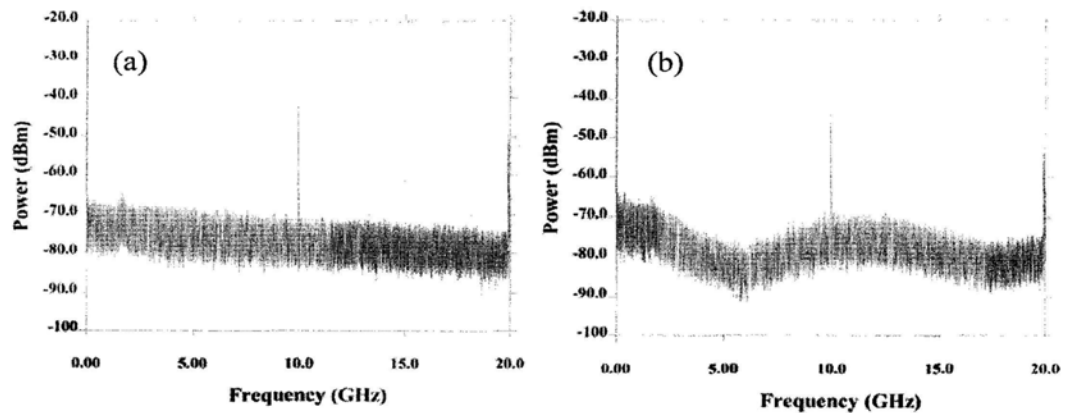


Fig. 5.2. RF power spectrum when pulse carver and data modulator are (a) aligned and (b) misaligned (Adapted from Ref. [90])

5.2.2 Optical Spectral Asymmetry Measurement

If electroabsorption modulator (EAM) is used as the data modulator in an RZ-OOK transmitter, then when there is modulation misalignment, chirp

will be induced and results in asymmetric optical spectrum as shown in Fig. 5.3. In [91], it was proposed to use a wedged etalon filter to extract the asymmetric sidebands and compare their power so that both the misalignment sign and the magnitude can be determined. This scheme has high sensitivity. However, it only works for modulators which introduce chirp. Therefore it may not be applicable when dual-drive Mach-Zehnder interferometer (DD-MZI) is used as data modulator in the system, because no chirp is induced in DD-MZI.

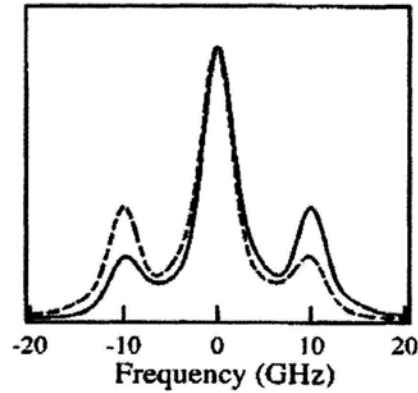


Fig. 5.3. Solid (dashed) curve is the measured optical when the pulse carver leads (lags) the data modulator by 20 ps. (Adapted from Ref. [91])

5.2.3 DOP Reduction Measurement

The above described schemes are both for RZ-OOK system. For RZ-DPSK system, it has been reported that alignment status can be monitored by measuring DOP reduction of the signal [92]. The alignment monitoring module consists of a polarization maintaining fiber (PMF), a polarizer and a power meter, as shown in Fig. 5.4. The polarization launching angle of the incoming light into the module should be finely adjusted to be 45° with respect to the slow and fast axes of the PMF. The PMF introduces a finite DGD to induce SOP variation within the phase transition region (i.e. the ris-falling edges) of the phase modulation. Therefore when the pulse carver is not well-aligned with the data modulator, the SOP variation

region will move toward the maximum transmittance of the RZ pulses. As a result, the DOP of the output signal decreases, as the timing misalignment increases. The change in DOP indicates the amount of modulation misalignment and it can be easily detected by a polarizer and power meter. This scheme has small monitoring power dynamic range of ~ 0.2 dB. Also it is polarization sensitive.

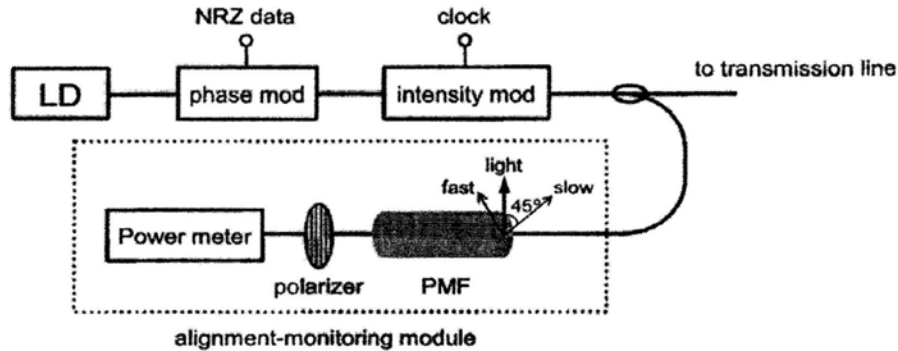


Fig. 5.4. Modulation alignment monitoring in RZ-DPSK systems by measuring DOP reduction (Adapted from Ref. [92])

5.3 RZ-OOK Alignment Monitoring Using Delay Tap Asynchronous Waveform Sampling

In this section, we describe and experimentally demonstrate the use of delay-tap asynchronous waveform sampling technique described in Section 4.4.1 to realize a modulation alignment scheme in RZ-OOK systems. The scheme is applicable to any kind of optical intensity modulator, and is able to determine both the magnitude and the direction of modulation misalignment.

5.3.1 Experimental Results and Discussion

Since the same sampling technique is used here, the experimental setup is similar to the one described in Section 4.4.2. Fig. 5.5 shows the

experimental setup used to investigate the proposed scheme, a CW light at 1547 nm was carved into a 10-Gb/s pulse train with a pulse width of 28 ps via an electro-absorption modulator (EAM), driven by a 10-GHz sinusoidal clock signal. The pulse train was then modulated with a 10-Gb/s NRZ PRBS of pattern length $2^{31}-1$ using a LiNbO₃ Mach-Zehnder intensity modulator (IM). The optical delay line (ODL) was used to provide different misalignments between the pulse train and the data modulator. At the output of the RZ-OOK transmitter, the signals was fed into a delay-tap asynchronous sampling system in which a signal was first detected using a photo-detector. Then the detected signal was split into two branches with relative delay of Δt , before being sampled by a 50-MHz triggered low-speed analog to digital converter. Finally, a computer was used to collect and analyze the samples. In our experiment, Δt was set to be exactly one bit period (100 ps for 10 Gbit/s).

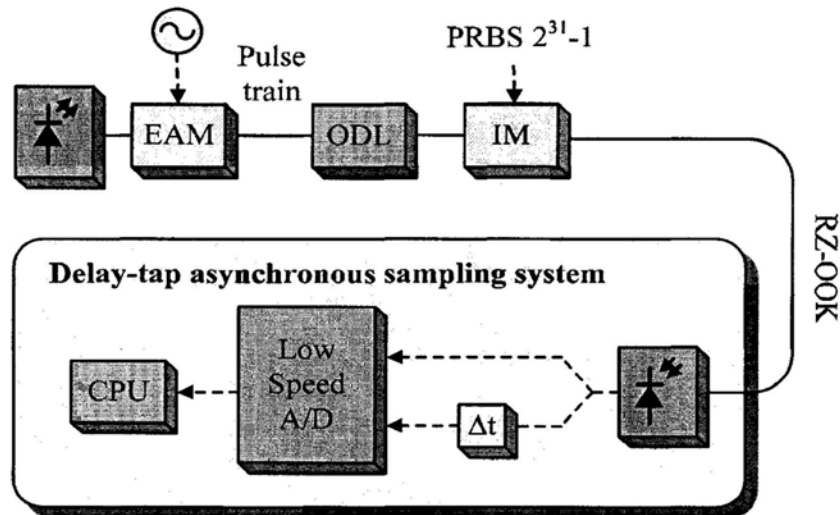


Fig. 5.5. Experimental setup. EAM: electro-absorption modulator; ODL: optical delay line; IM: intensity modulator

First we investigate the power penalty induced by misalignment in RZ-OOK systems. With reference to the receiver sensitivity with perfect

alignment at bit-error rate (BER) of 10^{-9} , the power penalty for different timing misalignment between the pulse carver and the data modulator was obtained and depicted in Fig. 5.6. Notice that when timing misalignment exceeds ± 20 ps, the power penalty increases rapidly. Eye diagrams for the signal with different misalignments are provided in Fig. 5.7. The eye is severely degraded by timing misalignment, and therefore high penalty is resulted.

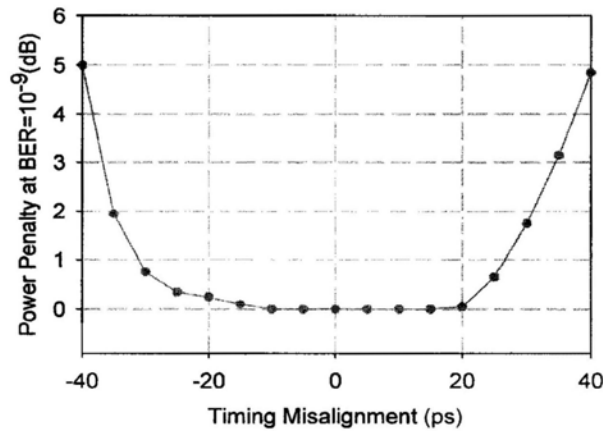


Fig. 5.6. Power penalty vs timing misalignment for RZ-OOK system with 28-ps pulsewidth.

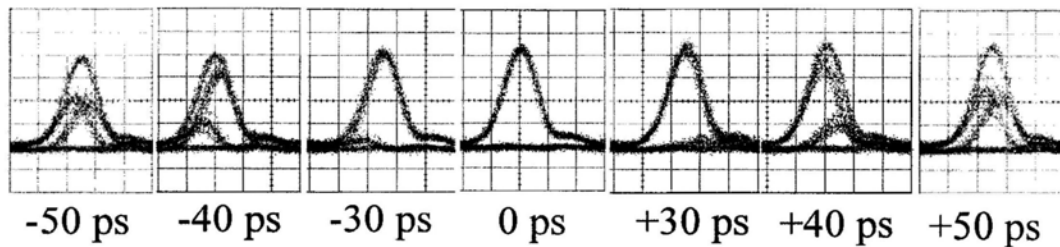


Fig. 5.7. Eye diagrams for the signal with different modulation misalignments.

Fig. 5.8 shows the two-tap scatter plots obtained at different modulation timing misalignments. For misalignment of 0 ps, the scatter plot has clear diagonal. Increasing misalignment to 30 ps starts to cause the sample

points on the diagonal to disperse. In addition, the negative and positive misalignments induce different opposite rotational directions to the diagonal sample points. For example, the diagonal points of the -40-ps plot rotate in counter-clockwise direction, while that of the +40-ps plot rotate in clockwise direction. Note that the -50-ps and +50-ps cases are identical in 10-Gb/s systems since the bit period is equal to 100 ps.

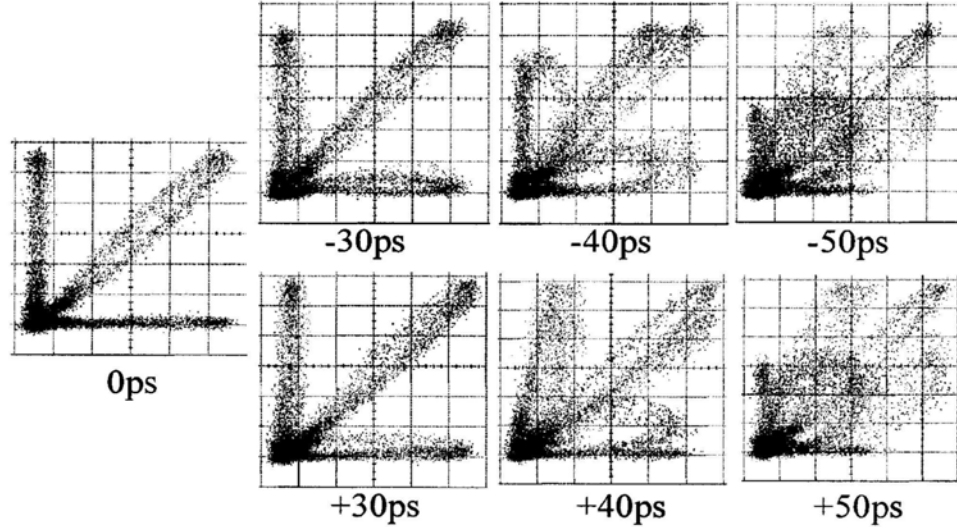


Fig. 5.8. Two-tap scatter plots for different modulation timing misalignments

The increasing dispersion and the rotation of the sample points on the diagonal offer a potential tool for monitoring the modulation misalignment status. We design two parameters to investigate this effect:

$$d = \frac{1}{n} \sum_i \sqrt{x_i^2 + y_i^2} \sin \left(\left| \frac{\pi}{4} - \arctan \frac{y_i}{x_i} \right| \right) \quad (5.1)$$

$$t = \frac{1}{n} \sum_i \arctan \frac{y_i}{x_i} \quad (5.2)$$

d represents the average distance of every sample points from the diagonal, while t represents the average angle of the sample points from the origin. For these two parameters we just consider the top-right part of

the plots so as to reduce the influence from the vertical and the horizontal edges, and n is the total number of considered sample points.

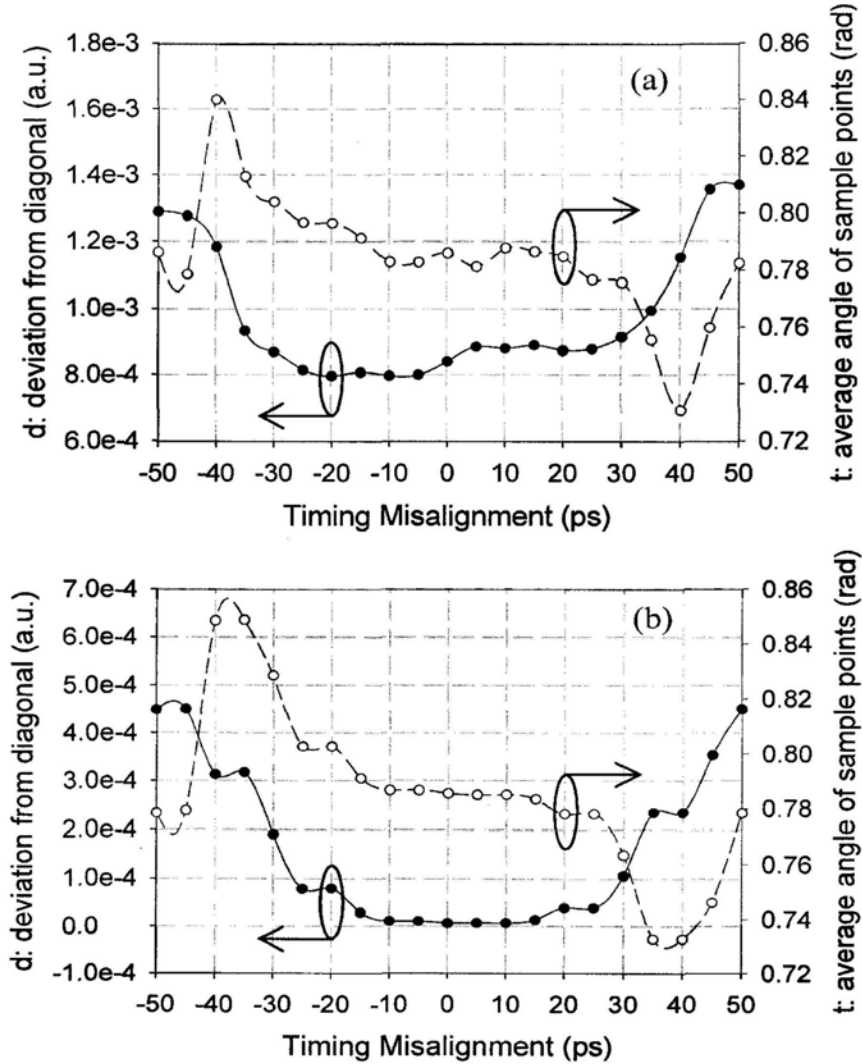


Fig. 5.9. d and t for different misalignment obtained by (a) experiment, and (b) simulation using *OptSim™*

Fig. 5.9(a) shows the experimentally obtained d and t . It is shown that d starts to increase when misalignment induced eye distortion starts to become significant at around 20 ps (see Fig. 5.6). On the other hand, t can reflect the misalignment direction because it is larger than $\pi/4$ for

negative misalignment while it is smaller than $\pi/4$ for positive misalignment. Therefore, by using both of the curves, both of the magnitude and direction of misalignment can be deduced. We have also performed simulation for the proposed scheme using OptSimTM and the results are depicted in Fig. 5.9(b). It is shown that the experimental results and simulation results agree very well.

To sum-up, we have proposed and experimentally demonstrated the use of delay-tap asynchronous waveform sampling technique to monitoring the alignment between the pulse carver and the data modulator in RZ-OOK systems. This scheme is simple, and is able to determine both the misalignment magnitude and direction. It is expected that the RZ-OOK transmitter robustness can be improved by integrating the proposed scheme to provide feedback control for automatic alignment. In next section, we will propose and demonstrate a modulation alignment monitoring scheme based on off-center optical filtering.

5.4 RZ-DPSK Alignment Monitoring Using Off-center Optical Filtering

Recently, RZ-DPSK has attracted much research interest for its higher tolerance against impairments due to fiber nonlinearities and 3-dB sensitivity improvement with balanced detection, compared with RZ-OOK. Same as the case for RZ-OOK systems, in order to ensure proper synchronization between pulse carver and data modulator in RZ-DPSK systems, it is essential to monitor the modulation alignment status for automatic feedback adjustment.

In a conventional RZ-DPSK transmitter, the phase modulation can be implemented by a dual-drive Mach-Zehnder modulation, or a LiNbO₃

phase modulator. In the former case, the phase modulated light exhibits amplitude dips at the points of phase change, which will cause output power drop once misalignment happens. Thus, the misalignment monitoring can be easily achieved by monitoring the average output power. Whereas in the latter case, the phase modulated light still maintains constant output power, making its modulation alignment status more difficult to be monitored. In Section 5.2.3, we have reviewed a modulation alignment monitoring scheme for phase modulator based RZ-DPSK system. However, it is polarization sensitive and only has small monitoring dynamic range.

In this section, we propose and experimentally demonstrate a novel yet simple modulation alignment monitoring scheme for phase modulator based RZ-DPSK systems. An off-center optical filter is employed to capture the chirp induced by misalignment. Thus, by monitoring the optical power at the filter output, the alignment status can be obtained. The proposed scheme is simple, low-cost, polarization insensitive and has high monitoring sensitivity.

5.4.1 Principle of Proposed Technique

As shown in Fig. 5.10(a), when the pulse appears in the middle of the data bit period, there is no timing misalignment between the pulse carver and the data modulator, which corresponds to the perfect alignment status. However, when there is a certain misalignment between the pulse carver and the data modulator such that parts of the pulses enter the phase transient region between data bits, phase variation occurs inside the pulses and induces frequency shift, which is given by:

$$\Delta f = \frac{\Delta\theta}{2\pi \cdot \Delta t} \quad (5.3)$$

where Δf is the induced frequency shift and $\Delta\theta / \Delta t$ is the rate of phase variation. Therefore the signal spectrum is broadened. This broadening is determined by the rise and fall times of phase modulation, i.e. $\Delta\theta / \Delta t$, and the timing misalignment. The worst misalignment case is that the pulses appear at the transition edge of phase modulation, so that the modulated pulses experience the maximum phase variation and hence the maximum spectrum broadening.

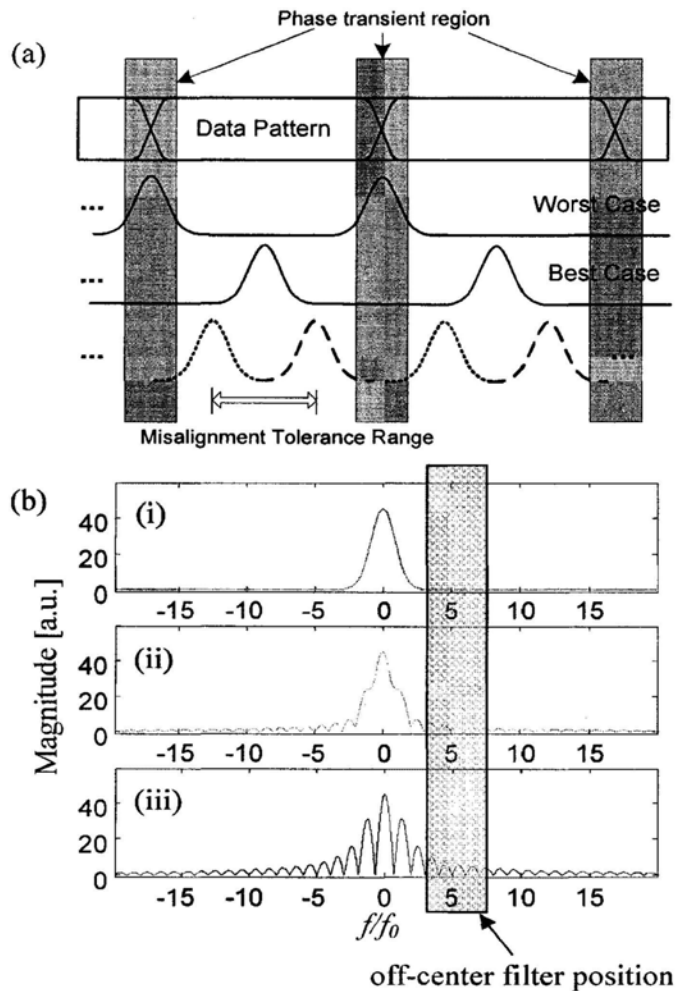


Fig. 5.10. (a) Illustration of timing alignment between pulse carver and data modulator. (b) Calculated signal spectra with timing alignment between pulse carver and data modulator of (i) 0, (ii) $0.3T$, and (iii) $0.5T$ in a 10-Gb/s RZ-DPSK system with $\sim 0.28 \cdot T$ pulsewidth

Assuming that the NRZ RF driving data of phase modulator is rectangular-shaped and RZ optical pulse is Gaussian-shaped with T_0 and peak power P , the power spectral density of the misaligned RZ-DPSK signal can be written as

$$\zeta(f) = \frac{|G(f)|^2}{T} \quad (5.4)$$

and

$$G(f) = \sum_{k=-\infty}^{+\infty} \sqrt{2\pi P T_0} \frac{\sin((2\pi f - 2\pi k f_0)T/2)}{(2\pi f - 2\pi k f_0)/2} \exp\left(-\frac{k^2(2\pi f)^2 T_0^2}{2} - j(2\pi f - 2\pi k f_0)t_0\right) \quad (5.5)$$

where T is the data period and t_0 is the timing misalignment, $f_0=1/T$ is the bit rate. Fig. 5.10(b) shows the power spectrum profile for $T_0=0.18T$ (FWHM of pulse: $\sim 0.28T$) with different amounts of misalignment. With the increased misalignment amount, the signal spectrum is broadened. So, by filtering out a narrow slice from the edge of the signal spectrum, any misalignment-induced spectrum broadening will be translated into an increased output power from the optical filter as shown in Fig. 5.10(b). Thus, the degree of misalignment between the pulse carver and the data modulator can be monitored by simple power monitoring after the filter.

As shown in Fig. 5.11, the typical RZ-DPSK transmitter consists of a continuous-wave (CW) laser, an electro-absorption modulator (EAM) for pulse carving and an optical phase modulator. The optical pulse train generated by a clock-driven EAM is modulated via a data-driven optical phase modulator. At the output of the RZ-DPSK transmitter, a portion of power is tapped off and fed into the proposed alignment monitoring module, which only consists of an optical band-pass filter (BPF) and an optical power meter. The passband of the optical filter is adjusted to be offset from the signal center wavelength. The output power of the filter serves as a monitoring signal of the timing misalignment.

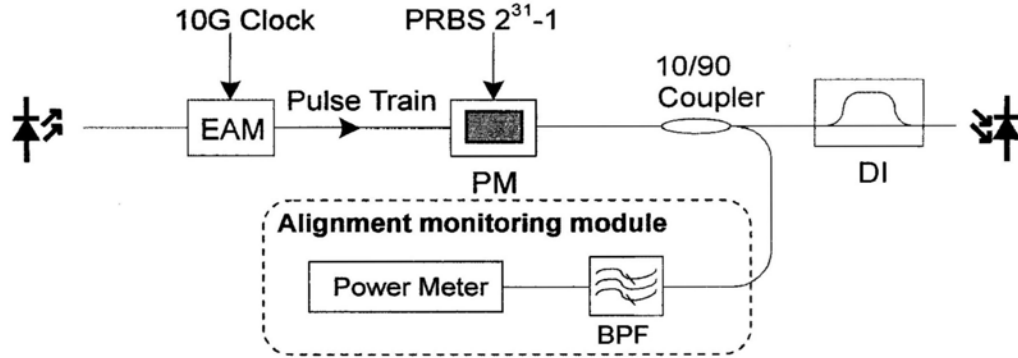


Fig. 5.11. Proposed alignment module. EAM: electroabsorption modulator; PM: phase modulator; DI: delay interferometer; BPF: bandpass filter

5.4.2 Experimental Results and Discussion

The experiment setup is shown in Fig. 5.11. A CW light at 1558 nm was carved into a 10.61-Gb/s pulse train with a pulse width of 28 ps via an EAM, driven by a 10.61-GHz sinusoidal clock signal. The pulse train was then modulated with a 10.61-Gb/s NRZ PRBS of pattern length $2^{31}-1$ using a LiNbO₃ phase modulator. For the direct detection of DPSK signals, a single-ended delay interferometer (DI) with 94-ps arm delay was employed in front of a PIN photodiode having an electrical bandwidth of about 11 GHz.

First, we investigate the power penalty induced by misalignment in RZ-DPSK systems. With reference to the receiver sensitivity with perfect alignment at bit-error-rate (BER) = 10^{-9} , the power penalty at different timing misalignment between the pulse carrier and the data modulator was obtained, shown as the solid symbols in Fig. 5.12. The degraded eye diagrams due to misalignment with (a) -32 ps and (b) +32 ps are shown in the insets of Fig. 5.12, which corresponds to around 4-dB power penalty. Notice that when the timing misalignment exceeds ± 15 ps, the power penalty increases rapidly. The timing alignment range of -15 ps to +15 ps

is referred as the misalignment tolerance range, which is affected by the rise and fall times of phase modulation, pulse shape and duty cycle of pulse train. The similar behaviour was obtained in BER performance, shown as the open symbols in Fig. 5.12. The BER was measured under different timing alignment with a received optical power of -20.9 dBm. Fig. 5.13 shows the optical spectra with resolution bandwidth of ~ 0.1 nm and eye diagrams for the case without misalignment (inset (a) of Fig. 5.13) and with 47-ps misalignment (inset (b) of Fig. 5.13), which corresponds to the worst case when the pulse is drifted to the edge of the data bit. Compared with the perfect alignment case, the eye is severely degraded, and the spectrum is noticeably broadened.

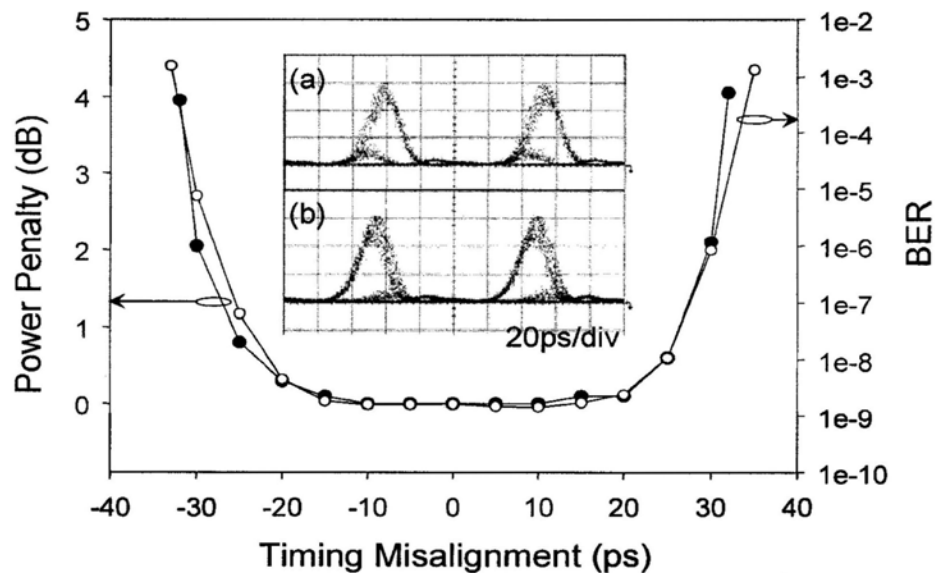


Fig. 5.12. Power and BER for different timing misalignments. Insets: Degraded eye diagrams due to misalignment of (a) -32 ps and (b) 32 ps

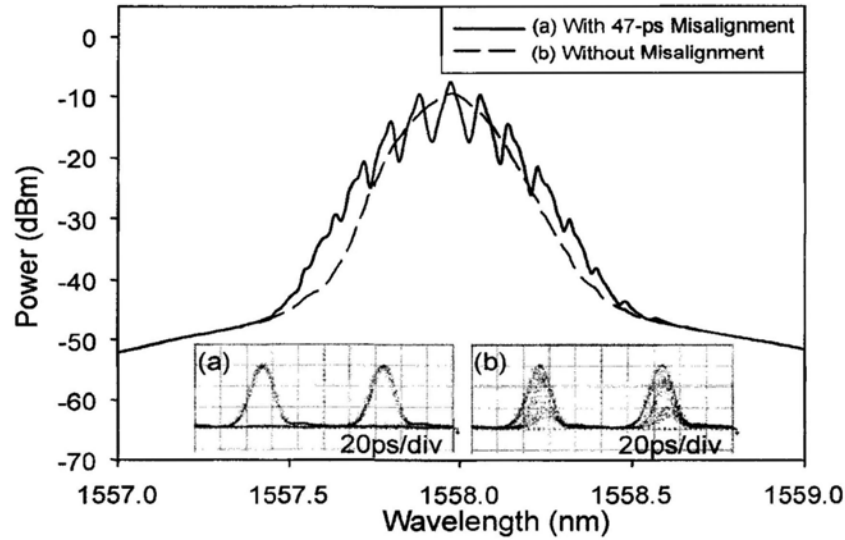


Fig. 5.13. Optical spectra for perfect alignment (solid line) and worst-case misalignment (dashed line). Inset: Eye diagrams

In the proposed monitoring module, a small amount of the modulated signal (10%) was tapped off and sent to an off-center optical band-pass filter with a passband of 0.22 nm. A filter with smaller bandwidth will be helpful to distinguish the spectrum change due to misalignment. However, as there are periodic power nulls in the signal spectrum as shown in Fig. 5.10(b) and Fig. 5.13, if the filter bandwidth is smaller than the nulls spacing, i.e., the bit rate, the monitoring power change will fluctuate with respect to the filter center frequency. This will make the monitoring much more sensitive to the filter center frequency stability. So, the bandwidth of the filter should be wider than the nulls spacing (the bit rate) to reduce filter position sensitivity. In particular, a filter with bandwidth of 0.22 nm (~ 25 GHz) was applied in a 10 Gb/s system in our experiment. The filter center frequency should be chosen to give the maximum monitoring dynamic range. The optimized filter offset position is related to the filter bandwidth and the spectrum bandwidth of the signal without timing misalignment. In order to achieve the maximum monitoring power

dynamic range, it is desirable to scan the filter center frequency for the perfect and worst alignment cases, respectively, to find out the optimal center frequency of tunable filter.

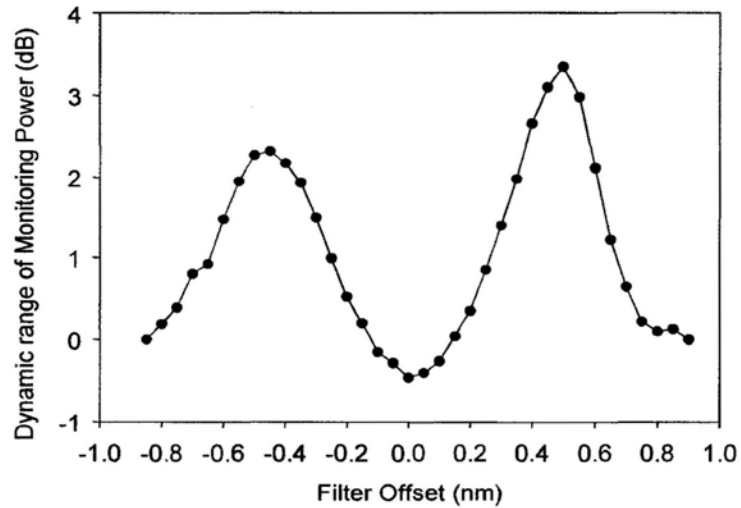


Fig. 5.14. MPDR for different filter offsets

Fig. 5.14 shows the monitoring power dynamic range (MPDR), which is defined as the ratio of the output power for half-bit-period, 47-ps, misalignment (the worst case) to the output power for perfect alignment. A maximum MPDR of 3.35 dB was obtained when the optical filter was placed at 0.5-nm offset from the signal center wavelength. Compared with the DOP-based alignment monitoring scheme proposed in [92], in which the MPDR is 0.2 dB, the proposed scheme shows a significant improvement of around 3.15 dB on MPDR, thus substantially improving the monitoring sensitivity. Meanwhile, it eliminates the polarization control for the signal before launching into the monitoring module. The asymmetry of the curve is attributed to the difference between the phase variation at the rising and the falling edges, which can also be verified by the asymmetric spectrum (solid line) shown in Fig. 5.13.

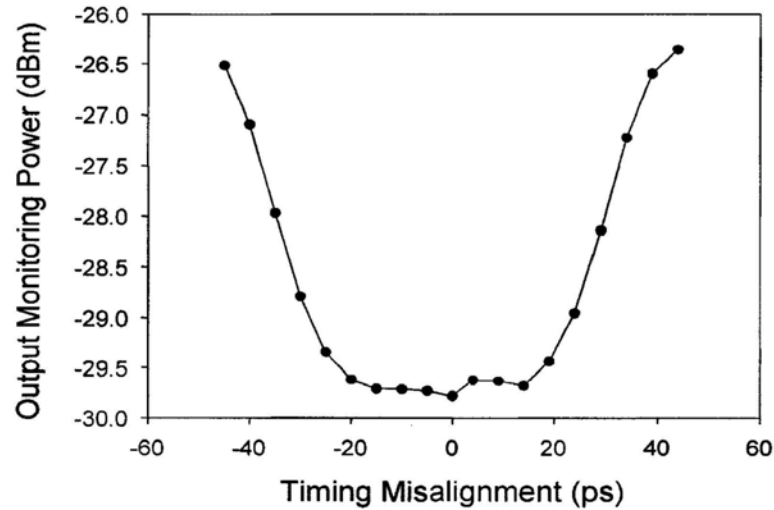


Fig. 5.15. Output monitoring power for different timing misalignments

Fig. 5.15 shows the detected monitoring signal power versus the timing misalignment when the filter offset is set to 0.5 nm. Within the timing alignment range of -15 ps to +15 ps, i.e. the misalignment tolerance range, the monitoring signal exhibits a minimum power. This can be further manifested in Fig. 5.12, as the misalignment penalty also approaches to zero in this region. Once the timing misalignment is $> +20$ ps or < -20 ps, the power of the monitoring signal drastically increases with a slope of $\sim \pm 0.15$ dB/ps as shown in Fig. 5.15. This again matches the abrupt change in the power penalty curve for misalignment $> +20$ ps or < -20 ps as depicted in Fig. 5.13. Thus, with the monitoring module in the RZ-DPSK transmitter, it can effectively circumvent the potential power penalty induced by misalignment between pulse-carver and data modulator.

In next section, we will apply the same off-center optical filter technique to monitor the synchronization of data signals in synchronized phase re-modulation (SPRM) systems.

5.5 SPRM Alignment Monitoring Using Off-center Optical Filtering

5.5.1 Introduction to SPRM

Recently, synchronized phase re-modulation (SPRM) has become a crucial signal processing technique to erase the original and write the new phase information simultaneously for phase-encoded modulation formats. Applications include optical label swapping in optical networks, the re-modulation of the downstream signal for upstream transmission in wavelength division multiplexing passive optical networks (WDM-PON), and the generation of spectral efficient orthogonal modulation format [93]-[96]. Fig. 5.16 illustrates the principle of SPRM. The old differential phase shift keying (DPSK) signal is re-modulated by a delta DPSK data, which is obtained by performing exclusive OR operation between the detected old DPSK data and the new DPSK data in electrical domain. In binary phase-encoded signal, a π phase change applied to either symbol will swap the original symbol to the other symbol, as shown in the inset of Fig. 5.16. Therefore, by using SPRM, the old DPSK signal is erased and the new DPSK signal is written simultaneously. To properly achieve SPRM, the electrical delta DPSK data should be superimposed onto the time slot center of the old optical DPSK signal. However, the long relative time delay between the incoming DPSK signal and the delta DPSK data drifts over time due to temperature variation and imperfect clock recovery in the SPRM module, which increases the difficulty of SPRM and hinders its practical applications.

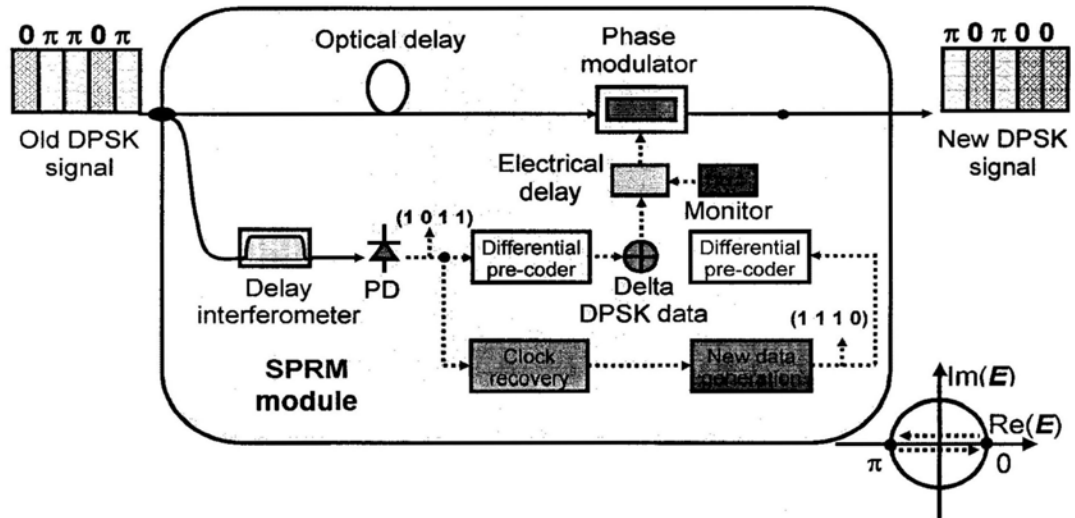


Fig. 5.16. Principle of SPRM to simultaneously erase old DPSK data and write new DPSK data. Inset: constellation diagram for DPSK.

To solve this problem, we propose a simple technique using a narrowband optical bandpass filter (OBPF) to monitor unsynchronized phase re-modulation. The obtained monitoring signal is fed back to control the delay between the incoming DPSK signal and the electrical delta DPSK data for automatic SPRM. We experimentally show that the proposed method is applicable to both non-return-to-zero DPSK (NRZ-DPSK) and return-to-zero DPSK (RZ-DPSK) formats. With the optimal central wavelength of the OBPF, -1.2-dB and 3.8-dB monitoring power dynamic ranges (MPDRs), defined as the ratio of the monitoring power for the worst case of phase re-modulation to that for the best case, are obtained for NRZ-DPSK and RZ-DPSK formats respectively, therefore achieving high monitoring sensitivity.

5.5.2 Experimental Results and Discussion

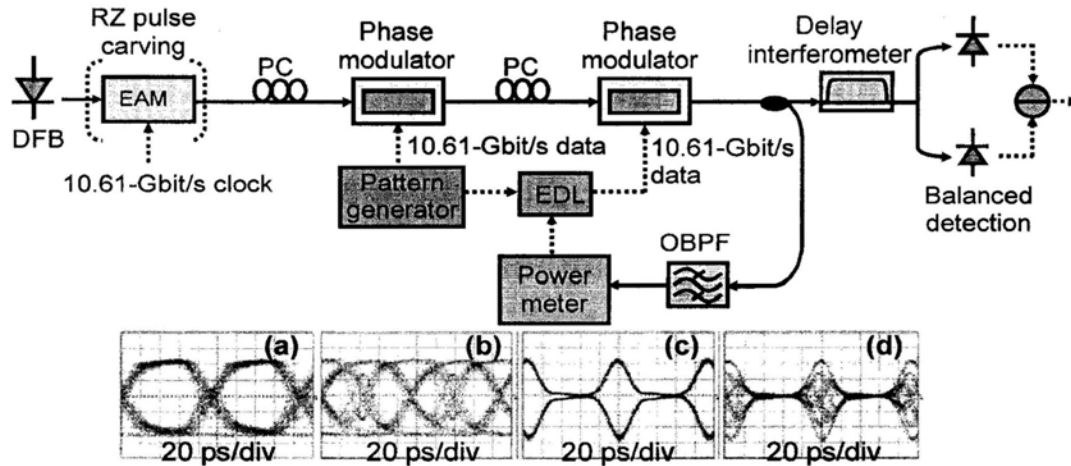


Fig. 5.17. Experimental setup. Insets: the eye diagrams of the new DPSK signal after balanced detection for (a) the best case of phase re-modulation in NRZ-DPSK format; (b) the worst case of phase re-modulation in NRZ-DPSK format; (c) the best case of phase re-modulation in RZ-DPSK format; and (d) the worst case of phase re-modulation in RZ-DPSK format.

Fig. 5.17 shows the experimental setup. The old DPSK signal was generated by modulating a continuous wave (CW) light or an optical pulse train by a 10.61-Gbit/s $2^{31}-1$ pseudorandom binary sequence (PRBS) in a phase modulator (PM). The optical pulse train was obtained by pulse carving a CW light using an electroabsorption modulator (EAM) driven by a 10.61-Gbit/s electrical clock. The wavelength of the CW light and the optical pulse train, λ_0 , were 1545.83 nm. The old DPSK signal was re-modulated with modulation depth of π by using another PM. An electrical delay line (EDL) was employed to adjust the time delay between the old DPSK signal and the delta DPSK data. The new DPSK signal was demodulated by a delay interferometer with the relative delay of 94.3 ps and detected by a balanced detector. The monitor consisted of a 0.2-nm

OBPF with tunable central wavelength, and a power meter. Insets of Fig. 5.17 show the eye diagrams of the new DPSK signal after balanced detection for (a) the best case of phase re-modulation in NRZ-DPSK format; (b) the worst case of phase re-modulation in NRZ-DPSK format; (c) the best case of phase re-modulation in RZ-DPSK format; and (d) the worst case of phase re-modulation in RZ-DPSK format. From the figure, it is shown that unsynchronized phase re-modulation causes severe eye closure, thus greatly degrades the performance. At the same time, it also causes power variation across the new DPSK signal's spectrum.

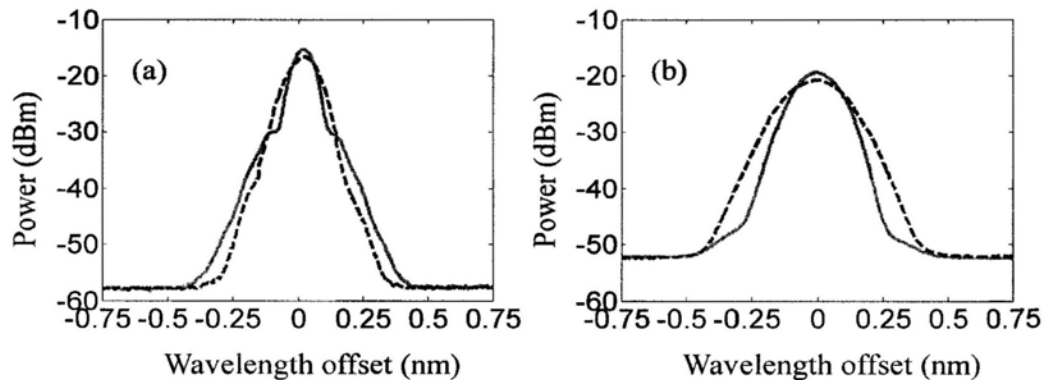


Fig. 5.18. The spectra of the new DPSK signal versus the wavelength offset with respect to the central wavelength of the DPSK signal under the best case (solid) and the worst case (dashed) of phase re-modulation for (a) NRZ-DPSK and (b) RZ-DPSK formats.

Fig. 5.18 depicts the spectra of the new DPSK signal versus the wavelength offset with respect to the central wavelength of the DPSK signal under the best case (solid) and the worst case (dashed) of phase re-modulation in (a) NRZ-DPSK and (b) RZ-DPSK formats. From the figure, it is shown that in NRZ-DPSK format, unsynchronized phase re-modulation causes spectral power decrease for the spectrum

$|\lambda - \lambda_0| < 0.05$ nm and $|\lambda - \lambda_0| > 0.15$ nm, and spectral power increase for the spectrum 0.05 nm $< |\lambda - \lambda_0| < 0.15$ nm. On the other hand, in RZ-DPSK format, unsynchronized phase re-modulation causes spectral power decrease for the spectrum $|\lambda - \lambda_0| < 0.08$ nm, and spectral power increase for the spectrum $|\lambda - \lambda_0| > 0.08$ nm. Such spectral power variation can be extracted by a narrowband OBPF and measured by a power meter.

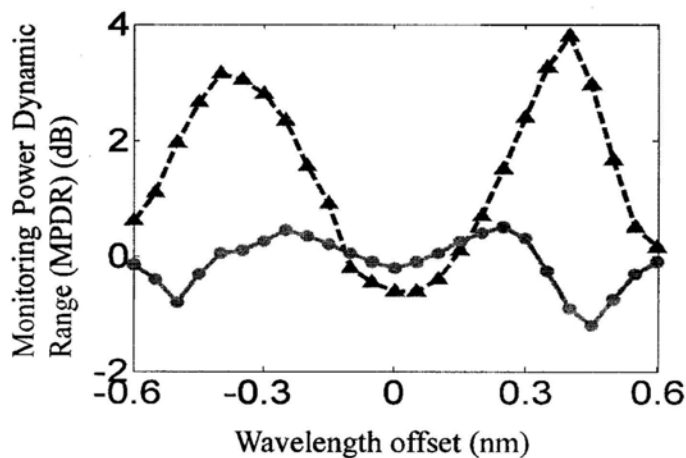


Fig. 5.19. The MPDR versus the wavelength offset of the OBPF with respect to the central wavelength of the DPSK signal for NRZ-DPSK (solid) and RZ-DPSK (dashed) formats.

Fig. 5.19 shows the MPDR versus the wavelength offset of the OBPF with respect to the central wavelength of the DPSK signal for NRZ-DPSK (solid) and RZ-DPSK (dashed) formats. Notice that the bandwidth of the OBPF is 0.2 nm and the monitoring power is averaged over the OBPF-filtered spectrum. At small wavelength offset, when the phase re-modulation is unsynchronized, there are both spectral power increase and spectral power decrease across the OBPF-filtered spectrum, resulting in small power difference between the worst case and the best case of phase re-modulation. In contrast, at the wavelength offset of 0.45 nm or 0.4 nm,

when the phase re-modulation is unsynchronized, only spectral power decrease or increase exhibits across the OBPF-filtered spectrum for NRZ-DPSK or RZ-DPSK format. As a result, optimal MPDR values of -1.2 dB at the wavelength offset of 0.45 nm and 3.8 dB at the wavelength offset of 0.4 nm are obtained for NRZ-DPSK and RZ-DPSK formats respectively, thus achieving high monitoring sensitivity. Meanwhile, the monitoring module is polarization independent.

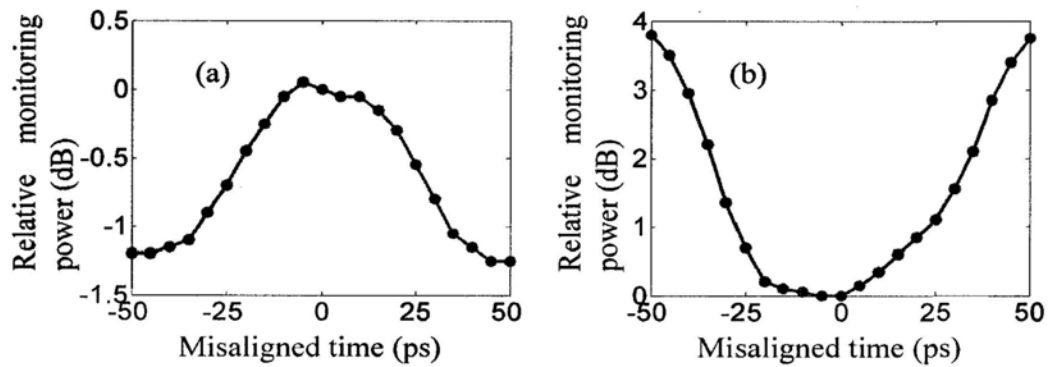


Fig. 5.20. The relative monitoring power versus re-modulation misaligned time for (a) NRZ-DPSK and (b) RZ-DPSK formats. The central wavelength of the OBPF is optimized and the relative monitoring power is with respect to the monitoring power for the best case of phase re-modulation.

Fig. 5.20 shows the relative monitoring power versus re-modulation misaligned time for (a) NRZ-DPSK and (b) RZ-DPSK formats. In the figure, the central wavelength of the OBPF is optimized and the relative monitoring power is with respect to the monitoring power for the best case of phase re-modulation. It is shown that when the misaligned time is larger than +10 ps or less than -10 ps, the relative monitoring power changes significantly. The monitoring signal is fed back to control the EDL for automatic SPRM. As a result, the potential penalty induced by unsynchronized phase re-modulation is avoided.

5.6 Summary

In this chapter, two alignment monitoring schemes have been proposed and experimentally demonstrated to monitor the alignment between the pulse carver and data modulator in RZ-OOK and RZ-DPSK systems, respectively. The first one is based on delay tap asynchronous waveform sampling technique. It is simple, applicable to any kind of optical intensity modulator, and is able to determine both the magnitude and the direction of modulation misalignment. The second scheme is based on off-center optical filtering technique. By measuring the power at the output of an off-center bandpass filter, the misalignment induced chirp can be captured and so the amount of modulation misalignment can be determined. The scheme is simple, polarization insensitive and has high monitoring dynamic range. The same technique was also applied to monitor the data synchronization in SPRM systems for both NRZ and RZ signals.

Chapter 6 Conclusions and Future Works

6.1 Summary of the Thesis

In this thesis, we have tackled four challenging issues in the field of optical performance monitoring: OSNR monitoring, CD monitoring, PMD monitoring, and alignment monitoring. The major contribution of this thesis can be summarized as follows:

1. We have proposed and investigated a novel, simple, and robust in-band optical signal to noise ratio (OSNR) monitoring technique using phase modulator embedded fiber loop mirror (PM-FLM). This technique measures the in-band OSNR accurately by observing the output power of a fiber loop mirror filter, where the transmittance is adjusted by an embedded phase modulator driven by low-frequency periodic signal. The robustness against polarization mode dispersion, chromatic dispersion, bit-rate, and partially polarized noise is experimentally demonstrated.
2. We have proposed and demonstrated the use of birefringent fiber loop (BFL) to facilitate chromatic dispersion monitoring based on RF spectrum analysis. By feeding a signal into a fiber loop which consists of a high-birefringence (Hi-Bi) fiber, we experimentally show that the amount of experienced dispersion can be deduced from the RF power at a specific selected frequency which is adjustable by the length of the Hi-Bi fiber. Experimental results show that this technique can provide high monitoring resolution and dynamic range as large as 1500 ps/nm.
3. We have demonstrated two different PMD monitoring schemes.

The first one is based on the analysis of frequency-resolved state-of-polarization (SOP) rotation, with signal spectrum broadened by self-phase modulation (SPM) effect. Experimental results show that the use of broadened signal spectrum induced by SPM not only relaxes the filter requirement and reduces the computational complexity, but also improves the estimation accuracy, and extends the monitoring range of the pulsewidth. The second one is based on the delay-tap asynchronous waveform sampling technique. By examining the statistical distribution of the measured scatter plot, unambiguous PMD measurement range up to 50% of signal bit-period is demonstrated.

4. We have employed the delay-tap asynchronous sampling technique to monitor the pulse carver and the data modulator misalignment in RZ-OOK transmission system. Experimental results show that both the misalignment direction and magnitude can be successfully determined. Besides, we have proposed and experimentally demonstrated the use of off-center optical filtering technique to capture the amount of spectrum broadening induced by the misalignment between the pulse-carver and the data modulator in RZ-DPSK transmission system. The scheme is polarization insensitive and has high monitoring power dynamic range. The same technique has been also applied to monitor the synchronization between old and new data in synchronized phase re-modulation (SPRM) system for both NRZ and RZ signals.

6.2 Future Works

There are several aspects in which the optical performance monitoring research can be continued. In our study on OSNR monitoring, CD

monitoring and PMD monitoring, only NRZ-OOK and RZ-OOK modulation formats are considered. More analyses on carrier suppressed RZ-OOK, alternate-chirped RZ-OOK, and all forms of DPSK/DQPSK formats which attract so much attention recently can be performed. Also, when we study the effects of PMD, only first-order PMD was emulated in our experiments. Studies concerning the effects of high-order PMD can be carried out.

For the monitoring schemes based on delay-tap asynchronous sampling techniques, currently only the signal waveform amplitude information can be obtained. It is interesting to explore the possibility to combine with interferometric techniques to acquire the signal phase information as well so that a more comprehensive picture of the signal can be derived.

The ultimate OPM envisions a simple device that can analyze an optical signal and characterize multiple parameters and a suite of impairments simultaneously. Some of the OSNR, CD and PMD monitoring techniques share similar working principles. Therefore the most probable but maybe also the most challenging next step is to decouple one type of these impairments in the presence of others. Additional research effort in the area of simultaneous OSNR, CD and PMD monitoring is surely worthwhile.

Finally, when deploying OPM in real network, network operator has to decide where the OPMs should be located and how frequent and what kind of the monitoring information should be collected. In order to make the best decision, higher layer research on mathematical optimization can be carried out. Further research endeavor in this direction will be vital to achieve the most effective deployment of physical layer OPM.

Bibliography

- [1] B. st. Arnaud, "Overview of the latest developments in optical Internets," *Optical Networks Magazine*, vol. 1, no. 3, pp. 51-54, 2000..
- [2] G. Rossi, T. E. Dimmick, and D. J. Blumenthal, "Optical performance monitoring in reconfigurable WDM optical networks using subcarrier multiplexing", *IEEE Journal of Lightwave Technology*, vol. 18, no. 12, pp. 1639-1648, December 2000.
- [3] Vinod Ramakrishnan, M. Govindarajan, and John Klonick, "Intelligent performance monitoring in optical networks", *Telecommunications Online*, January 2001.
- [4] Byrav Ramamurthy, Debasish Datta, Helena Feng, Jonathan P. Heritage, and Biswanath Mukherjee, "Impact of transmission impairments on the teletraffic performance of wavelength-routed optical networks", *IEEE Journal of Lightwave Technology*, vol. 17, no. 10, pp. 1713 – 1723, October 1999.
- [5] Robert Friskney, Kevin Warbrick, Simon Poliakoff, and Richard Heath, "Link-based photonic path performance prediction and control", in *Proc. ECOC 2002*, Copenhagen, Denmark, 2002, paper 7.4.3.
- [6] D. C. Kilper, R. Bach, D. J. Blumenthal, D. Einstein, T. Landolsi, L. Ostar, M. Preiss, and A. E. Willner, "Optical performance monitoring", *IEEE Journal of Lightwave Technology*, vol. 22, no. 1, pp. 294 – 304, January 2004.
- [7] Richard E. Neuhauser, "Optical performance monitoring (OPM) in next-generation optical networks", APOC 2002, (Invited paper), in *Proc. SPIE 2002*, Shanghai, China, 2002, paper 4909-47.

-
- [8] Keith Beckley, "Optical performance monitors continue to chase market", *Lightwave Magazine*, April 2004.
 - [9] Eugene Park, "Error Monitoring for Optical Metropolitan Network Services", *IEEE Communications Magazine*, vol. 40, no. 2, pp.104-109, Feb 2002.
 - [10] Bellcore Generic Requirements GR-253-CORE, Synchronous Optical Network (SONET) Transport Systems: Common Generic Criteria.
 - [11] ITU-T G.957 – Optical Interfaces for Equipments and Systems Relating to the Synchronous Digital Hierarchy, International Telecommunications Union.
 - [12] ITU-T G.958 – Digital Line Systems Based on the Synchronous Digital Hierarchy for use on Optical Fiber Cables, International Telecommunications Union.
 - [13] Hitoshi Takeshita and Naoya Henmi, "A novel data format free bit-by-bit quasi-error monitoring method for optical transport network" in *Proc. OFC 1999*, San Diego, USA, 1999, paper FJ2-1
 - [14] Lian Kuan Chen, Man Hong Cheung, Chun Kit Chan, Frank Tong, "Performance monitoring in transparent reconfigurable WDM networks", in *Proc. OECC 2003*, Shanghai, PRC, 2003, Paper 14D1.1.
 - [15] Giampaolo Bendelli, Carlo Cavazzoni, Raffaele Girardi, Roberto Lano, "Optical performance monitoring techniques", in *Proc. ECOC 2000*, Munich, Germany, 2000, vol. 4, pp. 113-116.
 - [16] Richard Habel, Kim Roberts, Alan Solheim, and James Harley, "Optical domain performance monitoring", in *Proc. OFC 2000*, Baltimore, Maryland, 2000, paper WK3-1.
 - [17] TIA/EIA-526-19 standard: OFSTP-19 Optical signal-to-noise ratio measurement procedures for dense wavelength-division systems.
 - [18] "Optical signal to noise ratio (OSNR)", white paper from Cicadiant Systems Inc., December 2002.

-
- [19] "BER vs. OSNR", white paper from Cicadant Systems Inc., February 2003.
- [20] Alex Vukovic, Michel Savoie, Heng Hua, "Performance monitoring challenges of next generation networks", *Communications Systems and Networks (CSN 2003), IASTED Conference*, Benalmadena, Spain, 2003.
- [21] D. C. Kilper and W. Weingartner, "Monitoring optical network performance degradation due to amplifier noise", *IEEE Journal of Lightwave Technology*, vol. 21, no. 5, pp. 1171-1178, May 2003.
- [22] D. C. Kilper, S. Chandrasekhar, L. Buhl, A. Agarwal, and D. Maywar, "Spectral monitoring of OSNR in high-speed networks", in *Proc. ECOC 2002*, Copenhagen, Denmark, 2002, paper p7.4.4.
- [23] H. Suzuki and N. Takachio, "Optical signal quality monitor built into WDM linear repeaters using semiconductor arrayed waveguide grating filter monolithically integrated with eight photodiodes", *IET Electronics Letters*, vol. 35, pp. 836-837, May 1999.
- [24] Wenlu Chen, Shan Zhong, Zhonghua Zhu, Wei Chen, and Yung-Jui (Ray) Chen, "Adding OSNR and wavelength monitoring functionalities on a double-resolution-AWG-based power monitoring circuit", *IEEE Photonics Technology Letter*, vol. 15, no. 6, June 2003.
- [25] K. Asahi, M. Yamashita, T. Hosoi, K. Nakaya, and C. Konoshi, "Optical performance monitor built into EDFA repeaters for WDM networks", in *Proc. OFC' 98*, San Jose, USA, 1998, paper ThO2.
- [26] J. Chappell and S. DeMange, "Optical signal-to-noise ratio characterization demands precision and flexibility", *WDM Solutions*, vol. 2, no. 6, pp. 55-60, Nov. 2000.
- [27] Chun-Liang Yang and San-Liang Lee, "OSNR monitoring using double-pass filtering and dithered tunable reflector", *IEEE Photonics Technology Letters*, vol. 16, no.6, pp.1570-1572, June 2004.

- [28] S. K. Shin, K. J. Park, and Y. C. Chung, "A novel optical signal-to-noise-ratio monitoring technique for WDM networks", in *Proc. OFC '2000*, Baltimore, Maryland, 2000, paper WK6.
- [29] C. J. Youn, S. K. Shin, K. J. Park, and Y. C. Chung, "OSNR monitoring technique based on high-frequency receiver noise", APOC 2001, in *Proc. SPIE 4584*, 2001.
- [30] C. Y. Joun, K. J. Park, J. H. Lee, and Y. C. Chung., "OSNR monitoring technique based on orthogonal delayed-homodyne method", *IEEE Photon. Technol. Lett.*, vol. 14, pp.1469-1471, Oct 2002.
- [31] Howard R. Stuart, "Optical performance monitoring using narrowband radio frequency analysis at the half-clock frequency", *OSA Journal of Optical Networking*, vol. 3, no. 6, pp. 396-409, June 2004.
- [32] M. Rasztovits-Wiech, M. Danner, and W. R. Leeb, "Optical signal-to-noise ratio measurement in WDM networks using polarization extinction", in *ECOC '98*, Madrid, Spain, 1998, pp. 549-550.
- [33] J. H. Lee, D. K. Jung, C. H. Kim, and Y. C. Chung, "OSNR monitoring technique using polarization-nulling method", *IEEE Photon. Technol. Lett.*, vol. 13, pp. 88-90, Jan 2001.
- [34] Mats Petersson, Henrik Sunnerud, Magnus Karlsson, and Bengt-Erik Olsson, "Performance monitoring in optical networks using stokes parameters", *IEEE Photonics Technology Letters*, vol. 16, no. 2, February 2004.
- [35] S. M. R. Motaghian Nezam, A. Sahin, J. McGeehan, Z. Pan, T. Luo, Y. Song, "Polarization state rotation filtering for single sideband generation and carrier suppression using a variable dgd element", in *Proc. OFC 2003*, Atlanta, USA, 2003, paper FM7.

- [36] Man-Hong Cheung, Lian-Kuan Chen, Chun-Kit Chan, "On robustness of in-band polarization-assisted OSNR monitoring schemes against PMD", in *Proc. CLEO/PR 2003*, Taipei, Taiwan, 2003, Paper W1J.
- [37] Man-Hong Cheung, Lian-Kuan Chen, Chun-Kit Chan, "PMD-insensitive OSNR monitoring based on polarization-nulling with off-center narrowband filtering", *IEEE Photonics Technology Letter*, vol. 16, no. 11, Nov 2004.
- [38] J. H. Lee and Y. C. Chung, "Improved OSNR monitoring technique based on polarization-nulling method", *IET Electronics Letter*, vol. 37, no.15, pp. 972 – 973, July 2001.
- [39] Z. Zalevsky, D. Abraham, V. Eckhouse, and Y. Beiderman, "In-band optical signal-to-noise ratio network monitoring using periodic polarization modulation", *OSA Journal of Optical Networking*, vol. 2, pp. 303-314, Sept 2003.
- [40] M. H. Cheung, L. K. Chen, and C. K. Chan, "A PMD-insensitive OSNR monitoring scheme based on polarization-nulling with off-center narrowband filtering", in *Proc. OFC 2004*, Los Angeles, CA, 2004, paper FF2.
- [41] E. Lichtman, "Limitations imposed by polarization-dependent gain and loss on all-optical ultralong communication systems," *IEEE Journal of Lightwave Technology*, vol. 13, no. 5, pp. 906-912, May 1995.
- [42] F. Bruyere and O. Andouin, "Penalties in long-haul optical amplifier systems due to polarization dependent loss and gain," *IEEE Photonics Technology Letters*, vol. 6, no. 5, pp. 654-656, May 1994.
- [43] Mark D. Feuer, "Measurement of OSNR in the Presence of Partially Polarized ASE," *IEEE Photonics Technology Letters*, vol. 17, no. 2, pp. 435-437, Feb. 2005.

- [44] X. Liu and Y. H. Kao, "A Simple OSNR Monitoring Technique Independent of PMD and Chromatic Dispersion Based on A 1-bit Delay Interferometer," in *Proc. ECOC 2006*, Cannes, France, 2006, paper Mo4.4.5.
- [45] Yannick Keith Lizé, Jeng-Yuan Yang, Louis Christen, Xiaoxia Wu, Scott Nuccio, Teng Wu, Alan E. Willner, Raman Kashyap and François Séguin, "Simultaneous and Independent Monitoring of OSNR, Chromatic and Polarization Mode Dispersion for NRZ-OOK, DPSK and Duobinary," in *Proc. OFC/NFOEC 2007*, Anaheim, USA, 2007, paper OThN2.
- [46] Elaine Wong, Ka Lun Lee, and Ampalavanapillai Nirmalathas, "Novel In-Band Optical Signal-to-Noise Ratio Monitor for WDM Networks," in *Proc. OECC 2005*, Seoul, Korea, 2005, paper 6B3-5
- [47] Zhenning Tao, Zhangyuan Chen, Libin Fu, Deming Wu, and Anshi Xu, "Monitoring of OSNR by using a Mach-Zehnder interferometer", *Microwave and Optical Technology Letters*, vol. 30, no.1, pp. 63-65, May 2001.
- [48] N. Onodera, K. Tsuji, T. Wantanabe, and M. Saruwatari, "Polarization-Independent, Active Birefringent Optical Fiber loop Filters for WDM Systems," in *Proc. OECC 2005*, Seoul, Korea, 2005, Paper 6E4-4
- [49] M.P. Fok, K.L. Lee, C. Shu, "Waveband-Switchable SOA Ring Laser Constructed With a Phase Modulator Loop Mirror Filter," *IEEE Photon. Technol. Lett.*, vol. 17, pp. 1393-1396 (2005).
- [50] G. P. Agrawal, *Fiber Optic Communications Systems*, John Wiley & Sons, New York, 2002.
- [51] A.E. Willner and B. Hoanca "Fixed and Tunable Management of Fiber Chromatic Dispersion," in *Optical Fiber Telecommunications IV-B*, Academic Press, 2002.

- [52] Z. Pan, Q. Yu, Y. Xie, S. A. Havstad, A. E. Willner, D. S. Starodubov, and J. Feinberg, "Chromatic dispersion monitoring and automated compensation for NRZ and RZ data using clock regeneration and fading without adding signaling," in *Proc. OFC 2003*, Atlanta, USA, 2003, paper WH5
- [53] Q. Yu, Z. Pan, L.S. Yan, and A.E. Willner, "Chromatic dispersion monitoring technique using sideband optical filtering and clock phase-shift detection," *IEEE Journal of Lightwave Technology*, vol. 20, pp. 2267-2271, 2002.
- [54] H. Schmuck, "Comparison of optical millimetre-wave system concepts with regard to chromatic dispersion," *IET Electronics Letters*, vol. 31, no. 21, pp. 1848-1849, 1995.
- [55] C.W. Chow and H.K. Tsang, "Polarization-Independent DPSK Demodulation Using a Birefringent Fiber Loop," *IEEE Photonics Technology Letters*, vol. 17, no. 6, pp. 1313-1315, 2005
- [56] K.T. Tsai, and W.I. Way, "Chromatic-Dispersion Monitoring Using an Optical Delay-and-Add Filter," *IEEE Journal of Lightwave Technology*, vol. 23, no. 11, Nov. 2005.
- [57] S. Wielandy, M. Fishteyn, T. Her, D. Kudelko, C. Zhang, "Real time measurement of accumulated chromatic dispersion for automatic dispersion compensation," *IET Electronics Letters*, vol. 38, no. 20, pp. 1198-1199, 2002.
- [58] A. E. Willner, S. M. R. Motaghian Nezam, L. S. Yan, Z. Pan, and M. C. Hauer, "Monitoring and control of polarization-related impairments in optical fiber systems", *IEEE Journal of Lightwave Technology*, vol. 22, no. 1, pp. 106-125, January 2004.
- [59] H. Sunnerud, M. Karlsson, and P. A. Andrekson, "A comparison between NRZ and RZ data formats with respect to PMD-induced system outage probability", *IEEE Photonics Technology Letter*, vol. 13, no. 5, pp. 448-450, May 2001.

- [60] H. Bulow, "System outage probability due to first- and second- order PMD", *IEEE Photonics Technology Letter*, vol. 10, no. 5, pp. 696-698, May 1998.
- [61] D. Penninckx, F. Roy, S. Lanne, and J. P. Thiery, "Statistical study of dynamic polarization-mode-dispersion compensation based on degree of polarization monitoring", *Microw. Optic. Technol. Lett.*, vol. 25, no. 1, pp. 41-43, May 2000.
- [62] C. Francia, F. Bruyere, J. -P. Thiery, and D. Penninckx, "Simple dynamic polarization mode dispersion compensator", *IEE Electronics Letter*, vol. 35, no. 5, pp. 414-415, March 1999.
- [63] Herwig Kogelnik and Robert M. Jopson, "Polarization-Mode Dispersion," in *Optical Fiber Telecommunications IV-B*, Academic Press, 2002.
- [64] Nobuhiko Kikuchi, "Analysis of signal degree of polarization degradation used as control signal for optical polarization mode dispersion compensation", *IEEE Journal of Lightwave Technology*, vol. 19, no. 4, April 2001.
- [65] S. Bahsoun, J. Negel, and C. Poole, "Measurement of temporal variations in fiber transfer characteristics to 20 GHz due to polarization-mode-dispersion", in *Proc. ECOC'90*, pp. 1003, postdeadline paper.
- [66] F. Heismann, D. A. Fishman, and D. L. Wilson, "Automatic compensation of first order polarization mode dispersion in a 10 Gb/s transmission system", in *Proc. ECOC'98*, vol. 1, pp. 529-530.
- [67] H. Y. Pua, K. Peddanarappagari, B. Zhu, C. Allen, K. Demarest, and R. Hui, "An adaptive first-order polarization-mode-dispersion compensation system aided by polarization scrambling: Theory and demonstration", *IEEE Journal of Lightwave Technology*, vol. 18, no. 6, pp. 832-841, June 2000.

- [68] T. Takahashi, T. Imai, and M. Aiki, "Automatic compensation technique for timewise fluctuating polarization mode dispersion in in-line amplifier systems", *IET Electronics Letter*, vol. 30, no. 4, pp.348-349, February 1994.
- [69] G. Ishikawa and H. Ooi, "Polarization-mode-dispersion sensitivity and monitoring in 40-Gb/s OTDM and 10-Gbit/s NRZ transmission experiments" in *Proc. OFC'98*, Washington, USA, 1998, paper WC5.
- [70] S. M. R. Motagian Nezam, Y. W. Song, A. B. Sahin, Z. Pan, and A. E. Willner, "PMD monitoring in WDM systems for NRZ data using a chromatic-dispersion regenerated clock" in *Proc. OFC 2002*, Anaheim, USA, 2002, pp. 200-202, paper WE5.
- [71] M. Hayashi, H. Tanaka, and M. Suzuki, "Low frequency band monitoring method for PMD compensation", *IET Electronics Letter*, vol. 38, no. 24, pp.1564-1565, November 2002.
- [72] S. M. R. Motaghian Nezam, Y. Wang, M. Hauer, S. Lee, and A. E. Willner, "Simultaneous PMD monitoring of several WDM channels using subcarrier tones", in *Proc. CLEO 2001*, Baltimore, Maryland, 2001, pp. 561-563, paper CFE1.
- [73] F. Buchali, S. Lanne, J. -P. Thiery, W. Baumert, and H. Bulow, "Fast eye monitor for 10 Gbit/s and its application for optical PMD compensation", in *Proc. OFC 2001*, Anaheim, USA, 2001, TuP5-1/TuP5-3.
- [74] F. Buchali, W. Baumert, H. Bulow, and J. Poirrier, "A 40 Gb/s eye monitor and its application to adaptive PMD compensation", in *Proc. OFC 2002*, Anaheim, USA, 2001, pp. 202-203, paper WE6.
- [75] B. W. Hakki, "Polarization mode dispersion compensation by phase diversity detection", *IEEE Photonics Technology Letters*, vol. 9, no. 1, January 1997.
- [76] R. Noe, D. Sandel, V. Mirvoda, F. Wust, and S. Hinz, "Polarization mode dispersion detected by arrival measurement of

- polarization-scrambled light”, *IEEE Journal of Lightwave Technology*, vol. 20, no. 2, February 2002.
- [77] M. Boroditsky, N. Frigo, P. Magill, L. Raddtz, “Technique for in-situ measurement of polarization mode dispersion,” in *Proc. OFC 2003*, Atlanta, USA, 2003, paper TuK1
- [78] Lothar Moller, Larry Buhl, “Method for PMD vector monitoring in picosecond pulse transmission systems,” *IEEE Journal of Lightwave Technology*, vol. 19, no. 8, pp. 1125-1129, 2001.
- [79] G. Bosco, B.E. Olsson, and D.J. Blumenthal, “Pulsewidth distortion monitoring in a 40-Gb/s optical system affected by PMD,” *IEEE Photonics Technology Letters*, vol. 14, no. 3, pp. 307-309, 2002.
- [80] G.P. Agrawal, *Nonlinear Fiber Optics*, San Diego, CA: Academic Press, 2001.
- [81] S.M.R. Motaghian Nezam, L.S. Yan, J.E. McGeehan, Y.Q. Shi, A.E. Willner, and Steve Yao, “Wide-Dynamic-Range DGD Monitoring by Partial Optical Signal Spectrum DOP Measurement,” in *Proc. OFC 2002*, pp. 924-926, 2002.
- [82] F. Buchali, S. Lanne, J.P. Thiery, W. Baumert, and H. Bulow, “Fast eye monitoring for 10 Gbit/s and its application for optical PMD compensation,” in *Proc. OFC 2001*, Anaheim, USA, 2001, paper TuP5.
- [83] P.S. Westbrook, L.E. Nelson, S. Wielandy, J. Fini, “Enhancement of spectral polarimetry for PMD measurement using transmitted signal spectra,” in *Proc. OFC 2004*, Los Angeles, CA, 2004, Paper FI5
- [84] S. D. Dods and T. B. Anderson, “Optical performance monitoring technique using delay tap asynchronous waveform sampling,” in *Proc. OFC 2006*, Anaheim, USA, 2006, paper OThP5
- [85] TIA/EIA-526-4, *Optical Eye Pattern measurement Procedure*, 1995.

-
- [86] S.W. Hinch and C.M. Miller, "Analysis of digital modulation on optical carriers," in D. Derickson, ed., *Fiber Optic Test and Measurement*, Prentice Hall, Upper Saddle River, NJ, 1998.
- [87] N Hanik, A Gladisch, C Caspar, and B Strebel, "Application of amplitude histograms to monitor performance of optical channels," *IET Electronics Letters*, vol. 35, pp. 403-404, 1999.
- [88] I Shake, H Takara, and S Kawanishi, "Simple measurement of eye diagram and BER using high-speed asynchronous sampling," *IEEE Journal of Lightwave Technology*, vol. 22, pp. 1296-1302, 2004.
- [89] J. Zyskind, R. Barry, G. Pendock, M. Cahill, and J. Ranka, "High-Capacity, Ultra-Long-Haul Networks," in *Optical Fiber Telecommunications IVB*, Academic Press, 2002.
- [90] J.H. Sinsky, "High-Speed Data and Pulse-Carver Alignment in Dual Mach-Zehnder Modulator Optical Transmitters Using Microwave Signal Processing," in *IEEE Journal of Lightwave Technology*, vol. 21, no. 2, pp. 412-423, 2003.
- [91] I. Kang, L. Mollenauer, B. Greene, and A. Grant, "A Novel Method for Synchronizing the Pulse Carver and Electroabsorption Data Modulator for Ultralong-Haul DWDM Transmission," in *IEEE Photonics Technology Letters*, vol. 14, no. 9, pp. 1357-1360, 2002.
- [92] H. Kim, C.R. Doerr, R. Pafchek, L.W. Stulz, and P. Bernasconi, "Alignment Monitoring of the Pulse Carver and Data Modulator for RZ-DPSK Systems," in *IEEE Photonics Technology Letters*, vol. 15, no. 11, pp. 1594-1596, 2003.
- [93] William Shieh, Xingwen Yi, and An V. Tran, "Label swapping for DPSK encoded Labels without wavelength conversion", in Proc. OFC 2005, Anaheim, CA, 2005, paper OTuC1.
- [94] Xingwen Yi and William Shieh, "On polarization sensitivity of all-optical label swapping using synchronous phase modulation" in

- IEEE Photonics Technology Letters*, vol. 18, no. 11, pp 1210-1211, Jun. 2006.
- [95] Yue Tian, Yikai Su, Lilin Yi, Lufeng Leng, Xiangqing Tian, Hao He, and Xinyu Xu, "Optical VPN in PON based on DPSK erasing/rewriting and DPSK/IM formatting using a single Mach-Zehnder modulator", in *Proc. ECOC 2006*, Cannes, France, 2006, paper Tu4.5.6.
- [96] Siu-Sun Pun, Chun-Kit Chan, and Lian-Kuan Chen, "Demonstration of a novel optical transmitter for high-speed differential phase shift keying / inverse return-to-zero orthogonally modulated signals", *IEEE Photonics Technology Letters*, vol. 17, no. 12, pp 2763-2765, Dec. 2005.

Appendix – List of Publications

1. Yuen-Ching Ku, Chun-Kit Chan, and Lian-Kuan Chen, “A Robust Optical Signal to Noise Ratio Monitoring Scheme Using Phase Modulator Embedded Fiber Loop Mirror”, to appear in *OSA Optics Letters*, vol. 32, no. 7, pp. 1752-1754, Jul. 2007.
2. Jian, Zhao, Yuen-Ching Ku, and Lian-Kuan Chen, “A Simple Monitoring Technique for Synchronized Phase Re-modulation Using Narrowband Optical Filtering,” in *IET Electronics Letters*, vol. 43, no. 6, pp. 363-364, Mar 2007.
3. Chun-Kit Chan, Yuen-Ching Ku, and Lian-Kuan Chen, “Novel Techniques for Optical Performance Monitoring in Optical Systems,” in *Proc. Asia Pacific Optical Communications Conference (APOC) 2006*, paper 6354-45, Korea, Gwangju, Sep. 2006.
4. Yuen-Ching Ku and Chun-Kit Chan, “High-Speed Data and Pulse-Carver Alignment in RZ-OOK Systems Using Delay Tap Asynchronous Waveform Sampling,” in *Proc. European Conference on Optical Communications (ECOC)*, Paper Tu4.2.2, Cannes, France, Sep. 2006.
5. Yuen-Ching Ku, Kit, Chan, Chun-Kit Chan, and Lian-Kuan Chen, “Patterning Effect Avoidance of SOA-based Demultiplexer in 80-Gb/s OTDM System Using RZ-DPSK Modulation Format,” in *Proc. Opto-Electronics and Communications Conference (OECC)*, Paper 7C1-4, Kaohsiung, Taiwan, Jul. 2006.
6. Qiguang Zhao, Xiaofeng Sun, Yuen-Ching Ku, Chun-Kit Chan, and Lian-Kuan Chen, “A Novel Internetworking Scheme for WDM Passive Optical Network Based on Remodulation Technique,” in *Proc. IEEE/OSA Optical Fiber Communication Conference / National Fiber*

- Optic Engineers Conference (OFC/NFOEC)*, Paper JThB67, Anaheim, California, United States, Mar. 2006.
7. Yuen-Ching Ku, Chun-Kit Chan, and Lian-Kuan Chen, “Chromatic Dispersion Monitoring Technique Using Birefringent Fiber Loop,” in *Proc. IEEE/OSA Optical Fiber Communication Conference / National Fiber Optic Engineers Conference (OFC/NFOEC)*, Paper OFN2, Anaheim, California, United States, Mar. 2006.
 8. Yuen-Ching Ku, Chun-Kit Chan, and Lian-Kuan Chen, “A Novel Robust OSNR Monitoring Technique with 40-dB Dynamic Range Using Phase Modulator Embedded Fiber Loop Mirror,” in *Proc. IEEE/OSA Optical Fiber Communication Conference / National Fiber Optic Engineers Conference (OFC/NFOEC)*, Paper OWN6, Anaheim, California, United States, Mar. 2006.
 9. Yuen-Ching Ku, Chun-Kit Chan, and Lian-Kuan Chen, “A PMD-Insensitive OSNR Monitoring Technique with 40-dB Dynamic Range Using Phase Modulator Embedded Fiber Loop Mirror,” in *Workshop on Optical Transmission and Equalization (WOTE)*, Paper B5, Shanghai, China, Nov. 2005
 10. Zhaoxin Wang, Chinlon Lin, Kin-Kee Chow, Yuen-Ching Ku, and Anders Bjarklev, “Wavelength-Tunable Dispersion-Imbalanced Loop Mirror based on Dispersion-Flattened High-Nonlinearity Photonic Crystal Fiber and Its Application in Suppression of the Incoherent Interferometric Crosstalk,” in *IEEE Photonics Technology Letters*, vol. 17, no. 9, pp.1911-1913, Sep. 2005.
 11. Zhaoxin Wang, Chinlon Lin, Kin-Kee Chow, Yuen-Ching Ku, and Anders Bjarklev, “Nonlinear Suppression of Incoherent Interferometric Crosstalk with Dispersion Imbalanced Loop Mirror Using Dispersion-Flattened High-Nonlinearity Photonic Crystal Fiber,” in *Proc. IEEE Conference on Lasers and Electro-Optics (CLEO)*, Paper JThE43, Baltimore, Maryland, United States, May

- 2005.
12. Guowei Lu, Yuen-Ching Ku, Lian-Kuan Chen, and Chun-Kit Chan, “A Novel Technique for Pulse-Carver and Data Alignment Monitoring in RZ-DPSK Systems Using Off-Center Optical Filtering,” in *IEEE Photonics Technology Letters*, vol. 17, no. 3, pp. 711-713, Mar. 2005
 13. Yuen-Ching Ku, Guowei Lu, Chun-Kit Chan, and Lian-Kuan Chen, “Novel Technique for Modulation Alignment Monitoring in RZ-DPSK Systems Using Off-Center Optical Filtering,” in *IEEE/OSA Optical Fiber Communication Conference / National Fiber Optic Engineers Conference (OFC/NFOEC)*, Paper OWJ4, Anaheim, California, United States, Mar. 2005.
 14. Yuen-Ching Ku, Chun-Kit Chan, Lian-Kuan Chen, and Frank Tong, “Homodyne Crosstalk Tolerance Enhancement by Self-Phase Modulation Based All-Optical Regeneration,” in *Proc. International Conference on Optical Communications and Networks (ICOON)*, Hong Kong, Nov. 2004
 15. Guowei Lu, Chungjin Xie, Yuen-Ching Ku, Lian-Kuan Chen, and Chun-Kit Chan, “Enhanced PMD Monitoring with Frequency-Resolved SOP Rotation by Self-phase Modulation,” in *IEEE Photonics Technology Letters*, vol. 16, no. 9, pp.2180-2182, Sep. 2004.